Titre: Title:	Décomposition de la traînée d'installation motrice par la méthode de champ lointain
Auteur: Author:	Benoit Malouin
Date:	2015
Type:	Mémoire ou thèse / Dissertation or Thesis
Référence: Citation:	Malouin, B. (2015). Décomposition de la traînée d'installation motrice par la méthode de champ lointain [Ph.D. thesis, École Polytechnique de Montréal]. PolyPublie. https://publications.polymtl.ca/1822/

UNIVERSITÉ DE MONTRÉAL

DÉCOMPOSITION DE LA TRAÎNÉE D'INSTALLATION MOTRICE PAR LA MÉTHODE DE CHAMP LOINTAIN

BENOIT MALOUIN
DÉPARTEMENT DE GÉNIE MÉCANIQUE
ÉCOLE POLYTECHNIQUE DE MONTRÉAL

THÈSE PRÉSENTÉE EN VUE DE L'OBTENTION
DU DIPLÔME DE PHILOSOPHIÆ DOCTOR
(GÉNIE MÉCANIQUE)
AOÛT 2015

UNIVERSITÉ DE MONTRÉAL

ÉCOLE POLYTECHNIQUE DE MONTRÉAL

Cette thèse intitulée :

DÉCOMPOSITION DE LA TRAÎNÉE D'INSTALLATION MOTRICE PAR LA MÉTHODE DE CHAMP LOINTAIN

présentée par : MALOUIN Benoit
en vue de l'obtention du diplôme de : Philosophiæ Doctor
a été dûment acceptée par le jury d'examen constitué de :

M. ROBERT Étienne, Doctorat Sc., président
M. TRÉPANIER Jean-Yves, Ph. D., membre et directeur de recherche
M. LAURENDEAU Éric, Ph. D., membre et codirecteur de recherche
M. DESTARAC Daniel, Ing., membre
M. SADRI Reza, Ph. D., membre externe

DÉDICACE

À ma femme, Hala et à ma famille...

REMERCIEMENTS

Je voudrais tout d'abord et principalement remercier mes parents, Ann et Alain, qui m'ont toujours fortement encouragé à poursuivre mes études. Nul doute que si ce n'était de leur dévouement, de leur patience et de leurs inconditionnels confiance et amour, je ne serais pas rendu là aujourd'hui. De tout coeur, merci ! Je remercie également mon frère, François, que j'adore.

Un merci très spécial à ma femme, Hala, qui a été à mes côtés chaque jour pendant ce doctorat. Son amour, son écoute et son soutien dans les moments les plus difficiles m'ont été indispensables.

Je remercie mon directeur de recherche, le Professeur Jean-Yves Trépanier, pour m'avoir confié ce projet et, par le fait même, d'avoir eu confiance en moi. Je le remercie également pour l'aide qu'il m'a apportée ainsi que les idées de recherche qu'il a partagées avec moi. Je remercie aussi mon codirecteur, le Professeur Éric Laurendeau, pour son aide et pour ses judicieux conseils qu'il a su me prodiguer lors de la rédaction de mes articles.

Je tiens à remercier mon ami, Martin Gariépy, qui a travaillé sur la méthode de champ lointain lors de son doctorat. L'aide qu'il m'a apportée au début de mon doctorat m'a été très utile. Merci également pour nos nombreuses conversations et pour ton amitié. Je crois n'avoir jamais autant rigolé qu'avec toi. À ce sujet, je tiens à m'excuser auprès des professeurs de génie physique qui, j'en suis sur, ont été dérangés par moi et Martin. Je remercie également tous mes collègues et principalement Foad Mehdizadeh, Christophe Tribes, Alexandre Lupien, Eddy Petro, Sami Ammar ainsi que Philippe Couturier pour leur amitié et discussions des plus agréables. Par le fait même, je tiens à remercier Sébastien Leclaire avec qui j'ai partagé un bureau pendant cinq ans. Malgré qu'il était toujours très concentré sur sa recherche ;), Sébastien m'a souvent donné de très bons conseils. Merci pour ton aide, ton amitié, nos hilarantes conversations sur maints sujets et ta complicité.

RÉSUMÉ

L'objectif principal de cette thèse est de proposer une méthode permettant d'évaluer la traînée d'installation motrice d'un avion. Pour ce faire, la méthode de champ lointain est tout à fait indiquée puisqu'elle permet de diviser la traînée en traînées visqueuse, d'onde, induite et numérique associées respectivement aux phénomènes de couche limite, d'onde de choc, de création de portance, et d'ajout de dissipation artificielle, ou erreur numérique, par le résoluteur et des erreurs de discrétisation. La méthode de champ lointain a été souvent utilisée pour des configurations non-motorisées, mais son usage en conditions de poussée demeure plutôt récent. Trois sections associées à trois objectifs constituent cette thèse. Tous les objectifs ont fait l'object d'un article scientifique.

Selon la pratique en comptabilité traînée-poussée des avionneurs, la traînée interne de la nacelle ne doit pas être incluse dans la traînée d'installation car elle est de la responsabilité du motoriste. Par conséquent, il est primordial d'évaluer cette composante. Le premier objectif est donc de proposer une méthode permettant l'évaluation et la décomposition de la traînée d'une nacelle en composantes interne, externe et de sillage. Les méthodes actuellement disponibles sont les essais expérimentaux et les analyses numériques. Les ingénieurs utilisant la seconde approche emploient la méthode de champ proche qui consiste à intégrer les forces de pression et de frottement sur la surface interne de la nacelle. Un inconvénient majeur de cette méthode est que sa précision dépend fortement de la position de la ligne de stagnation qui sépare les écoulements interne et externe. La méthode proposée n'a pas cette limitation et donne des résultats qui sont en accord avec les valeurs expérimentales et empiriques.

La force de captation est aussi requise pour le calcul de la traînée de configuration. Dans ce deuxième axe, une méthode permettant l'évaluation de cette poussée est présentée. La méthode traditionnelle requiert la connaissance du tube de courant capturé par le moteur et nécessite donc la location précise de la ligne de stagnation. La méthode de champ lointain permet de contourner cette difficulté. Suivant la même logique, une méthode alternative de calcul pour la poussée standard nette est présentée. La procédure classique interpole les propriétés de l'écoulement dans le plan de sortie du moteur ce qui induit des erreurs. Dans les deux cas, les résultats des méthodes proposées sont en accord avec les données empiriques et les formulations classiques.

Finalement, la connaissance des traînées d'interférence et d'installation est importante autant pour les avionneurs que pour les motoristes qui souhaient établir les performances de leurs systèmes respectifs. L'évaluation de ces deux forces est maintenant possible suite aux

développements des deux méthodes présentées ci-dessus. Notons que la traînée d'interférence résulte de l'interaction entre la nacelle et l'aile. Il s'agit d'un phénomène couplé complexe à évaluer. Il est donc proposé de séparer la traînée d'installation en traînées de nacelle et d'interférence. La méthode de champ lointain permet également de séparer ces deux forces en composantes visqueuse, d'onde, induite, numérique et de captation. Pour ce faire, des simulations sur la nacelle isolée et sur les configurations aile-moteur et aile-moteur-pylon-nacelle sont requises. Toutes les simulations de cette thèse sont effectuées à l'aide du logiciel ANSYS Fluent 14.5 sur la configuration aile-fuselage DLR-F6 équipé de nacelles de type CFM56.

ABSTRACT

The main objective of this research is to propose a method to study the engine installation drag of an aircraft. To do so, the far-field method comes in handy because of its ability to decompose the drag of a given configuration with respect to the physical phenomena involved. For an aircraft flying at transonic speed, they consist of the boundary layer, the shock wave and the lift that are responsible for the viscous, wave and induced drags, respectively. Since computational fluid dynamic softwares are used to simulate the flow around the aircraft, another type of drag, the spurious drag, appears. It is the consequence of artificial dissipation added by the solver to enhance convergence and discretization errors. The spurious drag is usually present at areas where strong gradients are expected such as leading edges. This method was used for wing-body configurations but its use in motorized configurations remains quite modern. This thesis is divided into three main parts, each addressing an objective. These objectives have each been the subject of a scientific article.

The first one is to propose a method for decomposing the total drag of a nacelle into external, internal, and wake drag. From the airframer's bookkeeping agreement, the internal drag is the engine manufacturer's responsibility and is not to be included in the aircraft's total drag. Consequently, computing the internal drag is mandatory for the airframe and engine constructors of interest and can be achieved either experimentally or by computational-fluid-dynamics analysis. Up to now, aerodynamic engineers have used a near-field approach to compute the internal drag using computational-fluid-dynamics analysis, but this method has serious drawbacks, including its dependency on the accurate location of the stagnation line that divides the internal flow from the external flow. Results of the proposed method show that it is independent of the location of the stagnation line and yields accurate results that agree well with experimental and empirical data. Results also show that the wake drag of a through-flow nacelle is caused by the flow passing through the nacelle and so needs to be added to the internal drag.

The second objective concerns the computation of the engine pre-entry thrust. This quantity is required to evaluate the aircraft configuration drag. Numerical computation of this quantity requires knowledge of the captured streamtube, which, once again, depends on the stagnation line location. A new method that uses the far-field formulation is developed so that knowledge of the streamtube properties is no longer required. Using similar techniques, an alternative method to compute the standard net thrust, the basis of most thrust/drag bookkeeping systems, is introduced. The classical formulation to compute the standard net thrust needs

interpolation of flow quantities in the nacelle's exit plane which leads to loss of accuracy. Results of the proposed approaches are in agreement with ESDU and classical formulations.

Finally, both methods presented hereinabove are applied to compute the engine installation and interference drags. Computation of the engine installation drag is important to both airframers and engine manufacturers who wish to assess performance of their respective system. This force comprises the interference drag that results from the interaction between the wing and the engine's nacelle. Its evaluation is cumbersome because of the coupled nature of this phenomenon. It is thus proposed to decompose the installation drag in terms of interference and nacelle drags that, using the far-field method, can be further discretized in terms of viscous, wave, induced, spurious and pre-entry forces. By using simulations on the isolated nacelle, the wing-body and the wing-body-pylon-nacelle configurations, it is thus possible to compute and decompose both the interference and installation drags. All simulations in this thesis are performed with ANSYS Fluent 14.5 on the DLR-F6 wing-fuselage configuration equipped with CFM56 nacelles.

TABLE DES MATIÈRES

LISTE DES TABLEAUX

LISTE DES FIGURES

LISTE DES SIGLES ET ABRÉVIATIONS

TFN	Through Flow Nacelle
TPS	Turbine Powered Simulator
MFR	Mass Flow Ratio
BTN	Blow Through Nacelle
RANS	Reynolds-Averaged Navier-Stokes

CHAPITRE 1 INTRODUCTION

La minimisation des coûts de développement d'un avion ainsi que l'augmentation de son efficacité sont primordiales dans le contexte industriel hautement compétitif d'aujourd'hui et de demain. Dans cette optique, la mécanique des fluides numérique, communément nommée CFD pour Computational Fluid Dynamics, a permis aux ingénieurs-aérodynamiciens de faire d'immenses progrès en diminuant la dépendance aux onéreux essais en souffleries et en vol lors du développement d'avions. Depuis les années 70, la précision des simulations CFD n'a cessé de croître au même titre que leur usage au cœur du processus de conception. L'optimisation d'une aile, par exemple, se fait dorénavant sur ordinateur. Cependant, il y a encore du progrès à faire. En effet, la précision requise par les industriels est de prédire le coefficient de traînée au dix millième de décimale, soit de l'ordre de moins de 0.3% de la traînée totale de l'avion, ce qui demeure un défi pour l'étude de certaines configurations plus complexes.

Afin d'analyser la traînée, la méthode de champ lointain, communément appelée *far-field*, est utilisée dans cette thèse. Le premier avantage de la méthode de champ lointain est qu'elle permet la décomposition de la traînée en ses diverses composantes, soient la traînée d'onde, de viscosité, induite et finalement, la traînée numérique. La possibilité de quantifier et d'extraire la traînée numérique constitue le deuxième avantage de la méthode. Cette traînée numérique est causée par la dissipation artificielle implémentée dans tous les solveurs ainsi que par les erreurs de discrétisation. Elle est donc inévitable et son retrait permet d'obtenir des résultats précis sur des maillages grossiers. Une économie importante en temps de calcul est alors réalisée. Les causes principales de la traînée étant connues, il est alors possible de cibler où concentrer les efforts d'optimisation.

Une fois qu'une méthode de décomposition applicable en mode motorisé est obtenue, il sera possible de développer une formulation pour la prédiction et la décomposition de la traînée d'installation. Ceci sera utile puisque, depuis quelques années, plusieurs facteurs tels l'économie d'énergie et les nouvelles lois restraignant le bruit poussent les avionneurs ainsi que les motoristes à opter pour des configurations de turbosoufflantes à hauts taux de dilution. Par contre, un inconvénient majeur de ce changement est l'augmentation de la traînée d'installation. Les nacelles étant plus grosses, elles offrent une plus grande résistance à l'air et influencent plus l'aérodynamisme de l'aile. L'optimisation de la position des nacelles est donc devenue importante pour réduire la traînée d'installation motrice. Même avec l'utilisation de la CFD, la prédiction de cette traînée demeure un processus qui présente des difficultés qui sont détaillées dans ce document.

L'objectif principal de cette thèse est d'obtenir une décomposition de la traînée sur une configuration d'avion complète motorisée, c'est-à-dire comprenant le fuselage, les ailes, ainsi que des moteurs en régime de poussée. De nos jours, les méthodes permettant une telle décomposition en régime non-motorisé ont été largement utilisées, mais l'ajout de moteurs complique l'analyse. En effet, dans le cas d'une installation motrice, il est en général requis de séparer les forces produites sur l'extérieur des nacelles de celles produites à l'intérieur, ces dernières étant de la responsabilité du motoriste plutôt que de l'avionneur. De plus, la présence des moteurs ajoute des termes de poussée, dont la force de captation, qui sont difficiles à évaluer par une méthode champ proche classique. Finalement, une intégration des forces de pression et de frottement sur la surface d'un avion en régime de poussée ne permet pas le calcul de la traînée. La surface d'intégration comprend les conditions limites d'entrée et de sortie du moteur qui injectent de la quantité de mouvement à l'écoulement ce qui produit une force de poussée. Une intégration champ proche ne donne que la force nette propulsive subie par l'avion sans permettre l'évaluation de la poussée ni de la traînée.

Le présent ouvrage se divise en six sections: une revue de la littérature, une explication de la démarche adoptée, les contributions scientifiques proposées se divisant en trois chapitres ainsi qu'une discussion générale sur l'ensemble du travail. La revue de littérature se divise en deux parties. La première traite du calcul de la traînée par la méthode champ lointain tandis que la seconde discute de la comptabilité traînée/poussée. Les éléments rendant difficile la séparation des traînées externe et interne et les méthodes de calcul de la poussée y sont expliqués. Cette thèse inclut dans le corps du texte le contenu de trois articles scientifiques. La théorie derrière les méthodes employées et développées y est donc détaillée au fur et à mesure dans les chapitres 4 à 6. Ces trois articles constituent trois contributions distinctes mais dépendantes l'une de l'autre. Chacun des trois articles présente donc une méthode dont les résultats sont présentés et validés. Une discussion sur l'ensemble du travail sera présentée au Chapitre 7.

CHAPITRE 2 REVUE CRITIQUE DE LA LITTÉRATURE

2.1 Introduction

La prédiction de la traînée d'un avion est d'une grande importance. La minimisation de la traînée permet de réduire la consommation de carburant, donc de réduire les coûts d'opération ainsi que la pollution atmosphérique. Depuis les débuts de l'aéronautique, la prédiction de cette traînée fait l'objet d'une importante attention de la part de la communauté scientifique. Autrefois, seuls les essais en soufflerie et en vol permettaient d'estimer cette force. Depuis l'avènement du calcul scientifique, un nouveau joueur est apparu: la mécanique des fluides assistée par ordinateur (CFD). Cependant, cette dernière méthode n'a pas toujours eu bonne presse, même qu'en 1985, Sloof [5] s'interrogea à savoir s'il était possible d'obtenir des valeurs de traînée cohérentes par l'intermédiaire de la mécanique des fluides numérique.

Aujourd'hui, la CFD connait un succès remarquable dans le monde de l'aéronautique. D'ailleurs en industrie, pour plusieurs étapes de conception, la CFD est le seul outil de travail et les essais en soufflerie ont été mis de côté. Une grande diminution du coût de conception y est alors associée, avec de surcroît une augmentation de l'efficacité de l'appareil.

Si la CFD réussit dans un domaine, elle n'est cependant pas la réponse à tout. Un aspect causant toujours de la difficulté est la prédiction de la traînée d'installation, c'est-à-dire lorsque les moteurs sont ajoutés au modèle. Afin de simuler adéquatement une telle configuration, une distinction claire doit être faite entre les forces appartenant à la poussée et les forces liées à la traînée. Ce domaine se nomme "Thrust/Drag Bookkeeping", ou comptabilité Traînée/Poussée.

Le présent chapitre vise à introduire le lecteur aux connaissances actuelles de l'état de l'art dans ces deux domaines. Ce chapitre se divise en deux parties. Dans un premier temps, une revue des méthodes de prédiction de traînée est présentée. Par la suite, il sera traité de la comptabilité traînée/poussée des configurations motorisées.

2.2 Calcul de la traînée

2.2.1 Généralités

Il existe deux méthodes pour l'évaluation de la traînée: la méthode champ proche ou *Near-Field* (NF) et la méthode champ lointain ou *Far-Field* (FF). La première est l'approche la plus répandue et consiste à intégrer les forces de frottement et de pression sur la surface de

l'avion comme suit:

$$\mathrm{D_{NF}} = \mathrm{D_p} + \mathrm{D_f} = \int_{S_{Avion}} [(p - p_\infty)n_x - (\vec{\tau_x} \cdot \vec{n})]\, dS \tag{2.1}$$

Il s'agit d'une décomposition de type mécanique. Nous obtenons la valeur totale de la traînée sur le corps étudié. En 1938, Betz [6] apporta une autre idée, celle d'étudier le sillage en aval du modèle. Cette idée, basée sur le principe d'action-réaction de Newton et de la conservation de la quantité de mouvement, est à l'origine de la méthode de champ lointain. Elle se base sur le fait que si le fluide exerce une force sur l'avion, alors l'avion doit également exercer une force sur le fluide. Ces deux forces doivent être égales, mais de signes opposés tel que montré à l'Équation 2.2. L'intégrale se fait sur une surface externe entourant l'avion. Tous les phénomènes physiques doivent être contenus dans le volume délimité par cette surface. Par exemple, l'onde de choc doit être comprise dans ce volume.

$$\mathrm{D_{FF}} = -\mathrm{D_{NF}} = \int_{S_{Externe}} [-\rho(u - u_\infty)(\vec{q} \cdot \vec{n}) - (p - p_\infty)n_x + (\vec{\tau_x} \cdot \vec{n})]\, dS \tag{2.2}$$

Maskell [7] développa davantage la formulation de Betz afin de permettre la décomposition entre traînée de profil et traînée induite. Par la suite, Kusunose et al. [8] développèrent une méthode afin d'extraire la traînée d'onde de la traînée de profil basée sur des études de sillages.

La décomposition de la traînée en composantes physiques, soient les traînées d'onde, visqueuse et induite, associées respectivement aux phénomènes de choc, de couche limite et de création de portance, est importante. La Figure 2.1 résume les différentes approches. Une telle décomposition permet d'identifier les lacunes d'un design et permet aux ingénieurs de savoir où placer l'emphase afin de minimiser la traînée. Un des avantages de l'approche champ lointain est qu'elle permet aussi l'extraction de traînée numérique, ou *spurious drag*, engendrée par l'ajout de dissipation artificielle dans les solveurs et par les erreurs de discrétisation. Nous parlerons de ce phénomène plus en détails dans les sections à venir. Il existe d'autres façons de produire une décomposition physique, par l'intermédiaire de méthodes empiriques [9–11]. Ces dernières ont fait leurs preuves au cours des années et sont d'ailleurs toujours utilisées. Par contre, elles servent surtout en design conceptuel et ne peuvent mener à des optimisations fines des designs. De plus, elles ne peuvent plus être utilisées sur des configurations innovantes, comme l'aile volante, car les corrélations n'y sont pas adaptées.

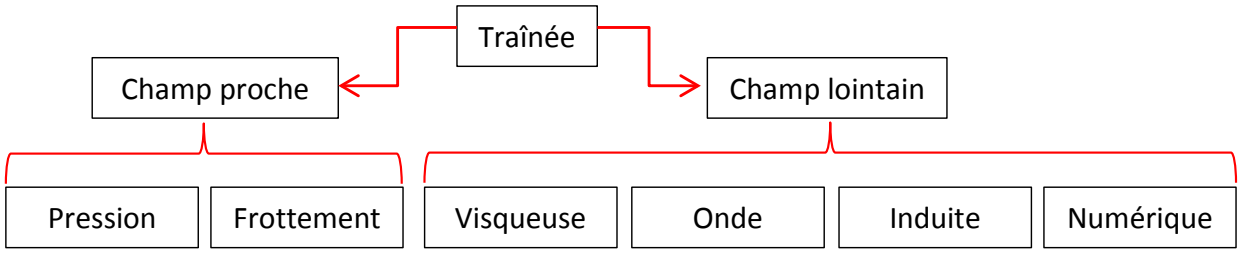

Figure 2.1 Méthodes et types de décomposition

2.2.2 Méthode champ lointain en numérique

C'est en 1990 que Van Der Vooren et al. [12] transposèrent la méthode du milieu expérimental au milieu numérique en proposant la première formulation de la méthode de champ lointain applicable au solveur CFD. La méthode fut d'abord utilisée sur les écoulements potentiels par Destarac [13] puis transposée aux écoulements Euler par van Dam et al. [14]. Dans ces deux publications, la traînée d'onde est respectivement mesurée par la chute de quantité de mouvement, vu l'absence d'entropie des solveurs potentiels, et par le saut d'entropie à travers le choc. Une autre contribution de Destarac [13] est la première utilisation de senseurs pour le choix des zones d'intégration. Les cellules supersoniques sont identifées en se basant sur la vitesse locale et elles définissent le contour à intégrer. En 1999, Lovely et al. [15] proposèrent un senseur permettant une identification automatique des cellules constituant la zone du choc et Tognaccini [16] développa un senseur permettant la sélection des cellules de la couche limite. En l'absence de viscosité, la traînée de profil est composée uniquement de la traînée d'onde et le régime Navier-Stokes ajoute la traînée visqueuse. Un problème persiste: les traînées d'onde et visqueuse sont toutes deux caractérisées par une augmentation de l'entropie. On doit alors déterminer comment décomposer ces deux traînées. Cummings et al. [17] furent les premiers à répondre à cette question en effectuant la première décomposition en champ lointain en régime RANS. Schmitt et al. [18] répétèrent cette tâche en utilisant la formule d'Oswatitsch [19], qui développa une équation exprimant la vitesse dans le plan de Trefftz en fonction de l'entropie pour les traînées induite et d'onde. Ils notèrent un phénomène: la traînée induite diminue au fur et à mesure qu'ils reculent le plan d'intégration. Ils expliquèrent leur observation par l'accroissement trop rapide des cellules du maillage dans le champ lointain qui cause une diffusion accélérée des tourbillons. Ils proposèrent une correction pour remédier à cette faiblesse. Cependant, une astuce beaucoup plus simple fut proposée par Laurendeau et al. [20]. Il s'agit de limiter le volume d'intégration très près de la configuration analysée afin d'éviter la dissipation des tourbillons. Une autre

solution fut apportée par Veilleux et al. [21, 22] qui consiste à obtenir la traînée induite en soustrayant les autres composantes de la traînée totale. Ces autres traînées (onde et visqueuse) étant moins sensibles à la dissipation, la prédiction de la traînée induite s'en trouve améliorée.

Au début, la méthode champ lointain appliquée aux solutions numériques était très similaire à son application aux souffleries [23, 24]. C'est en 2003 que Destarac [25] proposa de séparer le vecteur de la quantité de mouvement en deux composantes afin de séparer la traînée réversible, soit la traînée induite, des traînées irréversibles, soient les traînées d'onde et visqueuse. Notez qu'un phénomène thermodynamique est qualifié de réversible s'il n'occasionne aucun changement d'entropie tout en étant adiabatique. Il proposa d'intégrer ces deux vecteurs dans les zones de choc et de couche limite donnant lieu aux trois composantes principales de la traînée. Cependant, il ajouta une correction pour tenir compte de la traînée numérique. Le vecteur irréversible devra donc être intégré sur les zones de choc et de couche limite, mais aussi sur le complément du domaine. Dans cette région, l'écoulement est réputé isentropique et si ce n'est pas le cas, la traînée est non-physique et doit nécessairement être numérique. Pour la traînée induite, on doit dorénavant intégrer le vecteur réversible sur tout le domaine, y compris la zone où l'écoulement est réputé isentropique. Notez que Destarac [25] utilise la formulation exacte du déficit de vitesse axiale, la différence entre la vitesse mesurée à un endroit donné et la vitesse à l'infini amont, car la formule d'Oswatitsh [19] a été prouvée inadéquate par Paparone [26] lorsqu'appliquée aux écoulements visqueux.

L'extraction de la traînée numérique permet l'utilisation de méthodes de maillage automatiques, plus efficaces, mais générant des mailles parfois de moins bonne qualité du point de vue de l'orthogonalité et du raffinement. Une simulation sur de telles grilles est plus difficile à converger et requiert l'ajout d'une plus grande quantité de dissipation artificielle ce qui rend le calcul de la traînée moins précis par la méthode champ proche. Esquieu [27] et Yamazaki et al. [28] ont obtenu, par la méthode champ lointain, de bonnes prédictions en utilisant respectivement les "patched grids" et des maillages non structurés. Par la suite, plusieurs auteurs ont utilisé la méthode champ lointain [27, 29–32], et Yamazaki et al. [33] ont utilisé le potentiel de détection de la traînée numérique pour développer une méthode de raffinement automatique basée sur ce critère.

Un des inconvénients de la formulation exacte du déficit de vitesse axiale est qu'elle est non définie lorsque la perte de pression totale est importante, ce qui est généralement le cas dans les zones de décrochage. Lorsqu'un avion en régime de croisière est étudié, cette limitation n'affecte que quelques cellules, ne changeant que très peu le résultat final. Cependant, si une

zone de décollement de la couche limite est présente, la méthode champ lointain ne peut être appliquée. Récemment, Gariépy et al. [34] ont proposé une nouvelle formulation du déficit de vitesse axiale valide dans tous les cas. La méthode champ lointain ne s'en retrouve que plus précise, car maintenant toutes les cellules d'un maillage sont comptabilisées.

2.3 Configuration motorisée

2.3.1 Comptabilité Traînée/Poussée

Un des aspects ayant reçu moins d'attention de la communauté numérique au cours des années est la prédiction de la traînée en configuration motorisée. Les lignes suivantes dressent l'état de l'art de ce domaine. Le but ultime est d'être en mesure de séparer les forces agissantes sur un avion. Les forces appartiennent soit à la traînée ou à la poussée et la séparation doit être claire. En fait, tout comme les bilans financiers, il existe une multitude de méthodes. L'important est de bien définir la méthodologie employée. Les références [3, 35] expliquent les règles d'une telle séparation et expriment la force résultante F_{EX} appliquée sur un avion par l'équation suivante:

$$F_{EX} = F_{IPF} - D_{AFS} \tag{2.3}$$

Les deux termes de droite représentent respectivement la force propulsive F_{IPF} et la traînée totale de l'avion D_{AFS}. Ils se décomposent comme suit:

$$F_{IPF} = F_N + \Delta F_{INL} + \Delta F_{EXH} + \Delta F_{TRIM} \tag{2.4}$$

$$D_{AFS} = D_{REF} - \Delta D_{INL} - \Delta D_{EXH} - \Delta D_{TRIM} - \Delta D_{RN} \tag{2.5}$$

Il est à noter que les termes en Δ représentent des corrections qui sont négligées dans le cadre de ce travail. Dans tous les cas, ils se détaillent comme suit:

- F_N: Force nette générée par les moteurs (voir Section 2.3.2)
- $\Delta F_{INL}/\Delta D_{INL}$: Variation de la force causée par un changement des conditions d'opération à l'entrée des moteurs
- $\Delta F_{EXH}/\Delta D_{EXH}$: Variation de la force causée par un changement des conditions d'opération à la sortie des moteurs

- $\Delta F_{TRIM}/\Delta D_{TRIM}$: Variation causée par un changement dans la position des surfaces de contrôle
- D_{REF}: Traînée de la configuration
- ΔD_{RN}: Variation de la traînée causée par un changement du nombre de Reynolds ou variation entre un essai en soufflerie et un essai en vol.

L'approche générale est de choisir des conditions d'opération de référence. Ces conditions donnent lieu à une traînée de référence D_{REF} et à une poussée nette des moteurs F_N. Les autres termes comprennent des corrections faites aux forces de référence causées par des changements de conditions d'opération. Par exemple, la température ambiante de l'avion en vol est différente de la température à l'intérieur de la soufflerie.

Dans ce travail, l'avion est étudié aux conditions de référence. C'est-à-dire que les termes de corrections seront tous négligés. L'Équation 2.3 peut donc se résumer comme suit:

$$F_{EX} = F_N - D_{REF} \tag{2.6}$$

2.3.2 Poussée

Dans le cas d'un moteur à double jet, il est habituel de numéroter les sections du moteur selon la Figure 2.2.

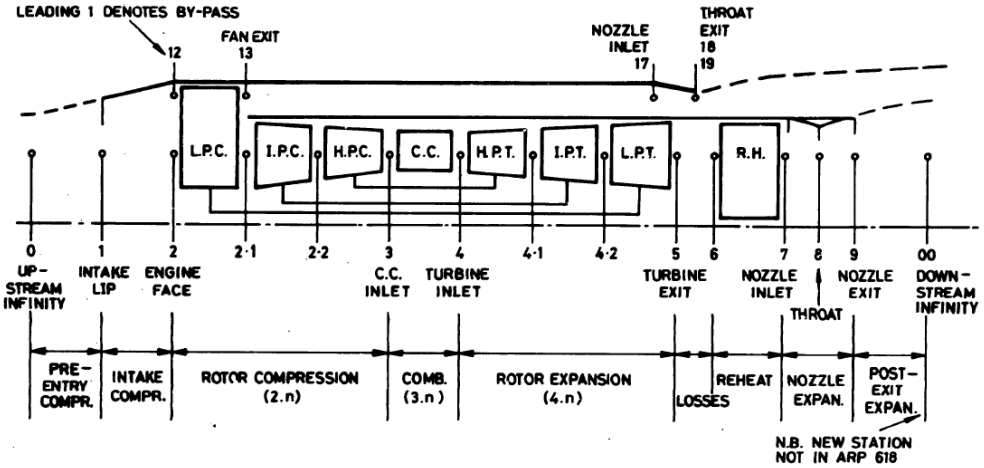

Figure 2.2 Numérotation des stations [1]

Suivant une telle numérotation, la poussée s'exprime comme suit [3]:

$$F_N = F_{G_9} + F_{G_{19}} - F_{G_0} \tag{2.7}$$

C'est en fait la différence entre l'impulsion F_G évaluée aux différentes stations. Notez que l'indice 0 représente l'infini amont. L'impulsion à la station "i" est donnée par:

$$F_{G_i} = \dot{m}_i V_i + A_i (p_i - p_0) \tag{2.8}$$

où A_i est l'aire de la section du tube de courant, $\dot{m}_i$ et V_i sont respectivement le débit massique et la vitesse de l'écoulement traversant cette section et p_i et p_0 sont respectivement les pressions statiques dans la section du tube de courant et à l'infini amont. Dans le cas d'un moteur à un seul flux (absence de soufflante), les termes avec l'indice 19 disparaissent.

Pour la traînée, elle est généralement prédite par des essais en soufflerie où les moteurs sont remplacés par des nacelles vides *Through Flow Nacelles* (TFN) ou encore des *Turbo Powered Simulator* (TPS) simulant le comportement d'un vrai moteur [4,36], mais avec un écoulement froid. Ces imitations de moteurs ajoutent une traînée supplémentaire générée par le passage de l'air à l'intérieur, la traînée interne, qui doit être retirée. Une autre problématique à laquelle se heurtent les ingénieurs apparaît. Il s'agit de la quantification de ce qui est appelé la traînée d'installation motrice. La traînée des moteurs seuls ainsi que la traînée de l'avion sans moteur sont connues, mais la traînée avion-moteurs est différente de l'addition des forces séparées. Cette variation constitue la traînée d'interférence, pouvant être positive ou négative, qui est une des composantes de la traînée d'installation.

2.3.3 Expérimental

Dans le milieu expérimental, beaucoup d'efforts ont été mis afin de déterminer la traînée d'installation. Les étapes de la comptabilité traînée/poussée sont expliquées dans plusieurs travaux [4, 36–41]. C'est un processus fastidieux qui implique plusieurs essais pour plusieurs configurations. Cette section décrit les méthodes utilisées dans le milieu expérimental. Elle se divise en deux sous-sections. La première traite des essais effectués sur des nacelles isolées tandis que la seconde concerne les avions complets.

Nacelle

Afin de déterminer la force de captation, des études sur le moteur seul sont effectuées [2]. La méthode la plus utilisée consiste à employer deux différents essais en soufflerie. Le premier avec une TFN et le second avec une *Blow-Through Nacelle* (BTN). Les Figures 2.3 et 2.4 [2]

illustrent un exemple des essais effectués.

La traînée interne est déterminée par la BTN (Figure 2.4) où la région des points de stagnation n'est volontairement pas simulée afin d'éviter le décollement de la couche limite causée par un changement abrupte de l'inclinaison des parois. La traînée interne est finalement mesurée par un bilan de quantité de mouvement entre l'entrée et la sortie. Une série de corrections doivent être faites pour conserver le même débit massique entre les tests BTN et TFN. Les *annular blockers* servent à ajuster le débit et donc à modifier le MFR. La force de captation est donc calculée à partir du TFN par la différence entre la traînée externe à un débit réduit et au débit de design.

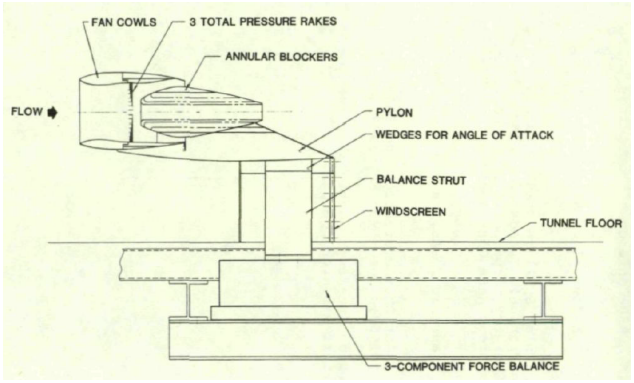

Figure 2.3 Essai sur nacelles TFN [2]

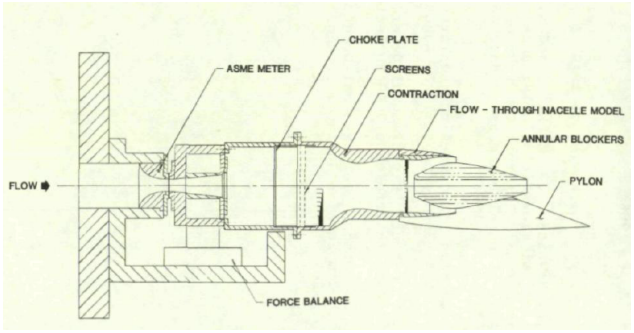

Figure 2.4 Essai sur nacelles BTN [2]

Ces tests ne servent cependant qu'à déterminer les performances reliées au moteur. D'autres types de nacelles sont employés afin de simuler des phénomènes plus spécifiques, tel l'effet des jets sur le reste de l'avion. La Figure 2.5 représente les différents types de nacelles pouvant être utilisés lorsqu'attachés sur une configuration d'avion en soufflerie.

Elles sont illustrées de la plus simple (TFN) à la plus complexe (TPS). Il est à noter que malgré l'absence de l'effet de la température, la TPS est l'outil expérimental simulant le

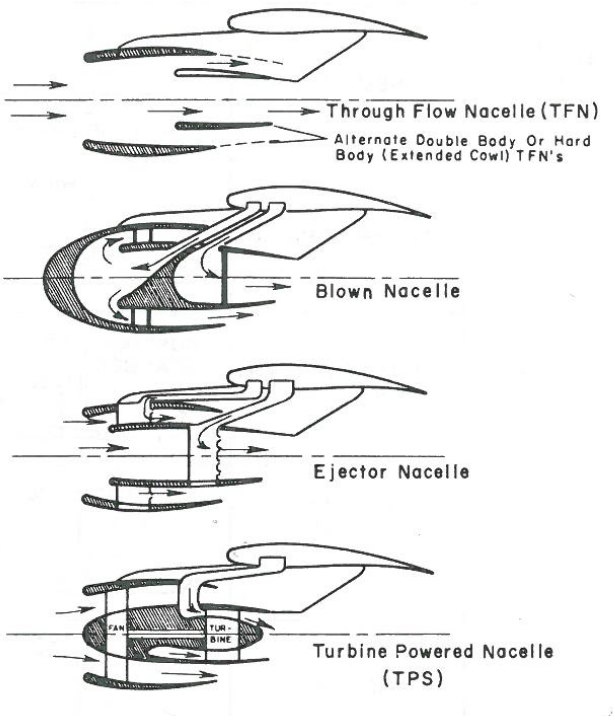

Figure 2.5 Nacelles employées en soufflerie [3]

mieux un moteur réel. Elle est cependant la plus coûteuse et la plus sensible aux erreurs expérimentales. La Figure 2.6 nous montre des exemples de TPS. Ce sont, en fait, des moteurs à échelle réduite, mais sans chambre de combustion. Outre le prix, un des désavantages des TPS est qu'elle ne simule pas la température du jet. De plus, la calibration d'un tel dipositif est très complexe [42].

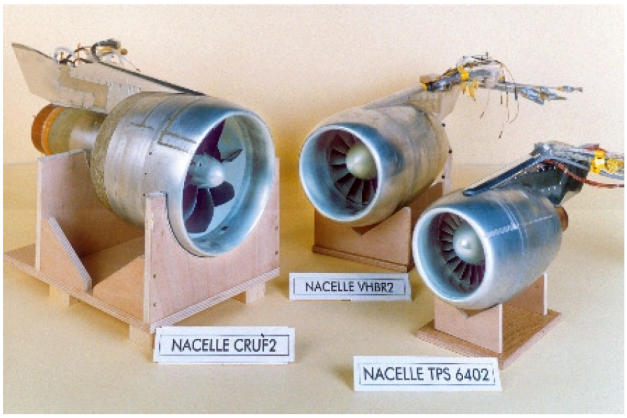

Figure 2.6 Turbo-Powered Simulator [4]

La Figure 2.7 [3] nous montre les divers types d'essais pouvant être effectués, chacun présen-

tant des avantages et des inconvénients. Une combinaison de plusieurs de ces essais est requise afin de déterminer de manière précise et sans ambiguité la traînée associée à chaque composant et la traînée d'installation motrice.

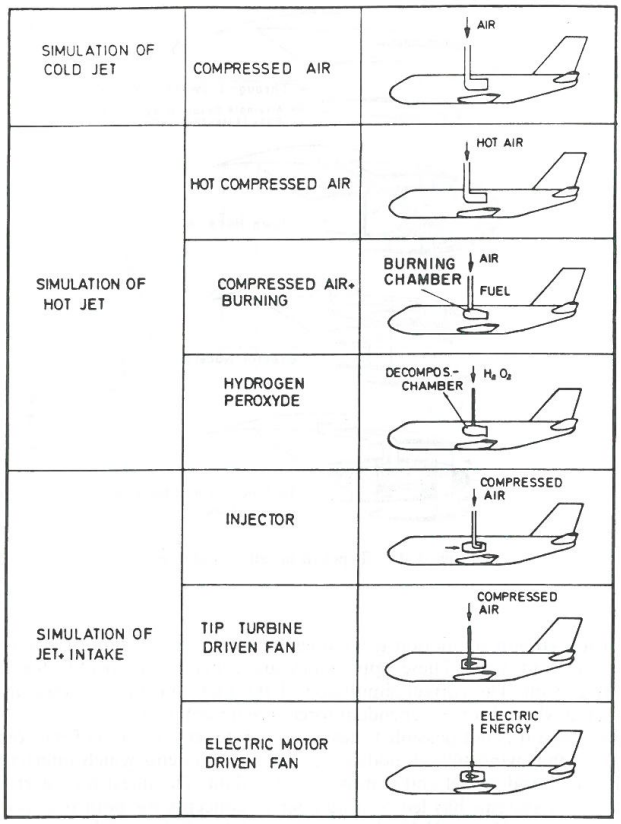

Figure 2.7 Simulation des jets

Configuration complète

La prochaine étape consiste à déterminer la traînée d'installation. Des essais sont faits sur un avion sans moteur et puis avec ses moteurs. Dans le cas de l'utilisation de nacelles vides (TFN), la traînée d'installation est calculée par l'équation suivante:

$$D_{\text{Installation}} = D_{\text{Moteurs inclus}} - D_{\text{Moteurs exclus}} - D_{\text{Interne}} \tag{2.9}$$

La Figure 2.8 [3] nous permet de visualiser les phénomènes responsables de cette traînée. L'aile influence l'écoulement autour du moteur et vice-versa. Le jet change la distribution de pression sur l'arrière de la nacelle, le pylon ainsi qu'une partie de l'aile. Tous ces phénomènes sont couplés et indissociables, ce qui pousse les ingénieurs à discrétiser les essais en soufflerie

de manière à quantifier ces phénomènes d'interférence. Les lignes qui suivent citent quelques exemples de cette pratique.

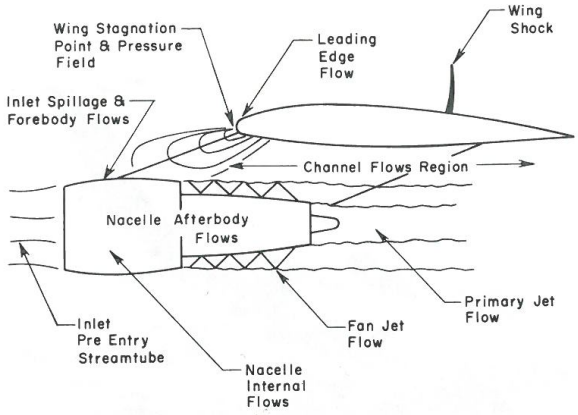

Figure 2.8 Interation aile-moteur-pylon [3]

En général, au minimum trois modèles sont requis. Le premier sert à calculer les forces et moments en jeu (Figure 2.9(a)). Le second ne modélise que la partie avant (inlet) de l'avion (Figure 2.9(b)). Le dernier simule la partie arrière et les effets des jets (Figure 2.9(c)).

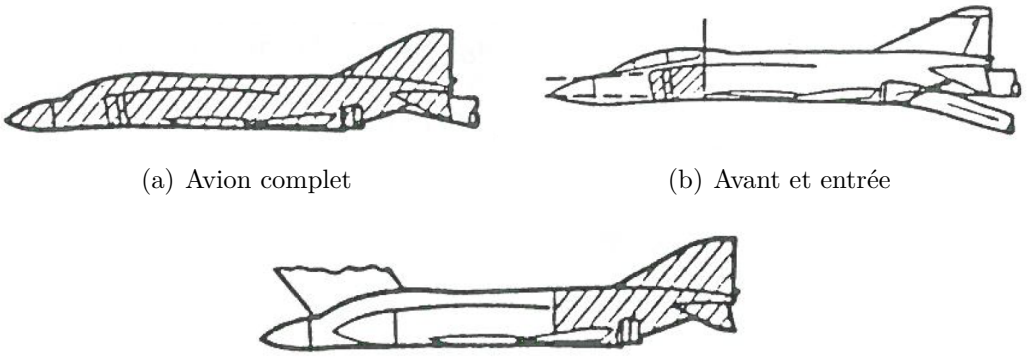

(a) Avion complet

(b) Avant et entrée

(c) Arrière et sortie

Figure 2.9 Simulation typique [3]

Un autre exemple est illustré sur la Figure 2.10. Chaque étape présente un incrément par rapport à la précédente. Premièrement, la traînée de la configuration lisse est étudiée (Figure. 2.10(a)). L'interaction aile-moteur est représentée par l'essai avec des nacelles vides (Figure. 2.10(b)). Par la suite, les effets des jets sont étudiés par des nacelles soufflées (Figure. 2.10(c)). Finalement, la nacelle seule est isolée de manière à retirer la traînée interne

(Figure. 2.10(d)) tel qu'expliqué à la section précédente. On peut résumer les divers essais correspondants aux diverses traînées par la Figure 2.11. Nous voyons que chaque essai apporte un nouvel élément et améliore la prédiction de la traînée d'installation.

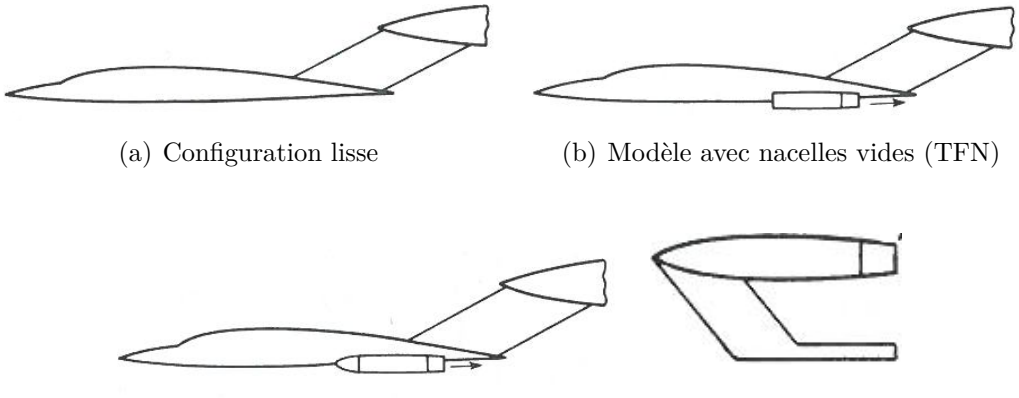

(a) Configuration lisse (b) Modèle avec nacelles vides (TFN)

(c) Modèle avec nacelles soufflées (BN) (d) Nacelle isolée

Figure 2.10 Simulations typiques [3]

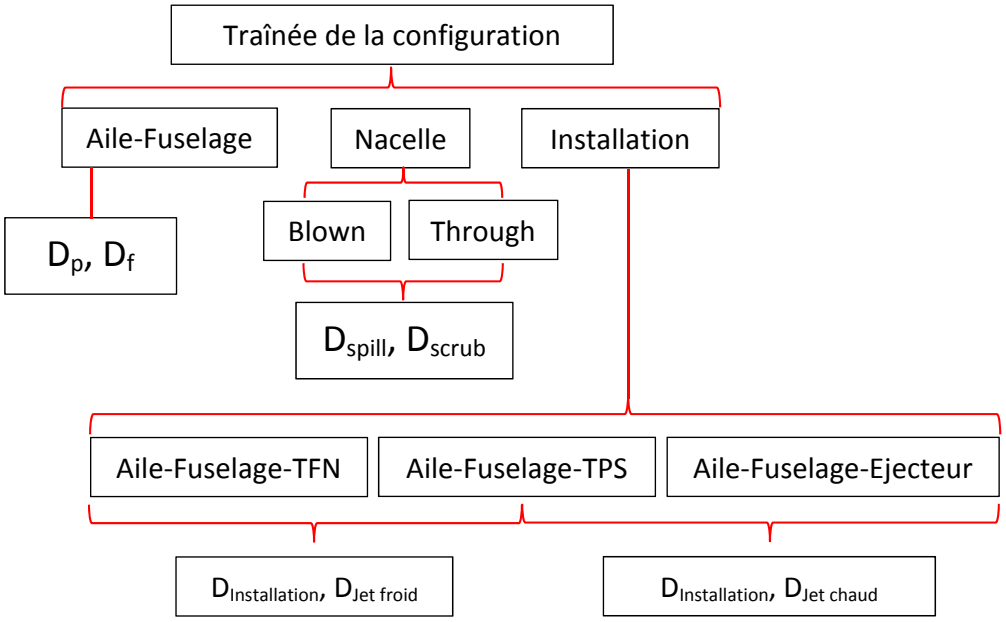

Figure 2.11 Composantes de la traînée d'une configuration par méthode expérimentale

2.3.4 Numérique

Un des premiers à écrire sur ce sujet et à poser les bases de la comptabilité traînée/poussée dans le domaine numérique est Tognaccini [16]. Esquieu [43] nomme les quatre contributions principales d'ajout de traînée en présence de moteur:

- Traînée visqueuse de la nacelle
- Traînée visqueuse du pylon
- Ajout de traînée induite
- Traînée de choc présente sur la nacelle

Ogoshi et al. [44] ainsi que Méheut et al. [45] ont montré, par une étude de sillage en soufflerie, que la première contribution est celle qui a le plus grand impact. Afin de déterminer la traînée d'installation motrice, Brodersen et al. [37] calculent cette force tout comme lors des essais expérimentaux, c'est-à-dire en suivant l'Équation 2.9.

La principale contribution dans ce domaine à ce jour a été faite par Van der Vooren et Destarac [46] qui proposèrent une méthode afin de calculer la traînée de configuration, soit la traînée totale avec moteurs inclus. Dans leurs travaux, la traînée d'installation est calculée, mais elle n'est pas décomposée.

La revue de littérature démontre qu'en date d'aujourd'hui, la comptabilité traînée/poussée représente toujours un défi de taille autant d'un point de vue expérimental que numérique. Le présent travail vise à développer et valider des méthodes d'analyse CFD basées sur l'approche champ lointain pour la comptabilité traînée/poussée comme outil d'analyse permettant de remplacer et complémenter, du moins en partie, les essais en soufflerie. Ces méthodes pourront ensuite être appliquées au calcul de la traînée d'installation ou d'interférence moteurs/avion.

CHAPITRE 3 DÉMARCHE

3.1 Mise en contexte

L'objectif principal de cette thèse est de décomposer et de quantifier les traînées d'installation motrice et d'interférence aile/moteur lorsque les moteurs sont en régime de poussée. L'utilisation de la technique d'intégration classique des forces de pression et de frottement (champ proche) n'est plus adéquate dans cette situation car la surface d'intégration comprend les conditions limites S_{in} et S_{out} illustrées sur la Figure 3.1. Ces surfaces sont situées à l'intérieur de la nacelle et produisent la poussée en ajoutant de la quantité de mouvement à l'écoulement. Par conséquent, la méthode champ proche ne sert qu'à calculer la force nette subie par l'avion aux conditions de vols données. Dans le cas de création de poussée, cette force ne correspond donc plus à la traînée. Il est également impossible d'omettre ces deux plans car la surface d'intégration serait alors ouverte. De plus, dans l'état de l'art de la comptabilité traînée/poussée, la poussée standard nette est utilisée [1, 3] et correspond à la variation de quantité de mouvement entre la surface infinie amont $S_{-\infty}$ et la surface de sortie S_{exit}. La variation de quantité de mouvement entre S_{in} et S_{out} correspond à la poussée de base [46]. Une solution possible permettant l'évaluation de la traînée est l'utilisation de la méthode champ lointain.

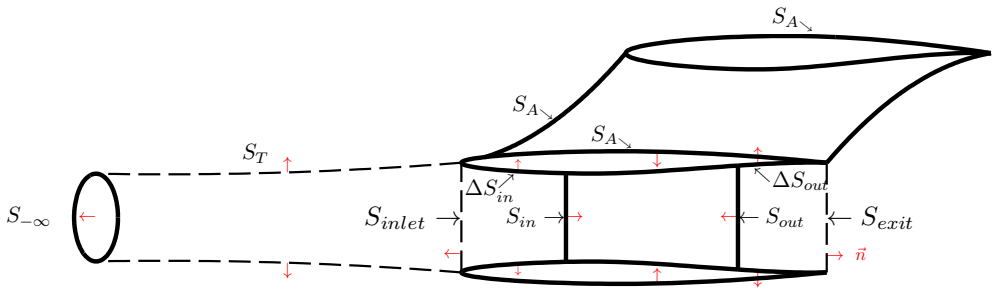

Figure 3.1 Surfaces d'une nacelle

Le coeur de cette thèse consiste donc à développer une méthodologie permettant la quantification et la décomposition des traînées d'installation et d'interférence aile/moteur ce qui, à la connaissance de l'auteur, n'a jamais été fait jusqu'à présent. Van der Vooren et Destarac [46] ont proposé une formulation de la traînée lorsque de la poussée est générée. La traînée de configuration D_c s'exprime donc comme suit:

$$D_c = D_v + D_w + D_{sp} + D_i - D_{tf} - D_{scrub} + T_{Pre} \tag{3.1}$$

où les indices *v*, *w*, *sp*, et *i* correspondent respectivement aux composantes visqueuse, d'onde, numérique et induite. D_{tf} représente l'ajout de traînée irréversible par le passage de l'écoulement à l'intérieur des moteurs. Van der Vooren et Destarac [46] ont proposé une formulation pour quantifier cette traînée. L'évaluation des deux derniers termes, soit la traînée interne D_{scrub} et la force de captation T_{Pre}, ne peut, qu'à ce jour, s'effectuer que par une intégration de type champ proche. Ils représentent respectivement la variation de quantité de mouvement entre les surfaces $S_{-\infty}$ et S_{inlet} et entre les surfaces S_{inlet} et S_{exit}. L'intégration de la quantité de mouvement sur la surface S_{inlet} est hautement sensible en raison des forts gradients de pression à cet endroit.

Les deux premières contributions de cette thèse visent à développer une formulation de la traînée interne et de la force de captation qui n'est pas fonction de l'intégration sur S_{inlet}. La troisième contribution propose une méthode permettant la décomposition des traînées d'installation et d'interférence. Les trois contributions sont expliquées plus en détails dans le texte qui suit.

3.2 Traînée interne

Cette force est difficilement évaluable par la méthode classique d'intégration des forces de pression et de frottement car la surface ainsi créée, soit l'intérieur de la nacelle, est une surface ouverte. Pour contourner cette problématique, la méthode de champ lointain est employée. Sa propriété permettant de découper le volume de calcul en sous-volumes selon les phénomènes physiques créateurs de traînée peut être appliquée afin d'effectuer une division de ce même volume, mais basée sur des critères géométriques au lieu de fluidiques. Pour la traînée interne, le volume de contrôle est divisé en deux sections, soient l'intérieur et l'extérieur de la nacelle. Le calcul des traînées, visqueuse, numérique et d'onde a donc été effectué uniquement dans le volume interne ce qui a permis d'évaluer la traînée interne. Le développement de cette méthode a fait l'objet d'un article scientifique intitulé *Internal Drag Evaluation for a Through-Flow Nacelle Using a Far-Field Approach* [47] qui a été publié dans le *Journal of Aircraft* de l'*American Insitute of Aeronautics and Astronautics* en 2015. Le contenu intégral de cet article est présenté au Chapitre 4 de cette thèse.

3.3 Force de captation

Un aspect très important de la comptabilité traînée-poussée est le choix de la définition de la poussée. La force nette agissant sur la configuration correspond à la traînée moins la poussée. Elle reste inchangée pour des conditions de vol et des paramètres moteur donnés. Cependant, la valeur de la traînée se verra modifiée selon la définition de la poussée employée dans le système de comptabilité. La poussée standard nette, ou *standard net thrust*, T_N est habituellement choisie [1,3] . L'inconvénient est que la force de captation T_{Pre} apparaît alors dans le calcul de la traînée de configuration D_c (voir Éq. (3.1)). Cette poussée se calcule soit en intégrant les forces de pressions agissant sur la paroi externe du tube de courant capté par le moteur, soit en intégrant la variation de quantité de mouvement entre une surface transversale située à l'extrémité amont de ce tube de courant et la surface définie par la ligne de stagnation qui correspond à l'intersection entre la nacelle et le tube de courant. Dans les deux cas, la pression doit être connue sur la ligne de stagnation. Hors, les gradients de pressions sont très importants à cet endroit et la moindre erreur d'évaluation de la pression engendrerait un résultat erroné de la force de captation. L'idée novatrice qui est proposée est d'utiliser la surface interne de la nacelle qui correspond à la condition limite de sortie de pression (*pressure outlet*) S_{in} (voir Fig. 3.1). L'avantage est que les propriétés telles que la pression et la vitesse sont connues et aucune interpolation n'est donc nécessaire. Pour calculer la force de captation, il suffit d'intégrer la différence de quantité de mouvement entre la surface infinie amont $S_{-\infty}$ du tube de courant et la face d'entrée interne de la nacelle S_{in}. Cependant, ce résultat n'est pas exact, car il faut retirer la variation de quantité de mouvement causée par le passage de l'écoulement à l'intérieur de la nacelle entre la surface de stagnation S_{inlet} et la face S_{in}. Cette variation correspond à la traînée de la portion de la paroi interne de la nacelle située en amont de S_{in}. Pour l'évaluer, la méthode de champ lointain est utilisée. Tout comme expliqué dans le paragraphe précédent, il est possible de calculer la traînée dans un sous-volume géométrique. La technique développée dans le premier article est alors employée pour évaluer la traînée interne amont de la nacelle. La valeur de la force de captation est alors connue. Basée sur ce même principe, une méthode alternative pour calculer la poussée standard nette est également développée. Les développements de ces méthodes ont été présentés dans un article scientifique intitulé *Engine pre-entry thrust and standard net thrust evaluation based on the far-field method* [48] qui a été publié dans le *Aerospace Science and Technology* en 2015.

3.4 Traînée d'interférence

La troisième contribution consiste à utiliser les méthodes développées aux étapes précédentes afin d'évaluer et de décomposer la traînée d'installation motrice. Il est proposé de diviser cette force en deux composantes, soient la traînée de la nacelle isolée et la traînée d'interférence. Cette dernière est évaluée en soustrayant de la traînée aile-fuselage-pylon-nacelle la somme des traînées aile-fuselage et nacelle isolée. Ensuite, la méthode de champ lointain est employée, ce qui permet de décomposer la traînée d'interférence selon toutes les composantes comprises dans la traînée de configuration. À la connaissance de l'auteur, il s'agit de la première fois qu'une méthode est proposée afin de décomposer la traînée d'interférence. Pour la configuration étudiée, soit le DLR-F6 en régime de poussée, la traînée d'interférence de la configuration représente environ 20% de la traînée d'installation et est principalement constituée de la traînée visqueuse. La traînée d'installation représente près de 25% de la traînée totale et la composante majeure est également la traînée visqueuse ce qui est attendu vu l'ajout de surface mouillée que représente les moteurs. Une autre composante importante de la traînée d'installation est la force de captation. Cependant, il est important de noter que cette force est inexistante pour la configuration aile-fuselage vu l'absence de moteur. Finalement, la traînée d'interférence est nuisible aux performances, mais ce n'est pas nécessairement toujours le cas. Par exemple, il est possible que l'ajout de la nacelle contribue à la portance de sorte que l'angle d'attaque de l'avion doit être diminué afin de conserver un coefficient de portance constant. Le cas échéant, la traînée induite pourrait diminuer ce qui ferait en sorte que la traînée d'interférence serait bénéfique. Les résultats ainsi que le développement de cette technique ont fait l'objet d'un article scientifique intitulé *Installation and Interference Drag Decomposition via RANS Far-Field Methods* qui a été soumis à la revue *Aerospace Science and Technology* en Juillet 2015.

CHAPITRE 4 ARTICLE 1: Internal Drag Evaluation for a Through-Flow Nacelle Using a Far-Field Approach

Malouin, B., Gariépy, M., Trépanier, J. Y., and Laurendeau, É. (2015), Internal Drag Evaluation for a Through-Flow Nacelle Using a Far-Field Approach, Journal of Aircraft, ahead of print, pp. 1-11.

4.1 Abstract

The main objective of this research is to propose a method for decomposing the total drag of a nacelle into external, internal, and wake drag. From a bookkeeping agreement, the internal drag (i.e., the drag generated inside a nacelle) is the engine manufacturer's responsibility and is not to be included in the aircraft's total drag. Consequently, computing the internal drag is mandatory for the airframe and engine constructors concerned and can be achieved either experimentally or by computational-fluid-dynamics analysis. Up to now, aerodynamic engineers have used a near-field approach to compute the internal drag using computational-fluid-dynamics analysis, but this method has serious drawbacks, including its dependency on the accurate location of the stagnation line. The new method proposed here has been applied to multiple two- and three-dimensional test cases, and results show that it is independent of the location of the stagnation line and yields accurate results that agree well with experimental and empirical data. Results also show that the wake drag of a through-flow nacelle is caused by the flow passing through the nacelle and so needs to be added to the internal drag.

4.2 Introduction

Over the last two decades, environmental concerns and sky-rocketing fuel prices have led the aerospace industry toward the use of Very High Bypass Ratio and Ultra High Bypass Ratio turbofan engines (VHBR/UHBR), which are more powerful and more efficient than the earlier low bypass turbofan engines [49]. However, the gain in propulsive efficiency is reduced by the increase in the installation drag generated by larger pylons and nacelles, with their larger area and correspondingly larger wetted area, as well as greater interaction with other aerodynamic surfaces. As a result, the location of the engine is important and must be carefully chosen and optimized. Determining the engine installation drag is a very time-consuming task in both CFD and experimental studies, because many runs are usually

required. The installation drag $D_{Install}$ is calculated by subtracting the wing body drag (D_{WB}) and the internal drag ($D_{Internal}$) from the wing-body-pylon-nacelle drag (D_{WBPN}), as follows [37]:

$$D_{Install} = D_{WBPN} - D_{WB} - D_{Internal} \tag{4.1}$$

Consideration of the installation drag is important for airframers and engine manufacturers alike, since it is common practice to stipulate that the internal drag must not be considered to belong to the aircraft's total drag. However, to compute the installation drag, knowledge of the internal drag is required. The traditional method for computing the internal drag via CFD analysis is called the near-field approach, and consists of integrating the viscous and pressure forces acting inside the nacelle. However, computation of this drag for integration purposes requires that the interior and exterior surface be determined. Furthermore, once split, the integration surface is no longer closed. With the near-field method, integration can be achieved by locating the nacelle's stagnation line. We show later that the results with this method are strongly dependent on accurately locating this line.

The objective of this research is to propose a method for decomposing and quantifying external and internal drag. This method, which we refer to as the DQEID method in the remainder of the paper, is derived from the far-field approach proposed by Destarac in 2003 [25] and Van Der Vooren [12], and, as discussed in the next section, proposes the decomposition of drag from a thermodynamics point of view: the drag generated by irreversible processes, such as boundary layers and shocks, and the drag generated by reversible processes, such as wing tip vortices. One advantage of the far-field approach is that it allows the spurious drag, which is generally caused by the solver's artificial dissipation and by mesh stretching in the field, to be extracted. However, for the purposes of this research, the key advantage of the far-field approach is its ability to perform a volumetric integral over the physical zones of drag production. As we demonstrate later, the location of the stagnation line is irrelevant to the proposed DQEID method.

The theory behind the far-field method, and its adaptation to the proposed DQEID method, are presented in the next section. To test the validity of this method, multiple 2D and 3D cases are done. First, the method is applied on two airfoils, NACA0012 and RAE2822, which are viewed as 2D nacelles, to demonstrate that it is not sensitive to the stagnation line's location (or stagnation point in 2D). NACA0012 was chosen because of its symmetry, which allows us to know both the internal and external drag because the two are equal. Then, the method is applied to two nacelles, a thin cylindrical one and the CFM56 TFN. Again, the choice of the cylindrical nacelle is dictated by verification and validation needs, and various

comparisons are presented. However, validation of the CFM56 results is more difficult, since only a few experimental data are available. Since those data are subject to experimental error and to misinterpretation, another simulation is performed to reinforce the validation: the CFM56 nacelle plugged to a bellmouth inlet. With this configuration, it is possible to compute the internal drag coefficient, which serves as a reference value for validating the proposed DQEID method. Finally, a theoretical and a numerical investigation are performed to demonstrate that the wake drag of an TFN is caused by the generation of internal drag, and so needs to be added to the internal drag.

4.3 Theory

This section is divided into two parts. In the first part, we present the development of the far-field method. We also show how this method is used to evaluate drag. In the second part, we explain how this method is adapted to evaluate the internal drag.

4.3.1 Far-field method

The classical way to calculate drag is to integrate the pressure and friction forces acting on an immersed body. This is called the near-field method. Based on the principle of action-reaction, we know that the force exerted on the body by the flow is equal to the force exerted on the flow by the body, but with the opposite sign.

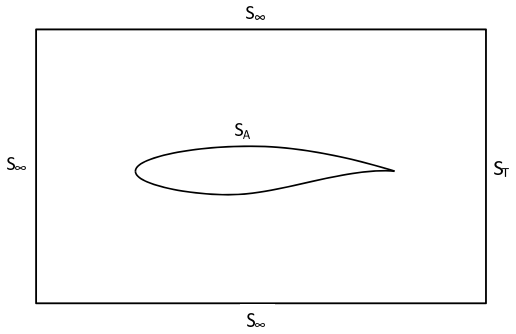

Figure 4.1 Control volume

Taking a control volume surrounding the configuration of interest, as depicted in Fig. 4.1, we can express the near-field drag $\mathrm{D_{NF}}$ as the integral of the momentum vector $\vec{f}$ on the control surface S_A, as follows:

$$\mathrm{D_{NF}} = -\int_{S_A} \left(\vec{f} \cdot \vec{n}\right) dS \tag{4.2}$$

where the momentum vector $\vec{f}$ is defined by:

$$\vec{f} = -\rho(u - u_\infty)\vec{q} - (p - p_\infty)\vec{i} + \vec{\tau_x} \tag{4.3}$$

Similarly, the far-field drag $\mathrm{D_{FF}}$ can be expressed as follows:

$$\mathrm{D_{FF}} = \int_{S_\infty \cup S_T} \left(\vec{f} \cdot \vec{n}\right) dS \tag{4.4}$$

Equation (4.4) corresponds to the generic form of the far-field drag and as such does not allow drag decomposition. Physical drag decomposition is based on the distinction between reversible and irreversible processes from a thermodynamics point of view [12,25]. Irreversible processes are associated with shock waves and boundary layers, while reversible processes are associated with wing tip vortices. To separate these terms, Destarac uses the axial velocity defect [25], $\Delta\bar{u} = \bar{u} - u_\infty$, associated with irreversible processes, as follows:

$$\Delta\bar{u} = u_\infty \sqrt{1 + 2\frac{\Delta H}{u_\infty^2} - \frac{2}{(\gamma - 1)M_\infty^2}\left[\left(e^{\frac{\Delta s}{R}}\right)^{\frac{\gamma-1}{\gamma}} - 1\right]} - u_\infty \tag{4.5}$$

where entropy variation from the free stream state Δs is given by:

$$\Delta s = \frac{R}{\gamma - 1} \log\left[\frac{p}{p_\infty}\left(\frac{\rho_\infty}{\rho}\right)^\gamma\right] \tag{4.6}$$

and enthalpy variation from the free stream state ΔH is given by:

$$\Delta H = \frac{\gamma}{\gamma - 1}\left(\frac{p}{\rho} - \frac{p_\infty}{\rho_\infty}\right) + \frac{u^2 + v^2 + w^2}{2} - \frac{u_\infty^2}{2} \tag{4.7}$$

However, it is not possible to define Eq. (4.5) when the total pressure loss becomes significant, since the value of the square root becomes negative in such cases. To overcome this problem, Gariepy et al. [34] propose a new formulation:

$$\Delta\bar{u} = u - u_\infty \left(\sqrt{1 + \frac{2\Delta H}{u_\infty^2} - \frac{2}{(\gamma - 1)M_\infty^2}\left[\left(\frac{p}{p_\infty}\right)^{\frac{\gamma-1}{\gamma}} - 1\right] - \frac{v^2 + w^2}{u_\infty^2}} + 1\right) \tag{4.8}$$

which leads to $\vec{f_{vw}}$, the irreversible portion of the momentum vector $\vec{f}$, which represents the momentum variation caused by irreversible processes. The vector $\vec{f_{vw}}$ can be computed as

follows:

$$\vec{f}_{vw} = -\rho \Delta \bar{u} \vec{q} \tag{4.9}$$

Consequently, the irreversible drag $\mathrm{D_{irr}}$ can be expressed as follows:

$$\mathrm{D_{irr}} = \int_{S_\infty \cup S_A} \left(\vec{f}_{vw} \cdot \vec{n} \right) dS \tag{4.10}$$

Using Ostrogradsky's theorem, we can transform this surface integral into a volumetric one, as follows:

$$\mathrm{D_{irr}} = \int_V \left(\vec{\nabla} \cdot \vec{f}_{vw} \right) dV \tag{4.11}$$

In a region where the flow is isentropic, the axial velocity defect $\Delta \bar{u}$ and the value of the integral in Eq. (4.11) diminish to zero. This means that the integral in Eq. (4.11) may be limited to shock volume V_W and to viscous volume V_V, and so the viscous drag and wave drag are obtained as follows:

$$\mathrm{D_V} = \int_{V_V} \left(\vec{\nabla} \cdot \vec{f}_{vw} \right) dV \tag{4.12}$$

$$\mathrm{D_W} = \int_{V_W} \left(\vec{\nabla} \cdot \vec{f}_{vw} \right) dV \tag{4.13}$$

In order to automate volume selection, sensors are used. For the viscous volume V_V, Tognaccini [50] proposes the following relation:

$$F_V = \frac{\mu_l + \mu_t}{\mu_l} \tag{4.14}$$

Equation (4.14) is calculated for each cell, and, if its value is greater than 1.1 times its free stream value, then the cell is attributed to the viscous volume.

For the shock volume V_W, the following relation has been proposed by Lovely et al. [15] :

$$F_W = \frac{\vec{V} \cdot \nabla p}{a |\nabla p|} \tag{4.15}$$

Again, Eq. (4.15) is evaluated at each cell, and, if its value is greater than 1, the cell is attributed to the shock volume V_W.

Spurious drag is obtained by evaluating Eq. (4.11) in volumes where the flow is expected to be isentropic, i.e. $V_{SP} = V/(V_V \cup V_W)$. Spurious drag can be expressed as follows:

$$\mathrm{D_{SP}} = \int_{V/(V_V \cup V_W)} \left(\vec{\nabla} \cdot \vec{f_{vw}}\right) dV \tag{4.16}$$

Spurious drag is caused by artificial dissipation that is implemented in flow solvers to enhance convergence and stability. However, it pollutes the numerical results, which is why the ability to quantify it and remove it is one of the key advantages of the far-field method.

The second part of $\vec{f}$, $\vec{f_i}$, which is associated with momentum variations caused by reversible processes, is expressed as follows:

$$\vec{f_i} = \vec{f} - \vec{f_{vw}} = -\rho(u - u_\infty - \Delta\bar{u})\vec{q} - (p - p_\infty)\vec{i} + \vec{\tau}_x \tag{4.17}$$

With this equation, the reversible drag, that is, the induced drag, can be evaluated as follows:

$$\mathrm{D_I} = \int_{V_V + V_W + V_{Sp}} \left(\vec{\nabla} \cdot \vec{f_i}\right) dV - \int_{S_A} \left(\vec{f_i} \cdot \vec{n}\right) dS \tag{4.18}$$

However, vortices rapidly dissipate in the wake because cells grow very quickly in this area. To overcome this issue, Laurendeau et al. [20] propose to limit the integration volume for the induced drag near the configuration. In this paper, the volume is composed of all the cells within a distance from a wall of less than 2 chords.

Numerical implementation

As proposed by Tognaccini [50], Ostrogradsky's theorem can be used to transform volumetric integrals of Eqs. (4.12),(4.13), (4.16), and (4.18) into surfacic integrals applied to all the cells contained in the volume. For example, wave drag can be expressed as follows:

$$\mathrm{D_W} = \sum_{i=1}^{N} \sum_{j=1}^{M} \left[A \left(\vec{f_{vw}} \cdot \vec{n}\right)\right]_{i,j} \tag{4.19}$$

where the indices i, j represent the j^{th} face of the i^{th} cell, and A is the face area.

With this far-field method, it is then possible to post-treat a CFD solution and decompose the physical drag into its components, i.e. wave, viscous, induced, and spurious drag. Some examples of the application of the method to non-motorized configurations are given in Refs. [20–22, 29, 34, 51].

4.3.2 Internal, external, upstream, and wake volumes

In the last section, we presented the theory behind the far-field method, mainly as developed by Destarac [25] and Gariepy et al. [34, 52]. With this method, drag can be decomposed into its viscous, wave, and induced drag components. Based on this far-field method, the DQEID method is aimed at using the same decomposition method to separate internal drag from external drag. For a typical nacelle configuration, the computational domain can be decomposed into four parts, the upstream, external, internal, and wake regions, as shown in Fig. 4.2. First, the total drag is decomposed into two parts: induced drag, and irreversible drag. Then, the irreversible drag is decomposed on each of these volumes into viscous, wave, and spurious drag. As the objective of this work is to separate external from internal drag, the question then becomes, how do we handle upstream drag and wake drag? Owing to the lack of drag production in the upstream area, the computed drag in this region is reckoned to be solely spurious drag, and should be removed from the final solution. However, wake drag is not solely caused by spurious drag, and needs to be added to either the internal drag or the external drag, or both. We will argue later that the wake drag is mainly caused by the flow through the nacelle, which results in its addition to the internal drag. Fig. 4.3 presents a summary of the proposed drag decomposition process.

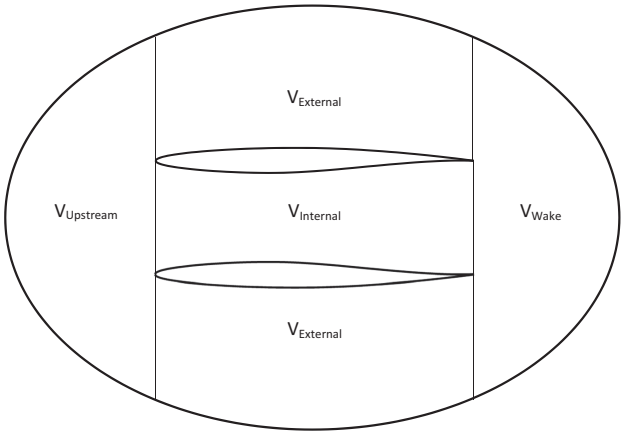

Figure 4.2 Integration volumes

4.4 Validation of internal drag computations on 2D geometries

As explained earlier, installation drag can be computed using Eq. (4.1). Clearly, the internal drag must be known. Aerodynamicists typically compute the internal drag either experimentally [2–4, 42], empirically [53, 54], or by CFD analysis, in order to compute the installation drag. Using CFD analysis, internal drag can be computed as follows:

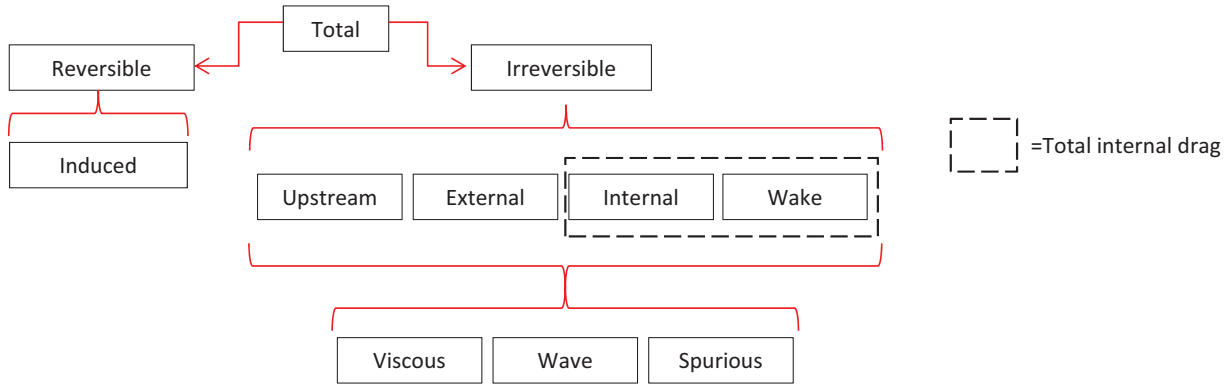

Figure 4.3 Drag decomposition inside volumes (note that the spurious drag is subtracted from the final solution)

$$C_d^{\text{Internal}} = \int_{S_{\text{Internal}}} \left(\vec{f} \cdot \vec{n}\right) dS \tag{4.20}$$

Determining the interior surface of the nacelle S_{Internal} usually requires locating the stagnation line, which separates internal from external flows. Doing so accurately is of particular importance, because the pressure is very high in this region and any location error would yield inconsistent results. This pressure sensitivity may be associated with the presence of strong pressure gradients at the nacelle's leading edge. The impact of such a sensitivity is illustrated below.

One way to reduce this sensitivity would be to apply an approach based on the far-field methodology. As stated earlier, our hypothesis is that the DQEID method would be less sensitive to the location of the stagnation point, because it is based on entropy production, which is very small close to that point – see Eqs. (4.5) and (4.9).

To verify this hypothesis, 2D simulations were performed. Since a 2D nacelle can be seen as a mirror profile, it follows that both the near-field and DQEID methods could be applied on a single profile for validation purposes. In this way, the pressure side drag and the suction side drag of the profile can be computed like the internal drag and external drag of a nacelle respectively. For this validation, two profiles were selected: NACA0012, because of its symmetry, and RAE2822.

Point A on Fig. 4.4 represents the stagnation point which, for the NACA0012, corresponds to the airfoil's forward-most point. For the RAE2822, it corresponds to the airfoil face with the highest pressure.

For the near-field internal drag, Eq. (4.20) is computed from point A to the trailing edge on the pressure side while, for the DQEID method, Eq. (4.11) is evaluated on the internal volume located below the horizontal line extrapolated from point A as shown in Fig. 4.4. Note that there is no irreversible drag generated upstream of the vertical line. To test the sensitivity of the stagnation point's location, four other computations are performed as the stagnation point, and the corresponding extrapolated dividing line, are moved higher and lower than their original position, as shown as points/lines B, C, D, and E in Fig. 4.4.

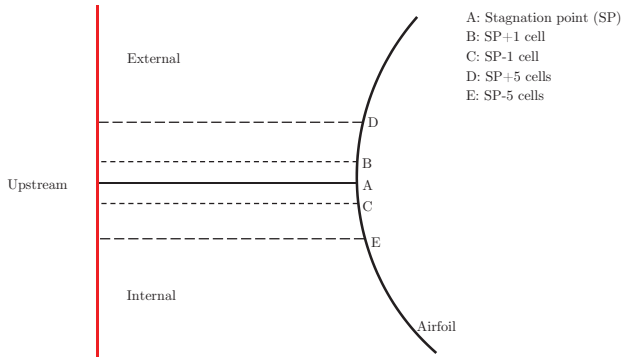

Figure 4.4 Streamlines (zoom on leading edge)

4.4.1 Flow conditions, meshes, & algorithm

The flow conditions are listed in Table 4.1. The meshes and a zoomed-in view at the stagnation point are shown in Fig. 4.5 and 4.6 respectively. The meshes contain 21600 and 52650 cells for NACA0012 and RAE2822 respectively. All the simulations were run with the ANSYS Fluent 13.0 CFD software. All the meshes were generated with ICEM-CFD, and provided values of $y+$ below 1. The Spalart-Allmaras [55] turbulence model was used, with a 4% turbulence viscosity ratio at the far-field boundaries, which were set to pressure-far-field. The density-based solver combined with the implicit Roe scheme was selected, and second order upwind resolution associated with the Green-Gauss cell center algorithm was used. For all the simulations, the residuals were dropped below 10^{-10}, and the drag coefficient was stable and non varying within less than 0.01 drag count (note that 1 drag count is worth $1/10,000^{th}$ of the drag coefficient).

4.4.2 Results

The results for NACA0012 and RAE2822 are summarized in Tables 4.2 and 4.3 respectively. In both tables, column 2 represents the distance from the stagnation point, which is A in

Table 4.1 Flow properties

Property	**Value**	**Units**
M_∞	0.60	-
α	0.00	$^\circ$
T_∞	300	K
ρ_∞	1.176674	kg/m^3
p_∞	101325	Pa
c	1.0	m
μ_∞	$3.8907 \cdot 10^{-5}$	$kg/m \cdot s$
Re_c	$6.3 \cdot 10^6$	-

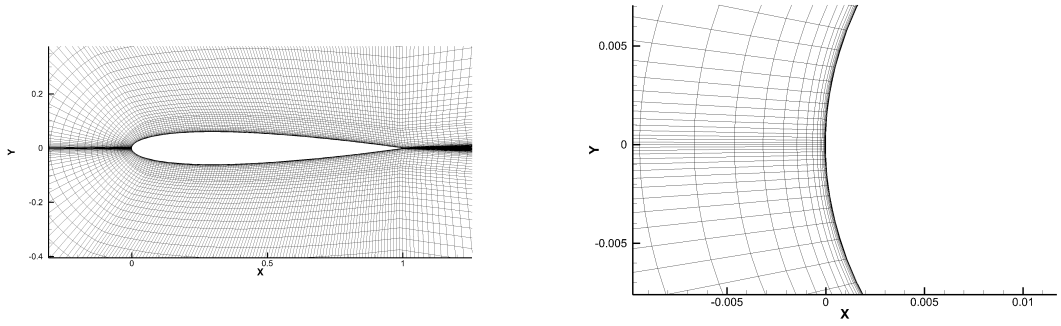

(a) Overall (b) Zoom on stagnation point

Figure 4.5 Mesh on NACA0012 airfoil

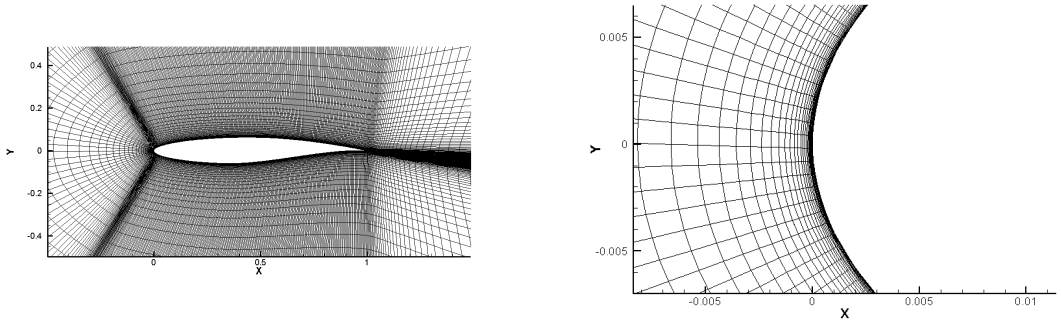

(a) Overall (b) Zoom on stagnation point

Figure 4.6 Mesh on RAE2822 airfoil

Fig. 4.4 and in Tables 4.2 and 4.3. Columns 3 and 4 represent the near-field drag coefficients computed with Eq. (4.20) for the suction and pressure sides corresponding to the external

drag and internal drag respectively. Each line represents a different location of the stagnation point. Columns 5 and 6 represent the far-field drag coefficients computed with Eq. (4.11) on the external and internal volume respectively. Columns 7 and 9 represent the absolute error between the computed drag coefficient with a particular stagnation point location and the same coefficient when evaluated at the precise location of the stagnation point with the near-field and the far-field approaches respectively. Columns 8 and 10 represent the relative error for the near-field and far-field approaches respectively. Finally, the last line of both tables shows the balance between the near-field and far-field methods.

For the NACA0012 airfoil, we expect the drag on both sides to be equal, because of its symmetry. Analysis of Table 4.2 shows that this is the case when the stagnation point is used (referred to as point A in Table 4.2). Further analysis of Table 4.2 reveals that slight variations in the stagnation point lead to inaccurate results when computed with the near-field method, showing an error of 20% in the worst case. However, with the far-field approach, the maximal error is less than 0.1%, which allows us to conclude that it is independent of the location of the stagnation point.

According to Table 4.3, RAE2822 behaves in the same way. In fact, our results for the internal drag and external drag are approximately the same with both the near-field and far-field approaches. However, as with the NACA0012 airfoil, the near-field approach results are inconsistent if there is any change in the location of the stagnation point, with an error of 79% in the worst-case scenario. For the far-field method, the maximal error is less than 0.1%.

For both cases (NACA0012 and RAE2822), analysis of the results shows that there is an imbalance between the near-field drag and the far-field drag. The magnitude of the imbalance, which amounts to 1 and 3 drag counts for NACA0012 and RAE2822 respectively, can be explained by looking at the drag decomposition summarized in Table 4.4. The difference is due to induced drag, which should theoretically be zero for 2D cases. However, this behavior is expected with pressure-far-field boundaries [56, 57].

Finally, the fact that the stagnation point could be displaced by as much as $\frac{\Delta y}{c} = 0.003$ may seem unrealistic. However, since it corresponds to the airfoil wall face associated with the highest pressure, and because the pressure is constant along this face, the accuracy of its location becomes highly dependent on mesh refinement. Furthermore, when considering a 3D nacelle, a stagnation line must be used. This line is composed of a series of stagnation points, each of which is subject to error. Clearly, the situation is more complicated in 3D cases, and this is where the robustness of the DQEID method becomes a key advantage.

Table 4.2 Comparison of the near-field and far-field suction side (SS) drag and the pressure side (PS) drag with stagnation point deviation for NACA0012 at M0.6 and 0° A.O.A. (drag counts)

Line (J)	$\frac{\Delta y}{c}$	C_d^{NF} SS	C_d^{NF} PS	C_d^{irr} SS	C_d^{irr} PS	**Near-Field** $\lvert C_{d,A} - C_{d,J} \rvert$	**Near-Field** $\frac{\lvert C_{d,A} - C_{d,J} \rvert}{C_{d,A}}$	**Far-Field** $\lvert C_{d,A} - C_{d,J} \rvert$	**Far-Field** $\frac{\lvert C_{d,A} - C_{d,J} \rvert}{C_{d,A}}$
A	0.0	43.5	43.5	43	43	-	-	-	-
B	$2 \cdot 10^{-4}$	42	45	43	43	1.5	3%	< 0.01	$< 0.1\%$
C	$-2 \cdot 10^{-4}$	45	42	43	43	1.5	3%	< 0.01	$< 0.1\%$
D	$9 \cdot 10^{-4}$	35	52	43	43	8.5	20%	< 0.01	$< 0.1\%$
E	$-9 \cdot 10^{-4}$	52	35	43	43	8.5	20%	< 0.01	$< 0.1\%$
Total		**87**		**86**					

Table 4.3 Comparison of the near-field and far-field suction side (SS) drag and the pressure side (PS) drag with a stagnation point deviation for RAE2822 at M0.6 and 0° A.O.A. (drag counts)

Line (J)	$\frac{\Delta y}{c}$	C_d^{NF} SS	C_d^{NF} PS	C_d^{irr} SS	C_d^{irr} PS	**Near-Field** $\lvert C_{d,A} - C_{d,J} \rvert$	**Near-Field** $\frac{\lvert C_{d,A} - C_{d,J} \rvert}{C_{d,A}}$	**Far-Field** $\lvert C_{d,A} - C_{d,J} \rvert$	**Far-Field** $\frac{\lvert C_{d,A} - C_{d,J} \rvert}{C_{d,A}}$
A	0.0	48	39	48	36	-	-	-	-
B	$6 \cdot 10^{-4}$	42	45	48	36	6	15%	< 0.01	$< 0.1\%$
C	$-6 \cdot 10^{-4}$	53	34	48	36	5	13%	< 0.01	$< 0.1\%$
D	$3 \cdot 10^{-3}$	19	68	48	36	29	74%	< 0.01	$< 0.1\%$
E	$-3 \cdot 10^{-3}$	79	8	48	36	31	79%	< 0.01	$< 0.1\%$
Total		**87**		**84**					

Table 4.4 Drag decomposition on the NACA0012 and RAE2822 airfoils (values in drag counts)

Drag	**Value**		**Eq. #**
	NACA0012	**RAE2822**	
Near-field	87	87	(4.2)
Far-field	87	87	(4.4)
Viscous	81	81	(4.12)
Wave	0	0	(4.13)
Spurious	5	3	(4.16)
Induced	1	3	(4.18)

Indeed, the DQEID method, being derived from the far-field theory, allows separation of the computational domain in sub-volumes. However, the real advantage of the latter is that we proved that a high level of accuracy near the nacelle's inlet is not required when delimiting the nacelle's internal volume. This last part constitutes the main contribution behind the

DQEID method.

4.5 Validation of internal drag computation on 3D geometries

In this section, we present the results computed on 3D geometries. First, the DQEID method is applied on a cylindrical nacelle. This test case was selected owing to the symmetry of the internal and external flows, which means that both the internal drag and the external drag are known, as they are equal and because there is no ambiguity in the location of the stagnation line. The second test case is based on the CFM56 TFN. For comparison purposes, owing the scarcity of experimental and CFD data on internal drag, another simulation was run on the CFM56 nacelle, but this time with a bellmouth inlet. This test case was inspired by the experiments performed at Onera [2, 58]. For this specific configuration, there is only internal drag to consider, which means that the computed internal drag coefficient can be used in the CFM56 test case with a normal inlet for comparison purposes.

In the next section, we present the grids, algorithms, and boundary conditions used in these two test cases.

4.5.1 Flow conditions, meshes, & algorithm

For the cylindrical (Fig. 4.7(a)) and CFM56 (Fig 4.8(a)) nacelles, a mesh was used with 0.2 and 2.4 million hexahedral cells respectively. The two meshes are shown in Figs. 4.7(b) (cylindrical nacelle) and 4.8(b) (CFM56 nacelle). Boundary conditions in the far-field were set to pressure-far-field in Fluent. The other conditions applied for these test cases are listed in Table 4.5 (CFM56 with bellmouth inlet) and 4.6 (cylindrical nacelle and CFM56). The length of all the nacelles is 1 m. The radius of the cylindrical nacelle is 0.15 m and the radius of the CFM56 nacelle at the forward-most point is 0.1531 m.

Table 4.5 Flow properties for the bellmouth test case

Property	**Value**	**Units**
T_0 at pressure inlet	300	K
P_0 at pressure inlet	101325	Pa
T at pressure outlet	300	K
P at pressure outlet	101325	K
S_{ref}	3.207	m^2
q_∞	39894	Pa
$\dot{m}$	16.62	kg/s

Table 4.6 Flow properties for the cylindrical and CFM56 nacelles

Property	**Value**	**Units**
M_∞	0.75	-
T_∞	300	K
ρ_∞	1.176674	kg/m^3
p_∞	101325	Pa
L_{nacelle}	1.0	m
c	0.6634	m
S_{ref}	3.207	m^2
μ_∞	$6.7652 \cdot 10^{-5}$	$kg/m \cdot s$
Re_c	$3 \cdot 10^6$	-

For a convergence study of the CFM56 nacelle with a bellmouth inlet, three meshes were used. From coarse to fine, these meshes have 0.4, 3.2, and 26.3 million cells respectively. At each refinement step, the number of nodes on each edge was doubled. A portion of the coarse mesh is shown in Fig. 4.9.

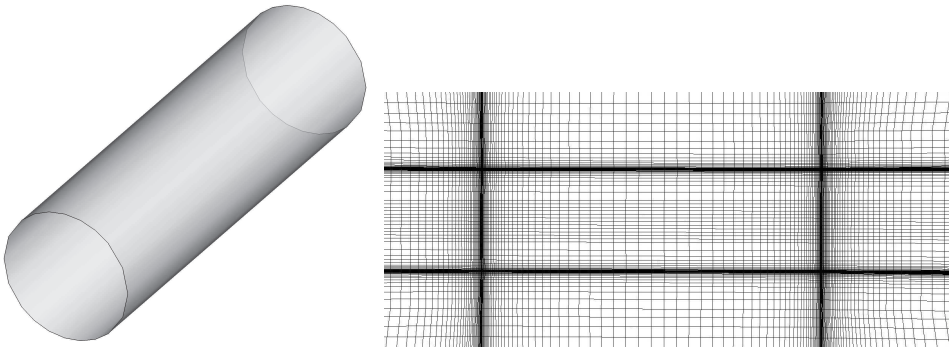

(a) Geometry (b) Mesh

Figure 4.7 Cylindrical nacelle

The solver, algorithms, and turbulence model are the same as for the 2D validation cases – see section 4.4 4.4.1 for more information. In all the simulation runs, convergence was judged on the stabilization of the drag coefficient up to a 0.01 drag count, and convergence on the residuals dropped below 10^{-5}. All the y+ values were below 1.

For the CFM56 test case with a bellmouth, the shape of the bellmouth inlet was constructed using a cubic spline. The bellmouth geometry was inspired by the experiments performed at ONERA [58] during the second drag prediction workshop. Figure 4.10(a) shows that the bellmouth connects tangentially to the inside of the nacelle. Fig. 4.10(b) shows that we reproduced this characteristic. The computational domain is shown in Fig. 4.11. Outside

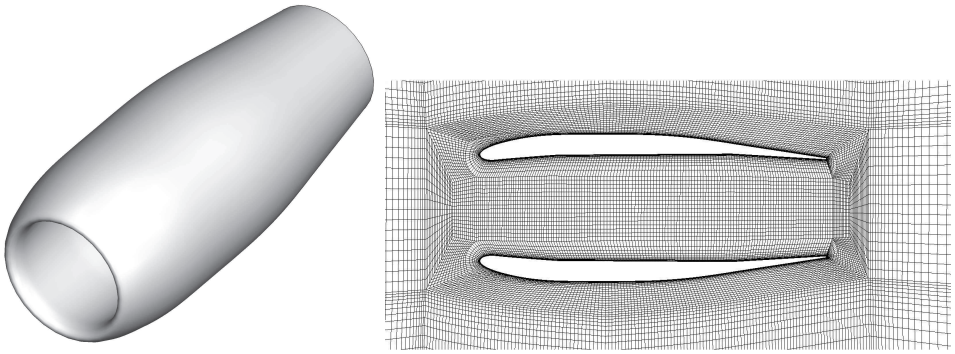

(a) Geometry (b) Mesh

Figure 4.8 CFM56 nacelle

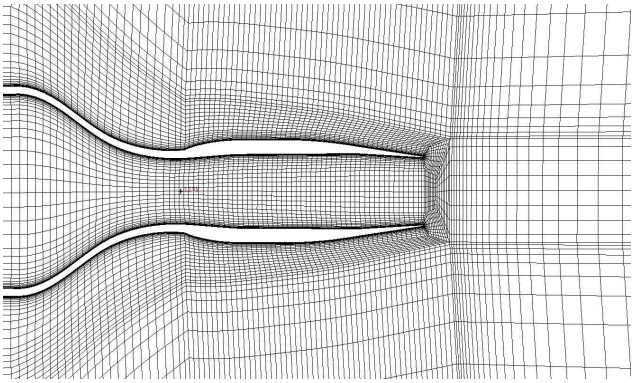

Figure 4.9 Coarse mesh on CFM56 with a bellmouth

the nacelle, in the far field, a pressure inlet at constant pressure allows the outside flow to be almost stagnant. The mass flow rate was obtained from the regular CFM56 simulation in Fluent, and imposed so that the two mass flow rates are equal.

In the next section, we present the results computed on the cylindrical nacelle.

4.5.2 Results - cylindrical nacelle

In this test case, we used a thin walled cylindrical nacelle, as illustrated in Fig. 4.7(a). Because of the thinness and straightness of these walls, there is no pressure drag, and so results can be validated with empirical techniques such as Prandtl-Schlichting's relation [59], as follows:

$$\mathrm{C_f} = \frac{0.455}{[\log Re]^{2.58}} \tag{4.21}$$

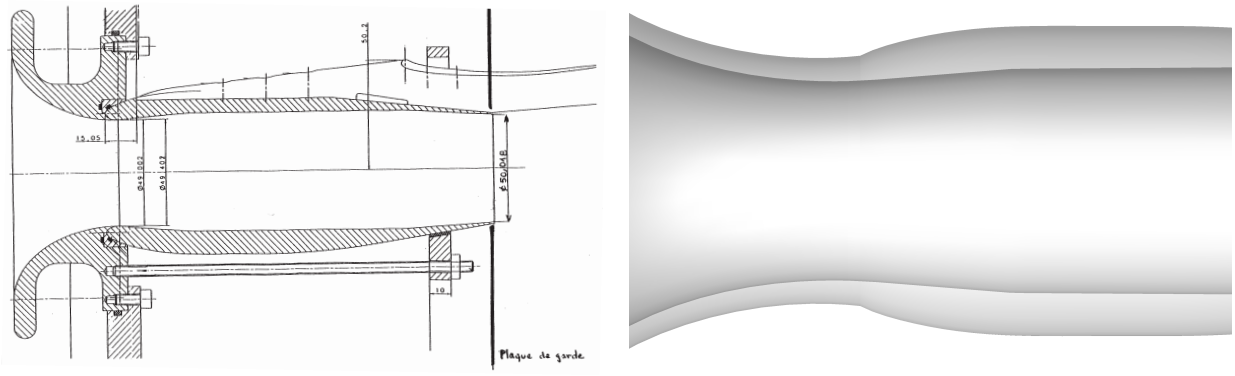

(a) Experimental configuration at ONERA [58] (b) CFD

Figure 4.10 Junction between the bellmouth and the nacelle

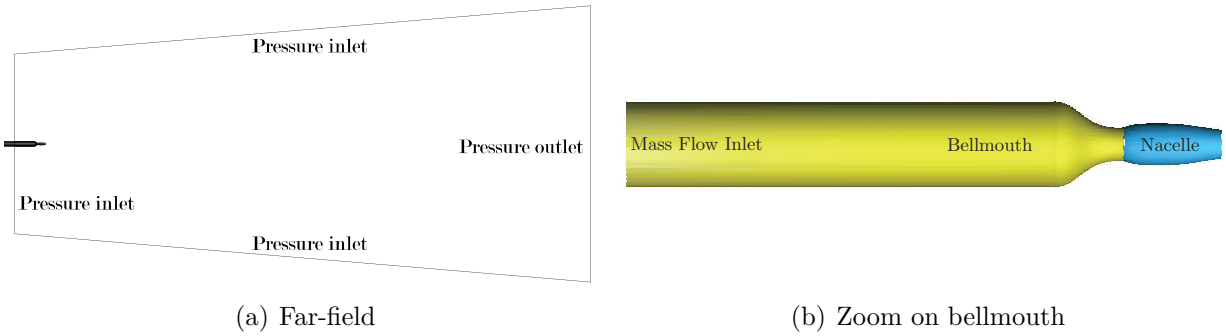

(a) Far-field (b) Zoom on bellmouth

Figure 4.11 Boundary conditions and computational domain for the bellmouth simulation

For this specific Reynolds number, the empirical value is 10.7 drag counts for both the external and the internal drag. Note that this assumes a thin boundary layer on the internal walls.

Furthermore, because of the absence of pressure drag owing to the thin, straight walls of the nacelle, there is only viscous drag, and so the flow passing through the interior of the nacelle must have the exact same characteristics of the flow outside the nacelle. We can validate this deduction by analyzing Fig. 4.12, which shows the axial velocity inside and outside the boundary layers at 90% of the nacelle length against the vertical axis. Note that the boundary layers are symmetrical.

In this particular test case, there is no induced drag, nor is there wave drag, as we can see by analyzing the overall drag decomposition presented in Table 4.7. Fig. 4.13 presents the results of the DQEID method for the viscous drag (Eq. (4.12)) and the spurious drag (Eq. (4.16)) on each of the four volumes (upstream, external, internal, and wake) presented earlier. We can see that there is no spurious drag, nor is there viscous drag in the wake, and,

because of the isentropic nature of the flow in this area, there is only spurious drag in the upstream volume. The results are compared in Table 4.8, which shows that the internal and external viscous drags are identical, as expected. Furthermore, we note that there is good agreement between the two methods. The near-field and DQEID drags are 9.1 and 8.7 drag counts respectively, corresponding to a difference of less than 0.5 drag counts or a difference of less than $5 \cdot 10^{-5}$ in the drag coefficients. Furthermore, both methods are within two drag counts of the empirical data.

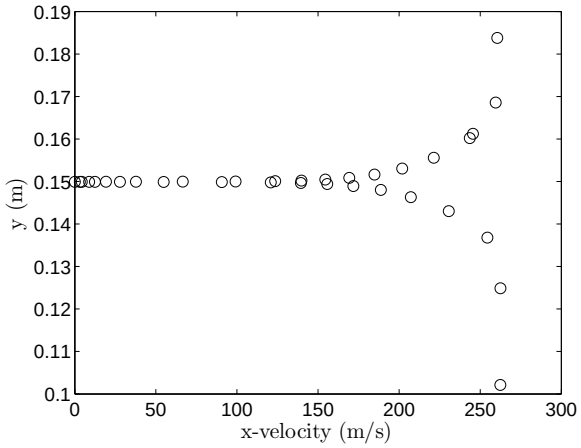

Figure 4.12 Axial velocity at 90% of the nacelle length

Table 4.7 Drag decomposition on the cylindrical nacelle (values in drag counts)

Drag	**Value**	**Eq. #**
Near-field	18.2	(4.2)
Far-field	18.2	(4.4)
Viscous	17.4	(4.12)
Wave	0.00	(4.13)
Spurious	0.9	(4.16)
Induced	0.0	(4.18)

Table 4.8 Values of internal and external drag coefficients obtained with different methods (drag counts)

Method	**Near-field**		**DQEID** (C_d^V)		**Empirical** (Eq. (4.21))
Zone	Internal	External	Internal	External	
$\mathbf{C_d}$	9.1	9.1	8.7	8.7	10.7

In the next section, we present the results computed on the CFM56 nacelle with a bellmouth inlet.

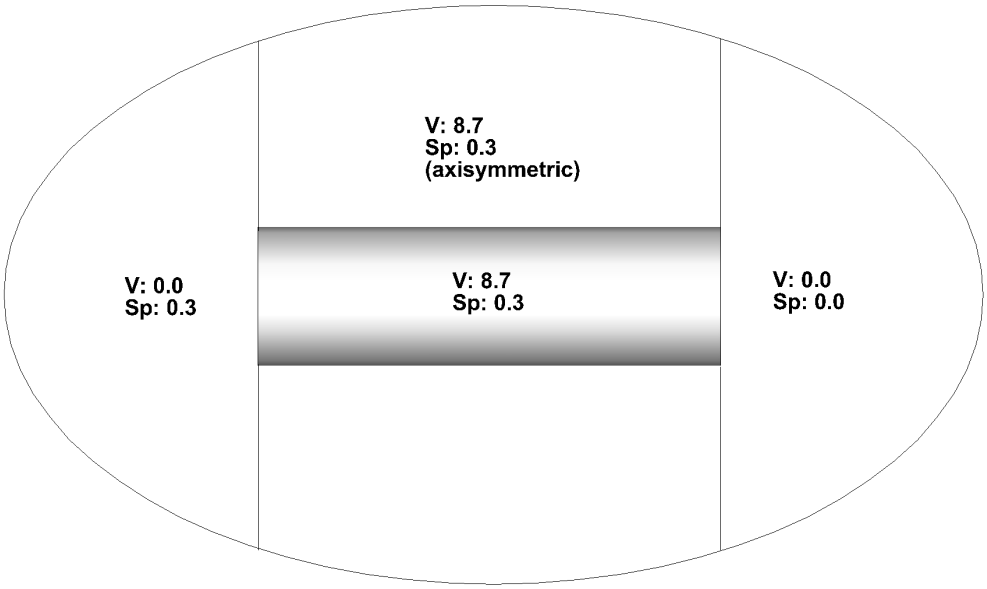

Figure 4.13 Distribution of viscous and spurious drag for different regions of the computational domain (drag counts)

4.5.3 Results - CFM56 with a bellmouth inlet

In this test, the CFM56 nacelle is connected to a bellmouth inlet. This particular configuration is illustrated in Fig. 4.11. As discussed earlier, the objective of this test case is to give a reference value for the internal drag. This can be easily achieved, since this configuration only allows inside flow, which means that the drag generated is only internal. Furthermore, all forces on this configuration are associated to internal drag as it is customary in the wind tunnel variation of this test case. Thus, it is believed that the wake drag should also be included in the internal drag. To ensure that the value of the internal drag is accurate, a refinement study was performed. Results are summarized in Table 4.9. Columns 2, 3, and 4 list the near-field drag coefficients computed on the coarse, medium, and fine mesh respectively. The 5^{th} column lists the extrapolated value computed with Celik et al.'s method [60]. The 6^{th} and 7^{th} columns list the extrapolation error and the order of convergence of the method respectively. These values, which are 4% and 1.7 respectively, lead us to conclude that the fine mesh is satisfactory for our needs. The extrapolated internal drag coefficient value (column 5) represents the drag if the mesh has been infinitely refined, and this value of 4.4 drag counts will serve as a reference for the next test case, the CFM56 TFN.

Table 4.9 Refinement study on the CFM56 with a bellmouth inlet

Mesh	Coarse	Medium	Fine	Extrapolated	Error	p
$\mathbf{C_d}$	6.0	4.9	4.5	4.4	4%	1.7

4.5.4 Results - CFM56 nacelle

The last validation test case involves the CFM56 nacelle in a viscous flow. The various boundary conditions are summarized in Table 4.6. The Mach number contours are shown in Fig. 4.14. Analysis of the latter reveals that the maximum value of the Mach number is 0.93, which is less than 1, indicating that there is no wave drag. Furthermore, because the angle of attack is zero and due to the axisymmetric geometry of the nacelle, there is no induced drag either. The overall drag decomposition is presented in Table 4.10, and confirms that neither induced drag nor wave drag is generated in this test case.

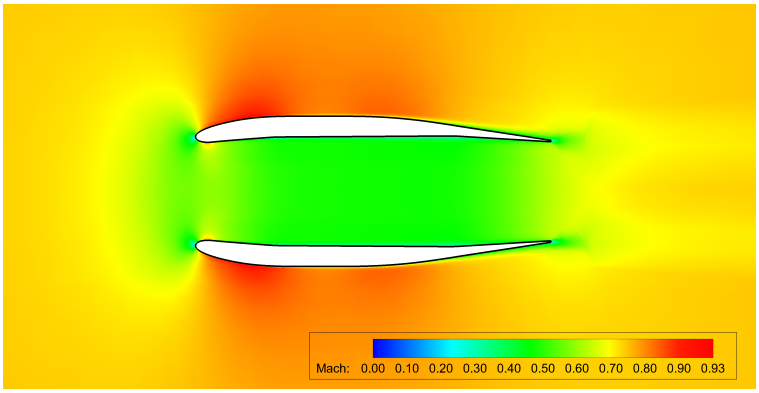

Figure 4.14 Contours of Mach numbers around the CFM56 nacelle

Table 4.10 Drag decomposition on the CFM56 nacelle (values in drag counts)

Drag	Value	Eq. #
Near-field	21.4	(4.2)
Far-field	21.1	(4.4)
Viscous	19.6	(4.12)
Wave	0.0	(4.13)
Spurious	1.5	(4.16)
Induced	0.0	(4.18)

Figure 4.15 shows drag decomposition in terms of viscous and spurious drag for the upstream, external, internal, and wake volumes. As expected, there is only negligible spurious drag in

the upstream region. The viscous drag in the internal volume is 3.6 drag counts, and 14.6 in the external volume.

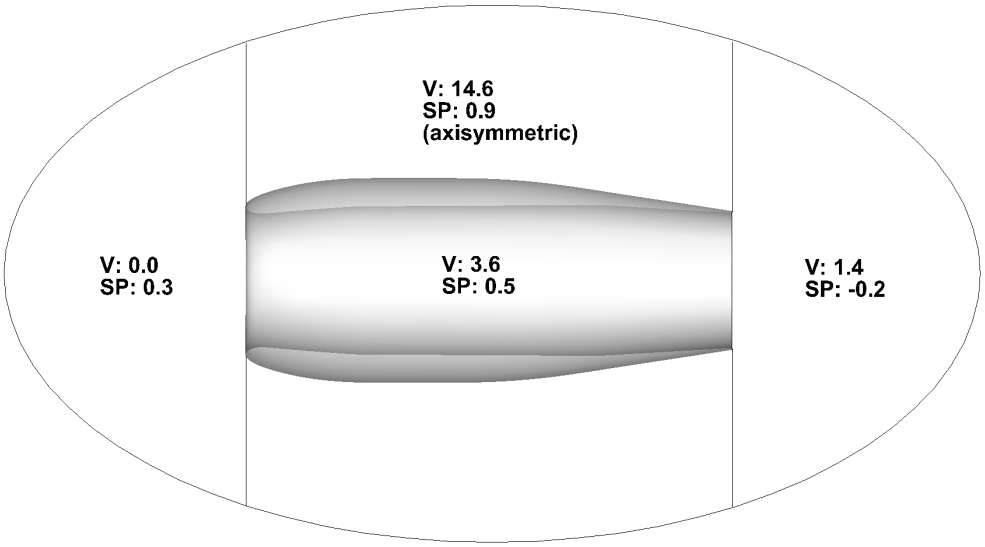

Figure 4.15 Illustration of drag decomposition on the CFM56 nacelle (drag counts)

Analysis of Fig. 4.15 reveals a value of 1.4 drag counts generated in the wake volume. As discussed earlier, the question is, how can we handle this viscous wake drag? We know that it is common practice in bookkeeping convention [3, 50] to consider viscous effects occurring in the jet as thrust loss. However, in this particular case, no thrust is generated. The wake drag is caused by the momentum change between the internal and external flow in the jet at the exit. Specifically, the flow encounters a momentum variation throughout the nacelle. This proves that the wake drag must be associated with the internal drag, as explained earlier. Indeed, it is common practice, from bookkeeping conventions, to discretize responsibilities based on the engine's captured streamtube. Everything occurring in the streamtube is the responsibility of the engine manufacturer, while the counterpart of the flow is the airframer's responsibility. Since thrust is, by definition, undoubtedly associated with the engine, and so, by stating that viscous effects in the wake are considered a thrust loss, we are implicitly implying that those effects are associated with the engine's captured streamtube. In the present case, there is no thrust. It is thus logical to add these viscous effects to the nacelle's internal drag.

Furthermore, the turbulence dissipation generates a mass entrainment between the inner and outer flow streams, which are mixed in the wake, making it impossible to determine the force

contributed by each stream individually [25]. This can be seen in Fig. 4.16, in which the entropy contours are presented. Analysis of this figure shows that the generation of drag is solely limited to the inside of the jet stream. One way to prove our assertion is to divide the wake volume into two parts, as shown in Fig. 4.17, and to compute the drag for each of these two volumes. By varying the angle defining these volumes, the boundary layer will eventually be crossed. Theoretically, the contribution to the drag by each volume will vary with the angle, until the angle is large enough to be outside the jet stream. We can verify this hypothesis by analyzing the drag distribution function of the angle of variation in Fig. 4.17. Analysis of this figure reveals that, for an angle greater than 30 degrees, the drag no longer varies, and that the contribution to the wake drag is solely caused by the drag generated inside the jet stream (the drag in the outside volume being zero). Hence, the wake drag can be added to internal drag. We can see in Fig. 4.15 that the internal drag is then 3.6 + 1.4 = 5.0 drag counts.

Both the cylindrical and CFM56 nacelles have approximately the same dimensions; however, the internal drag is 9 drag counts for the former and 5 drag counts for the latter. This is explained by the difference in the internal mass flow rates. For the cylindrical nacelle, the mass flow rate is 20.68 kg/s, and for the CFM56 it is 16.62 kg/s. A lower mass flow rate will induce a lower internal drag.

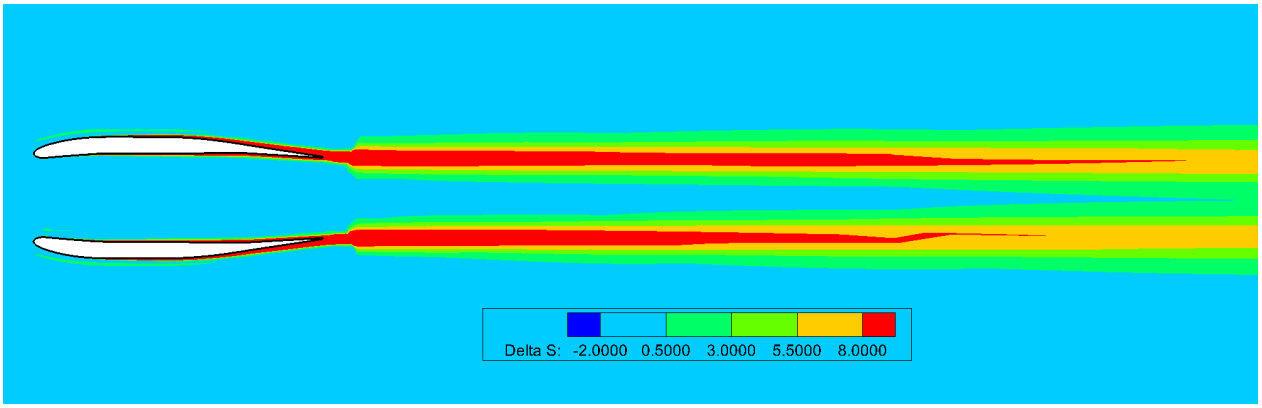

Figure 4.16 Contours of $\vec{f}_{vw}$ on the CFM56 nacelle

The drag decomposition results using various approaches are presented in Table 4.11. For the external drag, we note that there is good agreement between the empirical correlation proposed by Seddon and Goldsmith [53] (Eq. (4.22)) and the DQEID approach. The drag coefficients are 13.4 and 14.6 drag counts respectively. The difference is less than 1.5 drag counts. The difference between the empirical and DQEID calculations is less than 1% of the

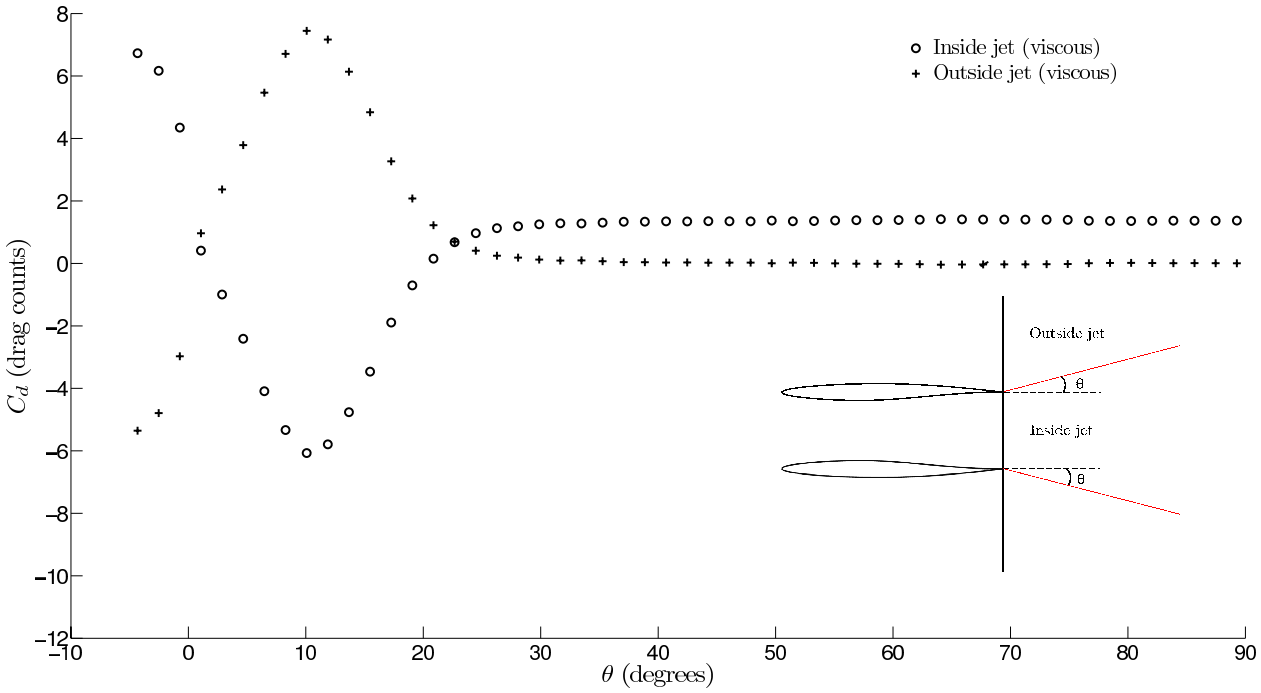

Figure 4.17 Wake drag splitting

total drag of an aircraft, which is generally around 300 drag counts.

Table 4.11 Comparison of DQEID drag to near-field, empirical, and experimental data

Zone	**Internal**			**External**	
Method	$\mathbf{C_d^{ext}}$ **(Bellmouth)**	**Experimental** [58]	**DQEID** ($\mathbf{C_d^V}$)	**Empirical**	**Far-field**
$\mathbf{C_D}$ (drag counts)	4.4	5.8	5.0	13.4	14.6

$$\left(\frac{\mathrm{C_D}}{\mathrm{C_f}}\right)^{0.6} = 1 + 0.33\frac{(d_m - d_c)}{l} \tag{4.22}$$

In the case of the internal drag, three methods are compared: near-field drag obtained from the bellmouth simulation presented in section 4.5.3, experimental data from Ref. [58], and the proposed DQEID approach. The near-field and DQEID drag coefficients are 4.4 and 5.0 drag counts respectively, which is a difference of fewer than 0.5 drag counts. There are many possible reasons for the slight difference between CFD and the experimental data, one being experimental error, an analysis of which was not available in Ref. [58].

4.6 Conclusion

This research focused on calculation of the internal drag in a nacelle. The typical near-field approach requires that the engineers separate the internal integration surface from the external one using the stagnation line. This method is very sensitive to the accuracy of this line's location, which means that this method will be inaccurate for more complex 3D geometries. We performed simple test cases on 2D geometries and we proved this last statement. To overcome the difficulty of stagnation line location, we have introduced our decomposition and quantification of external and internal drag (DQEID) method, which is derived from the well known far-field method. By dividing the computational domain into sub volumes, it is possible to isolate the domain inside the nacelle in order to evaluate the internal drag. Furthermore, because far-field drag is a function of entropy generation, its sensitivity to the location of the stagnation line is negligible. This last point constitutes the main contribution of the DQEID method. The latter has been applied to the case of a cylindrical nacelle and to the CFM56 through-flow nacelle. For validation purposes, another test case, inspired by the experimental results in the literature, has been imported into the CFD field for the first time: the CFM56 nacelle with a bellmouth inlet was simulated to isolate the internal drag. Based on bookkeeping conventions, we made the hypothesis that the wake drag belongs to the internal drag and the results proved right our hypothesis. Indeed, they show that the proposed DQEID method to compute the internal drag agrees well with experimental and empirical results, as well as with the predicted internal drag obtained from the bellmouth test case.

For all the test cases, results of the proposed DQEID method show good agreement with experimental and empirical data. Up to now, the internal drag had to be evaluated by wind-tunnel testing. The proposed approach allows a reliable and robust separation of the internal drag and the external drag from CFD simulation.

CHAPITRE 5 ARTICLE 2: Engine Pre-entry Thrust and Standard Net Thrust Evaluation Based on the Far-field Method

Malouin, B., Gariépy, M., Trépanier, J. Y., and Laurendeau, É. (2015), Engine Pre-entry Thrust and Standard Net Thrust Evaluation Based on the Far-field Method, Aerospace Science and Technology, vol. 45, pp. 50-59.

5.1 Abstract

Computation of engine pre-entry thrust is required to evaluate aircraft configuration drag. Numerical computation of this quantity requires knowledge of the captured streamtube, which depends on the stagnation line location. A new method that uses the far-field formulation is developed so that knowledge of the streamtube properties is no longer required. Using similar techniques, an alternative method to compute the standard net thrust, the basis of most thrust/drag bookkeeping systems, is introduced. The classical formulation to compute the standard net thrust needs interpolation of flow quantities in the nacelle's exit plane which leads to loss of accuracy. Theoretical development of the far-field method in power-on conditions is presented as well as an overview of the bookkeeping technique in CFD. Simulations are performed with ANSYS Fluent 13.0 on the isolated CFM56 nacelle in power-on conditions with varying boundary conditions. Results of the proposed approaches are in agreement with ESDU and classical formulations. Drag decomposition in terms of viscous, wave, spurious, induced, and through-flow drag is presented. Configuration drag is computed with two formulations which are in agreement.

5.2 Introduction

Drag extraction through near-field/far-field methods has been given attention since the last two decades so that the ultimate goal is to predict the drag coefficient within a drag count. [61]. However, motorized configurations and bookkeeping between thrust and drag are less addressed in the scientific literature. Airframers rely on both wind tunnel tests and CFD to study the interaction between the engine, the jet and the airframe. In wind tunnel tests, a through-flow nacelle (TFN) is used to evaluate the interaction drag between the wing and the engine [37]. Nonetheless, special treatment, such as truncating the nacelle, has to be made to ensure that the mass flow rate through the TFN when attached under the wing is the same as on the powered nacelle. For more accuracy, the TFN may be replaced by a Turbine Pow-

ered Simulator (TPS) [42] where compressed air is injected through a turbine to simulate jet effects. Though, there are still limitations. For instance, the jet generated by the TPS is cold.

Considering these limitations, CFD might provide a superior approach because test cases can be easily implemented. In the past, Tognaccini [50] and van der Vooren et al. [46] addressed thrust/drag bookkeeping in CFD. The former proposed a way to compute the nacelle external drag while the latter introduced the concept of additive through-flow drag created at the fan entry and turbine exit planes. In both researches, the far-field method was used. Recently, Malouin et al. [47] proposed a method to compute the internal drag of a TFN with the far-field approach.

In power-on conditions, the net propulsive force, which corresponds to the difference between the thrust and the drag, is constant for a given configuration at given flow conditions. However, many definitions for the thrust are available and the drag will vary in accordance with the thrust used in the bookkeeping system. Usually, the standard net thrust is used [1, 3] which leads to the computation of the pre-entry thrust by integrating the pressure distribution on the engine's captured streamtube. However, such procedure is not an easy task because results are dependent on the accuracy of the stagnation line location. The main objective of this paper is to propose a novel method to compute the pre-entry thrust derived from the far-field approach. Tests are performed on the CFM56 nacelle and results are compared to the ESDU [62] and to the classical pressure integration approaches. Results for the proposed method are in good agreement with both techniques. An alternative procedure to compute the standard net thrust is also presented. The classical way requires interpolation of flow quantities in the nacelle's exit plane which leads to loss of accuracy. The new formulation that uses the far-field method is shown to be more robust and less mesh-dependent.

The next section presents an overview of all the forces and drag encountered in a motorized configuration as well as a review of the far-field theory and the development of the proposed approaches to compute the pre-entry thrust and the standard net thrust. It is then followed by application on the CFM56 isolated nacelle in power-on conditions.

5.3 Theory

The difference between the configuration drag D_c and the thrust T is the net propulsive force $F = D_c - T$, which is constant at given flow conditions for a given configuration. However,

many definitions for the thrust are available and, regarding the user's choice, the thrust and the drag can vary. In the following section, forces on a motorized isolated nacelle are described. It is followed by a summary of the far-field method which is used to compute these forces. Then, new approaches to compute the standard net thrust and the pre-entry thrust are proposed.

5.3.1 Forces on configuration

Let's consider the isolated nacelle in power-on conditions depicted in Fig. 5.1. Note that the small red arrows represent the normal vectors. The forces applied to this configuration are:

- Pre-entry thrust
- Standard net thrust
- Basic thrust
- Intrinsic net thrust
- Scrubbring drag
- Nacelle external drag

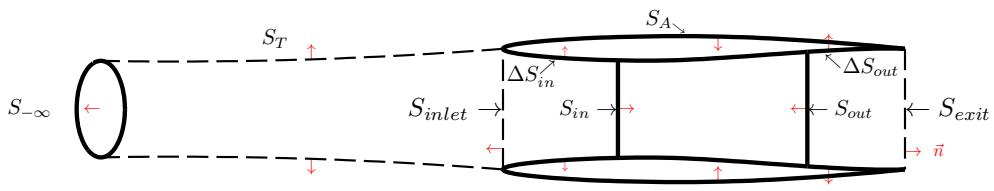

Figure 5.1 Isolated nacelle geometry and surfaces

The pre-entry thrust T_{Pre}, also known as additive drag, corresponds to the difference in stream forces between the nacelle's entry and the streamtube captation area located infinitely far upstream ($S_{-\infty}$) [62]. This force appears when the mass flow ratio is different than unit. The mass flow ratio MFR can be computed as follows:

$$\text{MFR} = \frac{S_{-\infty}}{S_{inlet}} \tag{5.1}$$

where S_{inlet} is determined by the nacelle's most forward points plane.

The pre-entry thrust is defined as follows [1, 46]:

$$\mathrm{T_{Pre}} = -\int_{S_T} \left[(p - p_\infty)\, n_x - (\vec{\tau}_x \cdot \vec{n}) \right] dS \tag{5.2}$$

where S_T corresponds to the streamtube surface. In this paper, the hypothesis is made that the shear stress is negligible on S_T because it is far from a wall and, since the streamtube is located upstream of the nacelle, it is not affected by viscous wake.

The standard net thrust $\mathrm{T_N}$ constitutes the basis of most bookkeeping systems because it uses the captation surface $S_{-\infty}$ [1]. This surface is a clever choice because the flow is undisturbed infinitely far upstream and its definition is not function of the geometry. Therefore, it is free of ambiguity. The standard net thrust is defined as follows:

$$\mathrm{T_N} = \int_{S_{-\infty} \cup S_{exit}} \left[\rho u \left(\vec{V} \cdot \vec{n} \right) + (p - p_\infty)\, n_x - (\vec{\tau}_x \cdot \vec{n}) \right] dS \tag{5.3}$$

where S_{exit} corresponds to the nacelle's exit plane as shown in Fig. 5.1.

The basic thrust $\mathrm{T_B}$, which can be considered as the force generated by the engine, is defined by:

$$\mathrm{T_B} = -\int_{S_{in} \cup S_{out}} \left[\rho \left(u - u_\infty \right) \left(\vec{V} \cdot \vec{n} \right) + (p - p_\infty)\, n_x - (\vec{\tau}_x \cdot \vec{n}) \right] dS \tag{5.4}$$

where S_{in} and S_{out} correspond to the fan inlet and turbine exit respectively, as illustrated in Fig. 5.1.

The intrinsic net thrust $\mathrm{T_{Int}}$ is given by:

$$\mathrm{T_{Int}} = \int_{S_{inlet} \cup S_{exit}} \left[\rho u \left(\vec{V} \cdot \vec{n} \right) + (p - p_\infty)\, n_x - (\vec{\tau}_x \cdot \vec{n}) \right] dS \tag{5.5}$$

The total friction and pressure drag generated on the nacelle's skin $S_{skin} = S_A \cup \Delta S_{in} \cup \Delta S_{out}$ correspond to the sum of the nacelle external drag and the scrubbing drag. The former being the drag produced by the airflow passing outside the engine while the latter corresponds to the drag generated by the inside flow on the nacelle's surfaces. The nacelle external drag D_A is defined as follows:

$$\mathrm{D_A} = \int_{S_A} \left[(p - p_\infty)\, n_x - (\vec{\tau}_x \cdot \vec{n}) \right] dS \tag{5.6}$$

where S_A represents all surfaces that are not wetted by the jet. Note that, when a full aircraft configuration is studied, $\mathrm{D_A}$ corresponds to the aircraft drag. In such a case, S_A is composed of the nacelle's external surface, the pylons, the wings, and the fuselage.

The scrubbing drag $\mathrm{D_{scrub}}$ can be computed as follows:

$$\mathrm{D_{scrub}} = \int_{\Delta S_{in} \cup \Delta S_{out}} \left[(p - p_\infty)\, n_x - (\vec{\tau}_x \cdot \vec{n}) \right] dS \tag{5.7}$$

Equations (5.2) to (5.7) are commonly known definitions. However, their evaluation in this form can lead to inaccurate results. In particular, the nacelle external drag and the scrubbing drag are sensitive to the stagnation line location. It has been shown in Ref. [47] that a small error in its determination can yield inaccurate results. To overcome this issue, alternative definitions derived from the far-field approach are proposed in the present paper for the first time to the authors' knowledge.

5.3.2 Far-field method in power-on conditions

The classical way to calculate drag is to integrate the pressure and friction forces acting on an immersed body. This is called the near-field method. Based on the principle of action-reaction, we know that the force exerted on the body by the flow is equal to the force exerted on the flow by the body, but with opposite sign. Let's consider the configuration depicted in Fig. 5.1. The near-field net propulsive force $\mathrm{F_{NF}}$ is computed as follows:

$$\mathrm{F_{NF}} = -\int_{\hat{S}_{nac}} \left(\vec{f} \cdot \vec{n} \right) dS \tag{5.8}$$

where the momentum vector $\vec{f}$ is defined by:

$$\vec{f} = -\rho(u - u_\infty)\vec{V} - (p - p_\infty)\vec{i} + \vec{\tau_x} \tag{5.9}$$

and $\hat{S}_{nac} = S_A \cup S_{in} \cup S_{out} \cup \Delta S_{in} \cup \Delta S_{out}$.

Similarly, the far-field net propulsive force $\mathrm{F_{FF}}$ can be expressed as follows:

$$\mathrm{F_{FF}} = \int\limits_{S_\infty} \left(\vec{f} \cdot \vec{n}\right) dS \tag{5.10}$$

where S_∞ is the surface of a control volume surrounding the whole configuration. It should be noted that the net propulsive force corresponds to the difference between the nacelle drag and the thrust that it generates. One way to compute the nacelle drag is to integrate the pressure and viscous forces on $S_{skin} = S_A \cup \Delta S_{in} \cup \Delta S_{out}$ as follows:

$$\mathrm{D_{NF}} = -\int\limits_{S_{skin}} \left(\vec{f} \cdot \vec{n}\right) dS \tag{5.11}$$

In order to compute the far-field drag of the nacelle, we shall introduce some variables. Drag can be caused by thermodynamic irreversible or reversible processes. The former is the consequence of shock waves and boundary layers while the latter involve exchange of mechanical energy such as wing tip vortices [12, 25]. To separate those contributions, Destarac [25] uses the axial velocity defect, $\Delta\bar{u} = \bar{u} - u_\infty$, associated with irreversible processes, as follows:

$$\Delta\bar{u} = u_\infty \sqrt{1 + 2\frac{\Delta H}{u_\infty^2} - \frac{2}{(\gamma-1)M_\infty^2}\left[\left(e^{\frac{\Delta s}{R}}\right)^{\frac{\gamma-1}{\gamma}} - 1\right]} - u_\infty \tag{5.12}$$

where entropy variation from the free stream state Δs is given by:

$$\Delta s = \frac{R}{\gamma - 1} \log\left[\frac{p}{p_\infty}\left(\frac{\rho_\infty}{\rho}\right)^\gamma\right] \tag{5.13}$$

and enthalpy variation from the free stream state ΔH is given by:

$$\Delta H = \frac{\gamma}{\gamma - 1}\left(\frac{p}{\rho} - \frac{p_\infty}{\rho_\infty}\right) + \frac{u^2 + v^2 + w^2}{2} - \frac{u_\infty^2}{2} \tag{5.14}$$

One should note that it is not possible to use Eq. (5.12) when the total pressure loss becomes significant because, in such cases, entropy decreases and the value of the square root becomes negative. To overcome this problem, Gariépy et al. [34] proposed a new formulation:

$$\Delta\bar{u} = u - u_\infty \left(\left[1 + \frac{2\Delta H}{u_\infty^2} - \frac{2}{(\gamma-1)M_\infty^2} \left[\left(\frac{p}{p_\infty} \right)^{\frac{\gamma-1}{\gamma}} - 1 \right] - \frac{v^2+w^2}{u_\infty^2} \right]^{1/2} + 1 \right) \tag{5.15}$$

This leads to $\vec{f}_{vw}$, the irreversible portion of the momentum vector $\vec{f}$, which represents the momentum variation caused by irreversible processes. The vector $\vec{f}_{vw}$ can be computed as follows:

$$\vec{f}_{vw} = -\rho\Delta\bar{u}\vec{V} \tag{5.16}$$

Consequently, the irreversible drag $\mathrm{D_{irr}}$ can be expressed by:

$$\mathrm{D_{irr}} = \int\limits_{S_\infty \cup \hat{S}_{nac}} \left(\vec{f}_{vw} \cdot \vec{n} \right) dS \tag{5.17}$$

Using Ostrogradsky's theorem, we can transform this surface integral into a volumetric one, as follows:

$$\mathrm{D_{irr}} = \int\limits_{V} \left(\vec{\nabla} \cdot \vec{f}_{vw} \right) dV \tag{5.18}$$

where V is the volume delimited by S_∞.

In a region where the flow is expected to be isentropic, the axial velocity defect $\Delta\bar{u}$ and the value of the integral in Eq. (5.18) vanish. This means that the integral in Eq. (5.18) may be limited to shock volume V_W and to viscous volume V_V, and so the viscous drag and wave drag are obtained as follows:

$$\mathrm{D_v} = \int\limits_{V_V} \left(\vec{\nabla} \cdot \vec{f}_{vw} \right) dV \tag{5.19}$$

$$\mathrm{D_w} = \int\limits_{V_W} \left(\vec{\nabla} \cdot \vec{f}_{vw} \right) dV \tag{5.20}$$

In order to automate the volume selection, sensors are used [50]. The viscous volume is given

by:

$$V_V = \left\{ (x,y,z) \in \mathbb{R}^3 : \frac{\mu_l + \mu_t}{\mu_l} \geq 1.1 \left(\frac{\mu_l + \mu_t}{\mu_l} \right)_\infty \right\} \tag{5.21}$$

The shock volume V_W is given by Ref. [15]:

$$V_W = \left\{ (x,y,z) \in \mathbb{R}^3 : \frac{\vec{V} \cdot \nabla p}{a|\nabla p|} \geq 1 \right\} \tag{5.22}$$

Spurious drag is obtained by evaluating Eq. (5.18) in volumes where the flow is expected to be isentropic, i.e. $V_{sp} = V/(V_V \cup V_W)$. Spurious drag can be expressed as follows:

$$\mathrm{D_{sp}} = \int\limits_{V_{sp}} \left(\vec{\nabla} \cdot \vec{f_{vw}} \right) dV \tag{5.23}$$

Spurious drag is caused by artificial dissipation that is implemented in flow solvers to enhance convergence and stability. However, it pollutes the numerical results, which is why the ability to quantify it and remove it is one of the key advantages of the far-field method.

The second part of $\vec{f}$, $\vec{f_i}$, which is associated with momentum variations caused by reversible processes, is expressed as follows:

$$\vec{f_i} = \vec{f} - \vec{f_{vw}} = -\rho(u - u_\infty - \Delta\bar{u})\vec{V} - (p - p_\infty)\vec{i} + \vec{\tau}_x \tag{5.24}$$

However, in motorized configuration, the engine faces (S_{in} and S_{out}) can contribute to the reversible drag. Van der Vooren and Destarac [46] introduced a new definition, the additive through-flow drag, which can be computed as follows:

$$\mathrm{D_{tf}} = -\int\limits_{S_{in} \cup S_{out}} \left(\vec{f_i} \cdot \vec{n} \right) dS + \int\limits_{S_{in} \cup S_{out}} \frac{\rho}{2} \left(v^2 + w^2 \right) n_x dS \tag{5.25}$$

The latter equation represents the crossflow kinetic energy generated by the engines. In Eq. (5.33), the reversible drag $\mathrm{D_i}$ can be evaluated as follows:

$$\begin{aligned} \mathrm{D_i} = & \int\limits_{V_V \cup V_W \cup V_{sp}} \left(\vec{\nabla} \cdot \vec{f_i} \right) dV - \int\limits_{S_{skin} \cup S_{in} \cup S_{out}} \left(\vec{f_i} \cdot \vec{n} \right) dS \\ & + \int\limits_{S_{in} \cup S_{out}} \frac{\rho}{2} \left(v^2 + w^2 \right) n_x dS \end{aligned} \tag{5.26}$$

Thus, the exact near-field/far-field drag balance becomes:

$$(\mathrm{D_p} + \mathrm{D_f})_{S_{skin}} = \mathrm{D_v} + \mathrm{D_w} + \mathrm{D_{sp}} + \mathrm{D_i} - \mathrm{D_{tf}} \tag{5.27}$$

where $\mathrm{D_p}$ and $\mathrm{D_f}$ are the pressure and friction drag respectively. From this equation, we notice that the sum of friction plus pressure drag is equal to the sum of the irreversible drag, composed of the viscous, wave and spurious drags, and reversible drag, composed of the induced drag and through-flow drag.

Note on numerical implementation As proposed by Tognaccini [16], Ostrogradsky's theorem can be used to transform volumetric integrals of Eqs. (5.19), (5.20), (5.23), and (5.26) into surface integrals applied to all the cells contained in the volume. For example, wave drag can be expressed as follows:

$$\mathrm{D_w} = \sum_{i=1}^{N} \sum_{j=1}^{M} \left[A \left(\vec{f}_{vw} \cdot \vec{n} \right) \right]_{i,j} \tag{5.28}$$

where the indices i, j represent the j^{th} face of the i^{th} cell, and A is the face area. Note that M is the number of faces by cell and N is the number of cells in the wave volume.

With this far-field method, it is then possible to post-treat a CFD solution and decompose the physical drag into its components, i.e. wave, viscous, induced, and spurious drag. Some examples of the method applied to non-motorized configurations are given in Refs. [20–22,29,34,51].

Another advantage of the far-field method that is relevant to our application is its ability to compute drag in subvolumes. For example, it is possible to compute drag in the nacelle's internal volume as described in Ref. [47]. In the following lines, a review of the thrust/drag bookkeeping technique is presented.

5.3.3 Thrust/Drag Bookkeeping

It is common practice that engine and airframe manufacturers distinguish performance of their systems by separating phenomena occuring inside or outside the streamtube. To this end, the configuration drag cannot be computed using Eq. (5.11) because contributions of inside and outside flows must be separated. Since the net propulsive force F is invariant at given flow conditions for a given configuration, the configuration drag $\mathrm{D_c}$, which corresponds to the difference between the net propulsive force and the thrust, is dependent on the thrust

definition used: basic, standard net or intrinsic. To illustrate this last statement, it is possible to express the net propulsive force as function of the different thrust definitions as shown in Table 5.1 [1,50]. Corresponding values of the configuration drag are also presented, with the basic thrust, the standard net thrust, the intrinsic net thrust, the pre-entry thrust, and the scrubbing drag defined in Eqs. (5.2) to (5.7).

Table 5.1 Various relations for the net propulsive force

When $\mathbf{F}$ is defined as	$\mathbf{D_c}$ is equal to
$(D_p + D_f)_{S_{skin}} - T_B$	$(D_p + D_f)_{S_{skin}}$
$(D_p + D_f)_{S_{skin}} - (T_{Int} + D_{scrub})$	$(D_p + D_f)_{S_{skin}} - D_{scrub}$
$(D_p + D_f)_{S_A} - T_{Int}$	$(D_p + D_f)_{S_A}$
$(D_p + D_f)_{S_A} - (T_N - T_{Pre})$	$(D_p + D_f)_{S_A} + T_{Pre}$

As stated earlier, the standard net thrust is usually used in bookkeeping systems. Thus, the difference between the near-field net propulsive force F_{NF} and the standard net thrust T_N yields the configuration drag D_c as follows:

$$D_c = F_{NF} + T_N \tag{5.29}$$

Note that a negative value of the net propulsive force means a thrust. From the last line of Table 5.1, the configuration drag can be computed as follows:

$$D_c = (D_p + D_f)_{S_A} + T_{Pre} \tag{5.30}$$

From the far-field method, it is possible to substitute the pressure and friction drag by the wave, viscous, spurious, through-flow, and induced drags:

$$D_c = D_v + D_w + D_{sp} + D_i - D_{tf} - D_{scrub} + T_{Pre} \tag{5.31}$$

However, in order to ensure an exact near-field/far-field net propulsive force balance, it is possible to use and alternative formulation for the additive through-flow drag D^*_{tf}. By combining Eq.(5.27) with the first line of Table 5.1, we get:

$$F_{NF} = D_v + D_w + D_{sp} + D_i - D_{tf} - T_B \tag{5.32}$$

By isolating D_{tf}, we get D^*_{tf}:

$$D^*_{tf} = D_v + D_w + D_{sp} + D_i - F_{NF} - T_B \tag{5.33}$$

Thus, by substituting D_{tf} by D^*_{tf} the exact near-field/far-field balance is guaranteed.

As shown in Ref. [47], it is also possible to separate the computational domain in subvolumes based on the geometry. For instance, all cells inside the nacelle can constitute a subvolume on which it is possible to compute the drag. In this case, it corresponds to the scrubbing drag. The surface integral of Eq. (5.7) is replaced by a volumetric integration of the irreversible momentum vector as follows [47]:

$$D_{scrub} = \int_{V_{int}} \left(\vec{\nabla} \cdot \vec{f}_{vw}\right) dV \tag{5.34}$$

where $V_{int} = V_{int,\ up} \cup V_{int,\ down}$ is the nacelle's internal volume as depicted in Fig. 5.2. Note that the hypothesis is made that the scrubbing drag is only constituted of irreversible phenomena. The reversible drag is thus a sole value for the whole configuration. It is not discretized in subvolumes. The reader can consult Ref. [46] for the thorough theoritical development of the power-on theory.

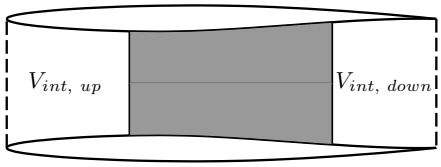

Figure 5.2 Nacelle's internal volumes

From Eq. (5.31), we know that the pre-entry thrust is required in order to compute the configuration drag which is the quantity of interest. However, to compute the latter, the pressure must be integrated on the streamtube. Such a procedure, especially for tridimensional flow, can be a delicate task. In fact, since the pressure is very high near the stagnation line, any error will generate incoherent results [47]. The need for an alternative method to compute the pre-entry thrust therefore arises. Also, from Eq. (5.29) we notice that the standard net thrust is mandatory. However, computation of this quantity through Eq. (5.3) requires interpolation of flow variables in the nacelle's exit plane. Such a procedure is expected to generate interpolation errors. Therefore, an alternative technique would be useful. Indeed,

the configuration drag can be computed using either Eq. (5.29) or Eq. (5.31), which uses the standard net thrust and the pre-entry thrust respectively. The next section presents the proposed methods to evaluate these two quantities.

5.3.4 Proposed method

From the momentum conservation in the x-direction applied to the control surfaces CS of a closed control volume, we have:

$$\int_{CS} \left(\vec{f_x} \cdot \vec{n}\right) dS = 0 \tag{5.35}$$

where the vector $\vec{f_x}$ is defined as follows:

$$\vec{f_x} = \rho u \vec{V} + (p - p_\infty)\,\vec{i} - \vec{\tau}_x \tag{5.36}$$

This principle is applied to the nacelle to obtain relations for the pre-entry thrust and the standard net thrust.

Firstly, let's consider the pre-entry thrust. The control volume is highlighted in bold lines in Fig. 5.3. Usage of S_{in} instead of S_{inlet} constitutes a great advantage. The former surface is clearly defined and, because it is a boundary, it matches grid lines. Therefore, interpolation is not required. This is not the case with S_{inlet}. Furthermore, S_{inlet} is located in a region where the pressure gradients are very high. Thus, any error in the stagnation line location would yield incoherent results. By summing all surfaces, we have:

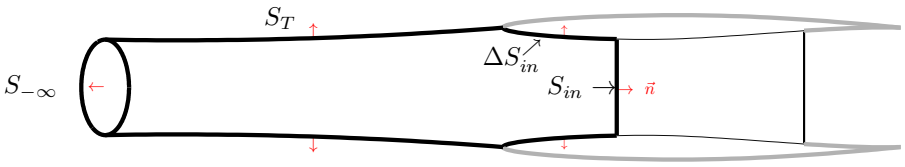

Figure 5.3 Control volume for the pre-entry thrust

$$\int_{S_{-\infty}} \left(\vec{f_x} \cdot \vec{n}\right) dS + \int_{S_T} \left(\vec{f_x} \cdot \vec{n}\right) dS + \int_{S_{in}} \left(\vec{f_x} \cdot \vec{n}\right) dS + \int_{\Delta S_{in}} \left(\vec{f_x} \cdot \vec{n}\right) dS = 0 \tag{5.37}$$

The pre-entry thrust corresponds to the negative of the second term of Eq. (5.37). By isolating this term, we get:

$$\mathrm{T_{Pre}} = \int\limits_{S_{-\infty}} \left(\vec{f}_x \cdot \vec{n}\right) dS + \int\limits_{S_{in}} \left(\vec{f}_x \cdot \vec{n}\right) dS + \int\limits_{\Delta S_{in}} \left(\vec{f}_x \cdot \vec{n}\right) dS \tag{5.38}$$

To avoid the aforementioned difficulty regarding the strong pressure gradients, it is possible to replace the last term of Eq. (5.38) by its far-field counterpart as follows:

$$\int\limits_{\Delta S_{in}} \left(\vec{f}_x \cdot \vec{n}\right) dS = \int\limits_{V_{int,\ up}} \left(\vec{\nabla} \cdot \vec{f}_{vw}\right) dV \tag{5.39}$$

where $V_{int,\ up}$ is the volume delimited by S_{in}, ΔS_{in}, and the entry plane of the nacelle.

Finally, the proposed method to compute the pre-entry thrust is given by:

$$\mathrm{T_{Pre}^{new}} = \int\limits_{S_{-\infty} \cup S_{in}} \left(\vec{f}_x \cdot \vec{n}\right) dS + \int\limits_{V_{int,\ up}} \left(\vec{\nabla} \cdot \vec{f}_{vw}\right) dV \tag{5.40}$$

The configuration drag can be computed using Eq. (5.29) which requires evaluation of the standard net thrust. In this case, we have to integrate $\vec{f}_x$ in the nacelle's exit plane S_{exit}. Usually, the issue with the rear stagnation line does not arise due to the trailing edge sharpness. Nevertheless, interpolation of the flow quantities will generate some errors because this plane does not necessarily match with grid lines. Thus, we propose an alternative method to compute the standard net thrust. Basically, the same procedure described above is applied in the case of the standard net thrust. The control volume is highlighted in bold lines in Fig. 5.4. In this case, we have two control volumes. The conservation of momentum can be applied to both of them:

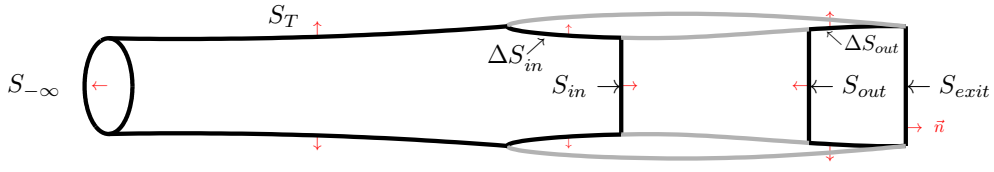

Figure 5.4 Control volume for the standard net thrust

$$\int\limits_{S_{-\infty}} \left(\vec{f}_x \cdot \vec{n}\right) dS + \int\limits_{S_{in}} \left(\vec{f}_x \cdot \vec{n}\right) dS + \int\limits_{\Delta S_{in}} \left(\vec{f}_x \cdot \vec{n}\right) dS + \int\limits_{S_T} \left(\vec{f}_x \cdot \vec{n}\right) dS = 0 \tag{5.41}$$

for the first control volume and:

$$\int\limits_{S_{out}} \left(\vec{f_x} \cdot \vec{n}\right) dS + \int\limits_{\Delta S_{out}} \left(\vec{f_x} \cdot \vec{n}\right) dS + \int\limits_{S_{exit}} \left(\vec{f_x} \cdot \vec{n}\right) dS = 0 \tag{5.42}$$

for the second one. Since the sum for both control volumes is zero, it is possible to combine them:

$$\begin{aligned} \int\limits_{S_{-\infty}} \left(\vec{f_x} \cdot \vec{n}\right) dS + \int\limits_{S_{in}} \left(\vec{f_x} \cdot \vec{n}\right) dS + \int\limits_{\Delta S_{in}} \left(\vec{f_x} \cdot \vec{n}\right) dS + \int\limits_{S_T} \left(\vec{f_x} \cdot \vec{n}\right) dS + \\ \int\limits_{S_{out}} \left(\vec{f_x} \cdot \vec{n}\right) dS + \int\limits_{\Delta S_{out}} \left(\vec{f_x} \cdot \vec{n}\right) dS + \int\limits_{S_{exit}} \left(\vec{f_x} \cdot \vec{n}\right) dS = 0 \end{aligned} \tag{5.43}$$

The definition of the standard net thrust is given in Eq. (5.3). By isolating terms present in Eq. (5.3), we get:

$$\mathrm{T_N} = -\int\limits_{S_T} \left(\vec{f_x} \cdot \vec{n}\right) dS - \int\limits_{S_{in} \cup S_{out}} \left(\vec{f_x} \cdot \vec{n}\right) dS - \int\limits_{\Delta S_{out} \cup \Delta S_{in}} \left(\vec{f_x} \cdot \vec{n}\right) dS \tag{5.44}$$

However, evaluation of Eq. (5.44) still requires the evaluation of the pre-entry thrust by integrating pressure on the streamtube. It is possible to substitute the pre-entry thrust, which corresponds to the first right-hand side term of Eq. (5.44), by Eq. (5.38). This would yield:

$$\mathrm{T_N} = \int\limits_{S_{-\infty}} \left(\vec{f_x} \cdot \vec{n}\right) dS - \int\limits_{S_{out}} \left(\vec{f_x} \cdot \vec{n}\right) dS - \int\limits_{\Delta S_{out}} \left(\vec{f_x} \cdot \vec{n}\right) dS \tag{5.45}$$

Once again, it is possible to replace the last term of the previous equation by its far-field counterpart. In this case, we get the proposed method to compute the standard net thrust:

$$\mathrm{T_N^{new}} = \int\limits_{S_{-\infty}} \left(\vec{f_x} \cdot \vec{n}\right) dS - \int\limits_{S_{out}} \left(\vec{f_x} \cdot \vec{n}\right) dS - \int\limits_{V_{int,\ down}} \left(\vec{\nabla} \cdot \vec{f}_{vw}\right) dV \tag{5.46}$$

where $V_{int,\ down}$ is the volume delimited by S_{exit}, ΔS_{out} and S_{out}. However, S_{exit} does not necessarily match a grid line. The decision to include a cell in $V_{int,\ down}$ is based upon its center. If the cell center is located upstream of S_{exit} it is thus included in $V_{int,\ down}$. So, the real dividing line may not be a straight line like S_{exit} but is more likely to have a discrete shape. Furthermore, because drag is function of small variations of entropy, the influence of

the exclusion or inclusion of a given cell is insignificant.

5.4 Test cases

5.4.1 Flow conditions, meshes, & algorithm

The CFM56 axisymmetric nacelle is used for all test cases [37, 58]. The flow conditions are listed in Table 5.2. The mesh of 2 388 480 cells, generated with ICEM-CFD, and providing values of $y+$ below 1, is shown in Fig. 5.6. All the simulations were run with ANSYS Fluent 13.0 CFD software. The Spalart-Allmaras [55] turbulence model was used, with a 4% turbulence viscosity ratio at the far-field boundaries, which were set to pressure-far-field. The density-based solver combined with the implicit Roe scheme was selected, and second order upwind resolution associated with the Green-Gauss cell center algorithm was used. For all the simulations, the residuals were dropped below 10^{-8}, and the drag coefficients were stable within less than 0.01 drag count between two successive iterations.[1].

Table 5.2 Flow properties

Property	**Value**	**Units**
α	0.00	$^\circ$
T_∞	300	K
ρ_∞	1.176674	kg/m^3
p_∞	101325	Pa
c	1.0	m
S_{ref}	3.207	m^2
μ	$6.7652 \cdot 10^{-5}$	$kg/m \cdot s$

Boundary conditions at the nacelle's entry and exit are illustrated in Fig. 5.5 and corresponding values for the nine test cases performed are listed in Table 5.3. For the engine boundary conditions, we make the hypothesis that the mass flow rate is conserved along the engine i.e., no injected fuel. In Fluent, the target mass flow rate option for pressure outlet is selected at the nacelle's entrance to match the mass flow rate generated at the nacelle's exit via the pressure inlet boundary condition.

5.4.2 Results & Discussion

Drag/thrust decompositions for the nine test cases are presented in Table 5.4. Columns 3 to 8 represent the viscous, spurious, induced, through-flow, adjusted through-flow, and scrubbing

[1] 1 drag count is worth $1/10,000^{th}$ of the drag coefficient

Table 5.3 Pressure inlet boundary conditions

Case	M_∞	T^0_{TE}/T^0_∞	p^0_{TE}/p^0_∞
1	0.60	2.0530	1.1700
2	0.60	2.2235	1.2176
3	0.60	2.5000	1.2000
4	0.60	1.0000	1.0000
5	0.75	2.0530	1.1700
6	0.75	2.2235	1.2176
7	0.75	2.5000	1.2000
8	0.75	1.0000	1.0000
9	0.50	1.0000	1.0938

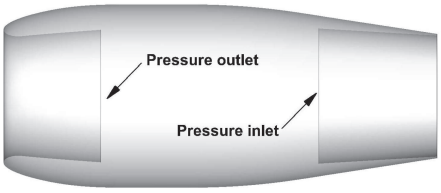

Figure 5.5 Power-on boundary conditions

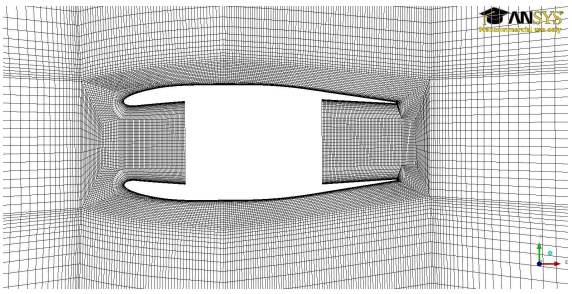

Figure 5.6 Mesh on CFM56 nacelle

drags respectively. Columns 9 to 11 list the pre-entry thrust, the basic thrust and, the standard net thrust computed with the proposed methods respectively. In the last four columns are shown the net propulsive force evaluated through the near-field and far-field approaches, and the configuration drag computed with two distinct ways for validation purposes. Note that the wave drag is not listed in this table because it is zero for all cases. Indeed, the local Mach number is always below unit. The induced drag is very small due to the axisymmetric nature of the flow. Values for the viscous, spurious, and scrubbing drag are not discussed in the present work because the method to compute those quantities has been extensively validated in previous works [25, 43, 47, 51]. One should note that when the adjusted through-flow drag D^*_{tf} is used, an exact near-field/far-field balance is achieved.

Table 5.4 Drag decomposition on CFM56 nacelle in power-on conditions (values in drag counts)

Property		Drag						Thrust			Net force		Conf. drag	
		C_d^v	C_d^{sp}	C_d^i	C_d^{tf}	C_d^{tf*}	C_d^{scrub}	C_T^{Pre}	C_T^B	C_T^N	C_F^{NF}	C_F^{FF}	$C_d^{c\,(1)}$	$C_d^{c\,(2)}$
Equation		(5.19)	(5.23)	(5.26)	(5.25)	(5.33)	(5.7)	(5.40)	(5.4)	(5.46)	(5.8)	(5.10)	(5.29)	(5.31)
Column #		3	4	5	6	7	8	9	10	11	12	13	14	15
Case	1	14.3	9.8	0.2	-18.1	-16.3	5.2	21.7	292.3	308.9	-251.7	-249.9	57.2	57.2
	2	13.9	10.9	0.2	-26.4	-24.4	5.8	18.7	361.8	374.7	-312.4	-310.4	62.3	62.3
	3	12.9	11.0	0.2	-14.9	-13.1	5.0	28.3	350.6	373.9	-313.5	-311.7	60.5	60.5
	4	17.4	4.7	0.2	-6.2	-5.0	4.0	17.4	9.2	22.6	18.1	19.3	40.7	40.7
	5	14.2	7.6	0.2	-6.1	-4.6	3.8	33.8	222.9	252.9	-196.4	-194.9	56.5	56.5
	6	13.2	8.8	0.2	-12.2	-10.6	4.0	32.0	272.5	300.4	-239.6	-238.1	60.8	60.8
	7	12.5	9.0	0.1	-0.5	1.0	3.6	42.2	266.4	304.9	-245.7	-244.3	59.2	59.2
	8	17.4	3.8	0.2	-7.1	-5.9	3.6	19.2	9.9	25.5	17.4	18.6	42.8	42.8
	9	19.9	9.8	0.4	-32.6	-30.3	10.5	-0.3	142.3	131.5	-81.9	-79.6	49.5	49.5

Table 5.5 Grid convergence study on case #1 (values in drag counts)

Property		Drag						Thrust			Net force		Conf. drag	
		C_d^v	C_d^{sp}	C_d^i	C_d^{tf}	C_d^{tf*}	C_d^{scrub}	C_T^{Pre}	C_T^B	C_T^N	C_F^{NF}	C_F^{FF}	$C_d^{c\,(1)}$	$C_d^{c\,(2)}$
Equation		(5.19)	(5.23)	(5.26)	(5.25)	(5.33)	(5.7)	(5.40)	(5.4)	(5.46)	(5.8)	(5.10)	(5.29)	(5.31)
Column #		3	4	5	6	7	8	9	10	11	12	13	14	15
Mesh	Coarse	11.8	19.5	0.1	-20.1	-16.9	7.4	20.9	294.0	307.6	-245.8	-242.5	61.8	61.8
	Medium	14.3	9.8	0.2	-18.1	-16.3	5.2	21.7	292.3	308.9	-251.7	-249.9	57.2	57.2
	Fine	18.0	4.0	0.2	-17.5	-16.4	4.5	21.9	291.7	309.0	-253.0	-251.9	56.0	56.0
Gap (%)		34.7	386.2	35.6	14.9	3.1	64.8	4.3	0.8	0.5	2.9	3.7	10.3	10.3

In power-on conditions, the near-field/far-field drag balance becomes the net propulsive force balance. It corresponds to the difference between columns 12 and 13 of Table 5.4. It is within 2 drag counts in average. For the configuration drag, both methods are in agreement within 0.01 drag count. Note that if the exact through-flow drag were used, the difference between the configuration drags would correspond to the difference between the near-field and far-field net propulsive forces.

For case #1, a grid convergence study was performed. Three meshes, containing 298 560, 2 388 480, and 19 107 840 cells were used. Results are summarized in Table 5.5 where the last line presents the relative gap between the coarse and fine meshes. Columns are the same as Table 5.4. Using Celik's method [60], the computed order of convergence p of the method is of 1.94 with the configuration drag as the quantity of interest, which is satisfactory. As expected, the spurious drag is decreasing with mesh refinement; from 20 drag counts on the coarse mesh to 4 drag counts on the fine mesh. We also notice that the thrusts and the net propulsive forces are less sensitive to mesh refinement than the drags. The fact that the

basic thrust variation is less than 0.8% proves that integration of $\vec{f_x}$ on S_{in} and S_{out} is almost invariable to the refinement. As for the drags, the variations are explained by the spurious drag which decreases with refinement. Spurious drag decay also explains the scrubbing drag variation from 7.4 to 4.5 drag counts and the configuration drag variation from 61.8 to 56.0 drag counts. It is possible to notice the increase in viscous drag. To study this phenomenon, we can separate the computational domain into four zones: upstream, wake, external and internal. The upstream and wake volumes are delimited as follows:

$$V_{\text{Upstream}} = \left\{(x, y, z) \in \mathbb{R}^3 : x < x_{\text{Leading edge}}\right\} \tag{5.47}$$

$$V_{\text{Wake}} = \left\{(x, y, z) \in \mathbb{R}^3 : x > x_{\text{Trailing edge}}\right\} \tag{5.48}$$

As for the internal and external volumes, the remaining cells are splitted depending if they are inside or outside the nacelle. Corresponding values are listed in Table 5.6. For all zones, the spurious and irreversible drags decrease with mesh refinement as expected. We also notice that all four zones beside the wake region present a viscous drag value invariable with mesh refinement. The latter increases from -6.3 to -0.2 drag counts. However, the irreversible drag, which in this case corresponds to the sum of the viscous plus spurious drag, is always positive in all regions, and decreases from 5.1 drag counts for the coarse mesh to 3.2 and 2.3 drag counts for the medium and fine meshes respectively in the wake region. The negative value is thus a consequence of the viscous sensor threshold. On a finer mesh, cells are smaller and the interaction between the inner and outer boundary layers is more defined as illustrated in Figs. 5.7-5.8 where the viscous sensor and the velocity magnitude are respectively plotted on a line located 0.5m from the nacelle's exit and perpendicular to the nacelle center line. We notice, on Fig. 5.7, a larger interaction zone on the coarse mesh than on the fine mesh. Again on Fig. 5.8, we notice that the jet is clearly distinct from the outside flow on the medium and fine meshes. However, on the coarse mesh at the same distance from the nacelle, both the inner and outer flows begin to merge. In such a case, some cells may be falsely assigned to the viscous volume which causes the viscous drag to yield incoherent values in the wake region. Cells are too large to solve accurately the interaction zone.

Table 5.6 Drag repartition on Case #1 (values in drag counts)

Zone		**External**			**Internal**			**Upstream**			**Downstream**			**Total**		
		$\mathbf{C_d^v}$	$\mathbf{C_d^{sp}}$	$\mathbf{C_d^{irr}}$	$\mathbf{C_d^v}$	$\mathbf{C_d^{sp}}$	$\mathbf{C_d^{irr}}$	$\mathbf{C_d^v}$	$\mathbf{C_d^{sp}}$	$\mathbf{C_d^{irr}}$	$\mathbf{C_d^v}$	$\mathbf{C_d^{sp}}$	$\mathbf{C_d^{irr}}$	$\mathbf{C_d^v}$	$\mathbf{C_d^{sp}}$	$\mathbf{C_d^{irr}}$
	Coarse	14.8	2.5	**17.3**	3.3	4.1	**7.4**	0.0	1.5	**1.5**	-6.3	11.4	**5.1**	11.8	19.5	**31.2**
Mesh	**Medium**	14.8	0.7	**15.5**	3.3	1.8	**5.2**	0.0	0.3	**0.3**	-3.9	7.1	**3.2**	14.3	9.8	**24.1**
	Fine	14.8	0.4	**15.2**	3.4	1.0	**4.5**	0.0	0.1	**0.1**	-0.2	2.5	**2.3**	18.0	4.0	**22.0**

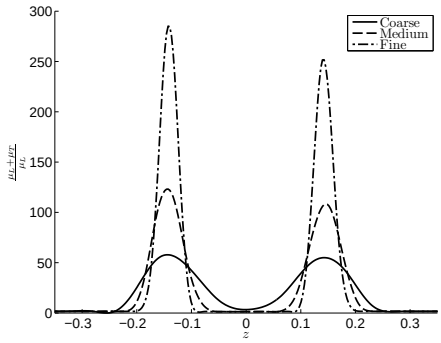

Figure 5.7 $\frac{\mu_L+\mu_T}{\mu_L}$ in nacelle's wake

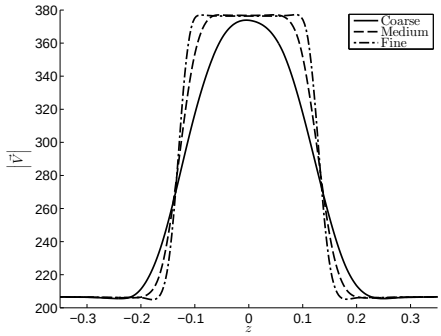

Figure 5.8 Velocity magnitude in nacelle's wake

Results for the pre-entry thrust are listed in Table 5.7. For each test case, columns 2 to 5 report the mass flow ratio and the pre-entry thrust computed with ESDU [62], the classical formulation, and the proposed method respectively. As expected, the pre-entry thrust is inversely proportional to the mass flow ratio. A lower MFR induces a more curved streamtube near the nacelle's inlet which translates in a higher pressure force in the x-direction, thus a higher pre-entry thrust. This behavior can be observed in Fig. 5.9 where the pre-entry thrust is plotted against the mass flow ratio.

One should note that the ESDU method is one-dimensional and uses isentropic relations. Those hypothesis are not met in the present case because the flow is not isentropic and is tridimensional. Therefore, ESDU and the proposed method are expected to yield different results. This validation intends to give the order of magnitude of the pre-entry thrust. For instance, the average discrepancy between the proposed method and ESDU is less than 6 drag counts. Furthermore, both methods have the same behavior when varying the mass flow ratio.

Table 5.7 Pre-entry Thrust

Case	MFR	Method (Eq. #)		
		ESDU (-)	Classical (5.2)	Proposed (5.40)
1	0.746	16.1	22.7	21.7
2	0.766	13.3	19.9	18.7
3	0.705	22.5	30.6	28.3
4	0.775	12.2	21.6	17.4
5	0.703	26.4	32.8	33.8
6	0.712	24.8	30.7	32.0
7	0.662	34.2	37.3	42.2
8	0.786	13.0	21.1	19.2
9	0.999	0.7	3.4	-0.3

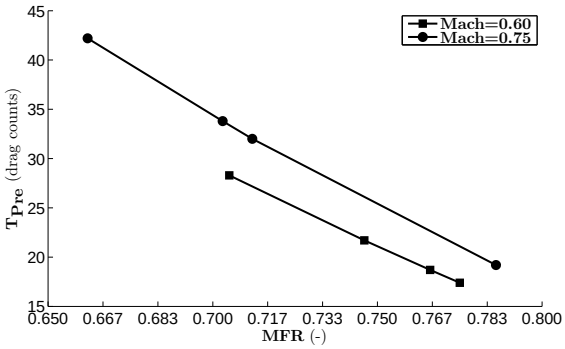

Figure 5.9 Pre-entry thrust (proposed) in function of mass flow ratio

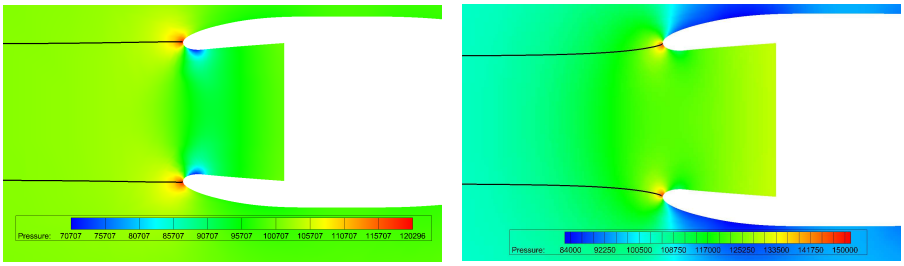

(a) MFR=1, Case #9 (b) MFR<1, Case #7

Figure 5.10 Impact of MFR on streamtube's shape

For validation purposes, the pre-entry thrust can also be computed by integrating the pressure on the streamtube as in Eq. (5.2). Results are reported in the fourth column of Table 5.7. A backward integration starting at the stagnation point has been performed and two thousand points per streamline were used. The average discrepancy between Eq. (5.2) and the new method is 2.1 drag counts. The discrepancy increases with the pre-entry thrust. For

instance, it is 1.1 drag count for the first case while it reaches 4.9 drag counts for the seventh case. A lower MFR means a higher pre-entry thrust and, in such cases, the streamtube becomes more and more curved near the nacelle's inlet as shown in Fig. 5.10(b) compared to Fig. 5.10(a). The more curved the streamtube is, the more mesh-dependent becomes the pre-entry thrust evaluation through Eq. (5.2), which explains the higher discrepancy. Furthermore, flow quantities must be interpolated at each integration step which is more likely to generate interpolation errors.

Note that, even though the results computed with Eq. (5.2) are in good agreement with the proposed method, the latter should be preferred over the former. The flow in all our tests is axisymmetric which means that only one streamline has to be computed in order to obtain the pre-entry thrust. This is not a typical situation. When the flow is not axisymmetric, streamlines have to be computed from the entire stagnation line. The more streamlines there are, the more accurate the results will be. Moreover, integrating pressure on the streamtube is a highly mesh-dependent process. This difficulty vanishes when using the far-field method [47].

An interesting validation case is when the mass flow ratio is equal to unit. The pre-entry thrust must then be zero because the streamtube has a cylindrical shape on which the x-component of the normal vector is expected to be zero. Such a situation is illustrated in Fig. 5.10 which compares the streamtubes of case #9 (Fig. 5.10(a)) and case #7 (Fig. 5.10(b)). The results in Table 5.7 show that the proposed method yields a value for the pre-entry thrust of -0.3 which is close to zero as expected. One should also notice a value of 3.4 drag counts for the classical integration method. A value closer to zero would have been expected. This shows that the classical method is sensitive to the stagnation point location and to the accuracy of the backward integration, which is not the case with the proposed method. Furthermore, it demonstrates the robustness and the superiority of the proposed technique.

Regarding the standard net thrust, it is possible to compare the proposed approach with an alternative formulation. The latter is derived by combining Eqs. (5.29) and (5.31). The standard net thrust is thus given by:

$$T_N = D_v + D_w + D_{sp} + D_i - D_{tf}^* - D_{scrub} + T_{Pre} - F_{FF} \tag{5.49}$$

Results for both Eq. (5.49) and the proposed method are listed in columns 2 and 3 of Table 5.8 respectively. Both methods are in agreement within 0.01 drag count as expected.

Table 5.8 Standard Net Thrust

Case	**Method**	
	Eq. (5.49)	**Proposed (Eq. (5.46))**
1	308.9	308.9
2	374.7	374.7
3	373.9	373.9
4	22.6	22.6
5	252.9	252.9
6	300.4	300.4
7	304.9	304.9
8	25.5	25.5
9	131.5	131.5

5.5 Conclusion

The far-field theory applied to a motorized configuration as well as a review of the book-keeping technique for CFD were presented. Two new methods to compute the standard net thrust and the pre-entry thrust, derived from the far-field formulation, were developed. All simulations were ran on the CFM56 nacelle in power-on conditions and boundary conditions were varied in order to test the accuracy of the proposed methods. Results of the new formulation for the pre-entry thrust were compared to the classical approach and to ESDU. The discrepancy between the proposed and the ESDU approaches were caused by the fact that the latter method's hypotheses were not met; the flow is tri-dimensional and non-isentropic. The proposed method and the classical formulation were within 2.1 drag counts on average. Furthermore, the new method to compute the pre-entry thrust does not depend on the stagnation line determination and computation of the streamtube is no longer compulsory, which form a great advantage. Thus, it is believed that it is well suited to study complex tridimensional geometry. The configuration drag was computed with two different formulations which are in excellent agreement. Near-field/far-field drag balance is within 2.3% and 1.7 drag counts on average. The proposed formulation for the standard net thrust is compared with an alternative formulation and results are in excellent agreement. Furthermore, for both proposed techniques, interpolation of flow quantities is no longer required.

CHAPITRE 6 ARTICLE 3: Installation and Interference Drag Decomposition Via RANS Far-Field Methods

Malouin, B., Trépanier, J. Y., and Laurendeau, É. (2015), Installation and Interference Drag Decomposition Via RANS Far-Field Methods, Submitted to Aerospace Science and Technology.

6.1 Abstract

Computation of the engine installation drag is important to both airframers and engine manufacturers who wish to assess performance of their respective system. This force comprises the interference drag that results from the interaction between the wing and the engine's nacelle. Its evaluation is cumbersome because of the coupled nature of this phenomenon. It is thus proposed to decompose the installation drag in terms of interference and nacelle drags that, using the far-field method, can be further discretize in terms of viscous, wave, induced, spurious and pre-entry forces. By using simulations on the isolated nacelle, the wing-body and the wing-body-pylon-nacelle configurations, it is thus possible to compute and decompose both the interference and installation drags. Simulations are performed with ANSYS Fluent 14.5 on the DLR-F6 equipped with CFM56 nacelles in power-on conditions.

6.2 Introduction

Global trends in fuel prices have lead airframers toward the use of very-high and ultra-high-bypass-ratios turbofan engines, which are more powerful and efficient than older generations engines [49]. However, the gain in power efficiency is partially overshadowed by the increase in installation drag in part due to higher wetted area. The installation drag is traditionally computed by subtracting the wing-body drag D^{WB} and the nacelle internal drag D^{scrub} from the wing-body-pylon-nacelle drag D^{WBPN}. The installation drag is composed of the nacelle and the interference drags. The latter is difficult to evaluate since it represents a coupled phenomenon involving the wing and the nacelle. The objective of this paper is to propose a method to estimate the installation and interference drags using the far-field approach.

The development of the far-field drag decomposition method made possible the identification of the main cause of drag creation for a given configuration in term of physical phenomena producing drag such as the boundary layer and the shock wave phenomena [20, 25, 34, 51].

Later, Tognaccini [50] and, Van der Vooren and Destarac [46] applied this method to powered configurations. Recently, Malouin et al. [48] proposed a new method to compute the pre-entry thrust and the standard net thrust based solely on the far-field theory yielding a more accurate method to study powered configurations. With all these tools available, it is now possible to decompose the installation drag. In this paper, we propose to decompose this force into two major components: the nacelle drag and the interference drag. For each, the far-field method, based on entropy generation, allows separation of each component in terms of the physical phenomena accountable for drag production.

In this paper, the chosen configuration is the DLR-F6 since it is public and is supplemented with experimental data in power-off conditions [58]. The lack of either numerical or experimental data in power-on conditions makes it difficult to validate the results. To overcome this issue, we propose to proceed via a step by step procedure. First, the DLR-F6 with through-flow nacelle (TFN) is simulated and results are validated with the available experimental data. Then, the TFN is replaced by a turbine powered simulater (TPS) with power-on boundary conditions used to reproduce the TFN flow. To verify the implementation of the TPS boundary conditions, the configuration drags are compared. Since the flow is the same, the configuration drags of both the TFN and TPS cases should be equals. In fact, there is a small discrepancy which is explained by the inclusion of the boundary conditions. Nevertheless, results are in good agreement and this discrepancy is further detailed. The next step is to compute and decompose the installation drag on the DLR-F6 TPS case , but still without thrust. The presence of those boundary conditions leads to the use of the configuration drag instead of the typical near-field net propulsive force which could be negative because of thrust generation. The advantage of this modification is that the pre-entry thrust of the nacelle can be computed and included in the installation drag. Since there is no available data for validation, the installation drag is validated based on the near-field/far-field balance which is in good agreement. Finally, thrust is added to the configuration by increasing the total pressure and total temperature ratios. Again, the installation drags are in good agreement.

The next section presents an overview of the far-field theory to compute drag and thrust and thrust/drag bookkeeping in CFD. It is followed by the development of the proposed approach to separate the installation drag in terms of nacelle and interference drags.

6.3 Theory

The difference between the configuration drag D_c and the thrust T is the net propulsive force $F = D_c - T$, which is constant at given flow conditions for a given configuration. However, many definitions for the thrust are available and, regarding the user's choice, the thrust and the drag can vary. In the following section, forces on a motorized aircraft are described. It is followed by a summary of the far-field method used to compute these forces. Then, new approaches to compute the standard net thrust and the pre-entry thrust are proposed.

6.3.1 Forces on configuration

Consider the isolated nacelle in power-on conditions depicted in Fig. 6.1. Note that the small red arrows represent the normal vectors. The forces applied to this configuration are:

- Pre-entry thrust
- Standard net thrust
- Basic thrust
- Scrubbring drag
- Aircraft drag

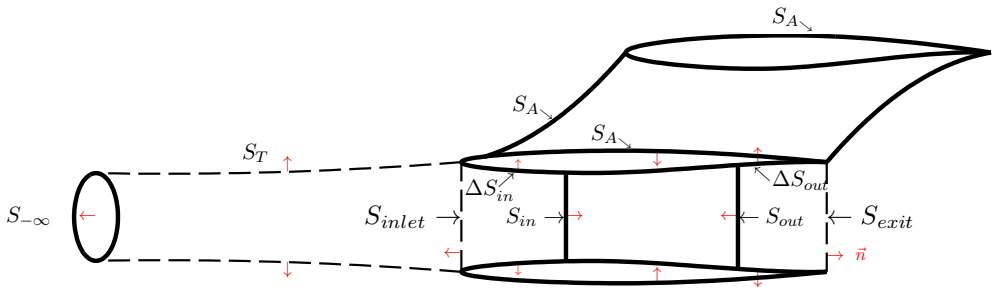

Figure 6.1 Isolated nacelle geometry and surfaces

The pre-entry thrust T_{Pre}, also known as additive drag, corresponds to the difference in stream forces between the nacelle entry and the streamtube captation area located infinitely far upstream ($S_{-\infty}$) [62]. This force appears when the mass flow ratio is different than unity. The mass flow ratio MFR can be computed as follows:

$$\text{MFR} = \frac{S_{-\infty}}{S_{inlet}} \tag{6.1}$$

where S_{inlet} is determined by the nacelle's most forward points plane. In this paper, the hypothesis is made that the shear stress is negligible on S_T because it is far from a wall and, since the streamtube is located upstream of the nacelle, it is not affected by the viscous wake. The standard net thrust $\mathrm{T_N}$ constitutes the basis of most bookkeeping systems because it uses the captation surface $S_{-\infty}$ [1]. This surface is a clever choice because the flow is undisturbed infinitely far upstream and its definition is not function of the geometry. Therefore, it is free of ambiguity. The basic thrust $\mathrm{T_B}$ can be considered as the force generated by the engine. Definitions of all thrusts are listed in Table 6.1.

Table 6.1 Thrusts definitions

Name	Symbol	Vector	Surfaces	Equation
Pre-entry thrust	$\mathrm{T_{Pre}}$	$-(p-p_\infty)\,n_x + (\vec{\tau}_x \cdot \vec{n})$	S_T	
Standard net thrust	$\mathrm{T_N}$	$\rho u\left(\vec{V}\cdot\vec{n}\right) + (p-p_\infty)\,n_x - (\vec{\tau}_x \cdot \vec{n})$	$S_{-\infty} \cup S_{exit}$	(6.2)
Basic thrust	$\mathrm{T_B}$	$-\rho\,(u-u_\infty)\left(\vec{V}\cdot\vec{n}\right) - (p-p_\infty)\,n_x + (\vec{\tau}_x \cdot \vec{n})$	$S_{in} \cup S_{out}$	(6.3)
				(6.4)

The total friction and pressure drags generated on the nacelle's skin $S_{skin} = S_A \cup \Delta S_{in} \cup \Delta S_{out}$ correspond to the sum of the nacelle's external drag and the scrubbing drag. The former being the drag produced by the airflow passing outside the engine while the latter corresponds to the drag generated by the inside flow on the nacelle's surfaces. The nacelle's external drag D_A is defined as follows:

$$\mathrm{D_A} = \int_{S_A} \left[(p-p_\infty)\,n_x - (\vec{\tau}_x \cdot \vec{n})\right] dS \tag{6.5}$$

where S_A represents all surfaces that are not wetted by the captured streamtube. Note that, when a full aircraft configuration is studied, $\mathrm{D_A}$ corresponds to the aircraft drag. In such a case, S_A is composed of the nacelle's external surface, the pylons, the wings, and the fuselage.

6.3.2 Far-field method in power-on conditions

This method was extensively detailed in many references [13,34,46,47,51,52] that the reader can consult for further information. However, it is briefly recalled in the following lines for convenience.

Consider the configuration depicted in Fig. 6.1. The near-field $\mathrm{F_{NF}}$ and far-field $\mathrm{F_{FF}}$ net propulsive forces are computed as follows:

$$\mathrm{F_{NF}} = -\int_{S_c} \left(\vec{f}\cdot\vec{n}\right) dS \tag{6.6}$$

where $S_c = S_A \cup S_{in} \cup S_{out} \cup \Delta S_{in} \cup \Delta S_{out}$ and

$$\mathrm{F_{FF}} = \int_{S_\infty} \left(\vec{f}\cdot\vec{n}\right) dS \tag{6.7}$$

where the momentum vector $\vec{f}$ is defined by:

$$\vec{f} = -\rho(u-u_\infty)\vec{V} - (p-p_\infty)\vec{i} + \vec{\tau_x} \tag{6.8}$$

where S_∞ is the surface of a control volume surrounding the whole configuration. It should be noted that the net propulsive force corresponds to the difference between the aircraft drag and the thrust that it generates. One way to compute the aircraft drag is to integrate the pressure and viscous forces on $S_{skin} = S_A \cup \Delta S_{in} \cup \Delta S_{out}$ as follows:

$$\mathrm{D_{NF}} = -\int_{S_{skin}} \left(\vec{f}\cdot\vec{n}\right) dS \tag{6.9}$$

At this stage, the drag cannot be decomposed. We shall divide the momentum vector into two components regarding entropy production. The first component, associated with entropy production and thermodynamically irreversible processes such as shock waves and boundary layers can be computed as follows:

$$\vec{f_{vw}} = -\rho\Delta\bar{u}\vec{V} \tag{6.10}$$

where $\Delta\bar{u} = \bar{u} - u_\infty$ is defined as follows:

$$\Delta\bar{u} = u_\infty\sqrt{1 + 2\frac{\Delta H}{u_\infty^2} - \frac{2}{(\gamma-1)M_\infty^2}\left[\left(e^{\frac{\Delta s}{R}}\right)^{\frac{\gamma-1}{\gamma}} - 1\right]} - u_\infty \tag{6.11}$$

and entropy variation from the free stream state Δs is given by:

$$\Delta s = \frac{R}{\gamma-1}\log\left[\frac{p}{p_\infty}\left(\frac{\rho_\infty}{\rho}\right)^\gamma\right] \tag{6.12}$$

and enthalpy variation from the free stream state ΔH is given by:

$$\Delta H = \frac{\gamma}{\gamma - 1}\left(\frac{p}{\rho} - \frac{p_\infty}{\rho_\infty}\right) + \frac{u^2 + v^2 + w^2}{2} - \frac{u_\infty^2}{2} \tag{6.13}$$

On the counterpart, the component of $\vec{f}$ associated with thermodynamically reversible processes such as the exchange of mechanical energy at wing tip vortices [12,25] can be computed as follows:

$$\vec{f_i} = \vec{f} - \vec{f_{vw}} = -\rho(u - u_\infty - \Delta\bar{u})\vec{V} - (p - p_\infty)\vec{i} + \vec{\tau}_x \tag{6.14}$$

Finally, the irreversible drag $\mathrm{D_{irr}}$ can be expressed by:

$$\mathrm{D_{irr}} = \int\limits_{S_\infty \cup S_{nac}} \left(\vec{f_{vw}} \cdot \vec{n}\right) dS \tag{6.15}$$

which, using Ostrogradsky's theorem, can be transformed into a volumetric integral, as follows:

$$\mathrm{D_{irr}} = \int\limits_{V} \left(\vec{\nabla} \cdot \vec{f_{vw}}\right) dV \tag{6.16}$$

where V is the volume delimited by S_∞.

Being a volumetric integral, it is possible to limit the integration to shock volume V_W and viscous volume V_V. Thus, the wave and viscous drags can be obtained as follows:

$$\mathrm{D_v} = \int\limits_{V_V} \left(\vec{\nabla} \cdot \vec{f_{vw}}\right) dV \tag{6.17}$$

$$\mathrm{D_w} = \int\limits_{V_W} \left(\vec{\nabla} \cdot \vec{f_{vw}}\right) dV \tag{6.18}$$

To automate volume selection, sensors are used [15, 50]. The viscous volume is given by:

$$V_V = \left\{(x, y, z) \in \mathbb{R}^3 : \frac{\mu_l + \mu_t}{\mu_l} \geq 1.1\left(\frac{\mu_l + \mu_t}{\mu_l}\right)_\infty\right\} \tag{6.19}$$

and the shock volume V_W is given by:

$$V_W = \left\{ (x, y, z) \in \mathbb{R}^3 : \frac{\vec{V} \cdot \nabla p}{a|\nabla p|} \geq 1 \right\} \tag{6.20}$$

Note that it is assumed that a numerical solution via Reynolds Averaged Navier-Stokes with turbulence modeling is available (i.e. ρ, $\vec{v}$, p and μ_t entirely available).

Regions outside boundary layers or shock waves are expected to be isentropic. In such cases, the axial velocity defect $\Delta\bar{u}$ and the value of the integral in Eq. (6.16) should vanish. However, it is not necessarily the case. Spurious drag is thus obtained by evaluating Eq. (6.16) in volumes where the flow is expected to be isentropic, i.e. $V_{sp} = V/(V_V \cup V_W)$. Spurious drag can be expressed as follows:

$$\mathrm{D_{sp}} = \int\limits_{V_{sp}} \left(\vec{\nabla} \cdot \vec{f}_{vw} \right) dV \tag{6.21}$$

Spurious drag is caused by artificial dissipation that is implemented in flow solvers to enhance convergence and stability. However, it pollutes the numerical results, which is why the ability to quantify it and remove it is one of the key advantages of the far-field method.

With this far-field method, it is then possible to post-treat a CFD solution and decompose the physical drag into its components, i.e. wave, viscous, induced, and spurious drag. Some examples of the method applied to non-motorized configurations are given in Refs. [20–22,29,34,51].

6.3.3 Recent improvements in the far-field method

In motorized configuration, the engine faces (S_{in} and S_{out}) can contribute to the reversible drag. Van der Vooren and Destarac [46] introduced a new definition, the additive through-flow drag, which can be computed as follows:

$$\mathrm{D_{tf}} = -\int\limits_{S_{in} \cup S_{out}} \left(\vec{f}_i \cdot \vec{n} \right) dS + \int\limits_{S_{in} \cup S_{out}} \frac{\rho}{2} \left(v^2 + w^2 \right) n_x dS \tag{6.22}$$

The last term of the latter equation represents the crossflow kinetic energy generated by the engines. For power-on configurations the induced drag is computed as follows [46]:

$$\begin{aligned} \mathrm{D_i} = & \int\limits_{V_V \cup V_W \cup V_{sp}} \left(\vec{\nabla} \cdot \vec{f_i}\right) dV - \int\limits_{S_{skin} \cup S_{in} \cup S_{out}} \left(\vec{f_i} \cdot \vec{n}\right) dS \\ & + \int\limits_{S_{in} \cup S_{out}} \frac{\rho}{2} \left(v^2 + w^2\right) n_x dS \end{aligned} \tag{6.23}$$

Thus, the exact near-field/far-field drag balance becomes:

$$\left(\mathrm{D_p} + \mathrm{D_f}\right)_{S_{skin}} = \mathrm{D_v} + \mathrm{D_w} + \mathrm{D_{sp}} + \mathrm{D_i} - \mathrm{D_{tf}} \tag{6.24}$$

where $\mathrm{D_p}$ and $\mathrm{D_f}$ are the pressure and friction drags, respectively. From this equation, we notice that the sum of friction plus pressure drags is equal to the sum of the irreversible drag, composed of the viscous, wave and spurious drags, and reversible drag, composed of the induced and through-flow drags.

One should note that it is not possible to use Eq. (6.11) when the total pressure loss becomes significant because, in such cases, entropy decreases and the value of the square root becomes negative. To overcome this problem, Gariépy et al. [34] proposed a new formulation:

$$\begin{aligned} \Delta\bar{u} = u - u_\infty \left(\left[1 + \frac{2\Delta H}{u_\infty^2} - \frac{2}{(\gamma - 1) M_\infty^2} \left[\left(\frac{p}{p_\infty} \right)^{\frac{\gamma - 1}{\gamma}} - 1 \right] \right. \right. \\ \left. \left. - \frac{v^2 + w^2}{u_\infty^2} \right]^{1/2} + 1 \right) \end{aligned} \tag{6.25}$$

Note that an hybrid method is used here. The new formulation of Eq. (6.25) is used only when the classical formulation of Eq. (6.11) is undefined.

Another advantage of the far-field method that is relevant to our application is its ability to compute drag in subvolumes. For example, it is possible to compute drag in the nacelle's internal volume as described in Ref. [47]. Thus, the scrubbing drag is computed as follows:

$$\mathrm{D_{scrub}} = \int\limits_{V_{int}} \left(\vec{\nabla} \cdot \vec{f_{vw}}\right) dV \tag{6.26}$$

where $V_{int} = V_{int,\ up} \cup V_{int,\ down}$ and $V_{int,\ up}$ is the volume delimited by S_{inlet}, S_{in} and ΔS_{in},

and $V_{int,\ down}$ is the volume delimited by S_{exit}, ΔS_{out} and S_{out}.

Recently, Malouin et al. [48] developped new formulations for the pre-entry thrust and the standard net thrust as follows:

$$\mathrm{T_{Pre}} = \int\limits_{S_{-\infty} \cup S_{in}} \left(\vec{f}_x \cdot \vec{n}\right) dS + \int\limits_{V_{int,\ up}} \left(\vec{\nabla} \cdot \vec{f}_{vw}\right) dV \tag{6.27}$$

$$\mathrm{T_N} = \int\limits_{S_{-\infty}} \left(\vec{f}_x \cdot \vec{n}\right) dS - \int\limits_{S_{out}} \left(\vec{f}_x \cdot \vec{n}\right) dS - \int\limits_{V_{int,\ down}} \left(\vec{\nabla} \cdot \vec{f}_{vw}\right) dV \tag{6.28}$$

The standard net thrust can also be computed as follows:

$$\mathrm{T_N} = \mathrm{T_{Pre}} + \mathrm{T_B} - \mathrm{D_{scrub}} \tag{6.29}$$

6.3.4 Thrust/Drag Bookkeeping

It is common practice that engine and airframe manufacturers distinguish the performance of their systems by separating phenomena occuring inside or outside the captured streamtubes. To this end, the configuration drag cannot be computed using Eq. (6.9) because contributions of inside and outside flows must be separated. Since the net propulsive force F is invariant at given flow conditions for a given configuration, the configuration drag $\mathrm{D_c}$, which corresponds to the difference between the net propulsive force and the thrust, is dependent on the thrust definition used: basic, standard net or intrinsic. Since the common practice is to use the standard net thrust [1, 50], the net propulsive force and the configuration drag are expressed as follows:

$$\mathrm{F} = \left(\mathrm{D_p} + \mathrm{D_f}\right)_{S_A} - \left(\mathrm{T_N} - \mathrm{T_{Pre}}\right) \tag{6.30}$$

$$\mathrm{D_c} = \left(\mathrm{D_p} + \mathrm{D_f}\right)_{S_A} + \mathrm{T_{Pre}} \tag{6.31}$$

where $\mathrm{T_{Pre}}$ and $\mathrm{T_N}$ are computed with Eqs. (6.27)-(6.28) respectively.

As stated earlier, the standard net thrust is usually used in bookkeeping systems. Thus, the difference between the near-field net propulsive force $\mathrm{F_{NF}}$ and the standard net thrust $\mathrm{T_N}$

yields the configuration drag D_c as follows:

$$D_c = F_{NF} + T_N \tag{6.32}$$

Note that a negative value of the net propulsive force means a thrust. From the far-field method, it is possible to substitute the pressure and friction drag by the wave, viscous, spurious, through-flow, and induced drags as follows:

$$D_c = D_v + D_w + D_{sp} + D_i - D_{tf} - D_{scrub} + T_{Pre} \tag{6.33}$$

However, in order to ensure an exact near-field/far-field net propulsive force balance, it is possible to use an alternative formulation for the additive through-flow drag D^*_{tf}. By combining Eq.(6.24) with an equivalent definition for the net propulsive force based on the basic thrust T_B defined as follows:

$$F = (D_p + D_f)_{S_{skin}} - T_B \tag{6.34}$$

we get

$$F_{NF} = D_v + D_w + D_{sp} + D_i - D_{tf} - T_B \tag{6.35}$$

By isolating D_{tf}, we obtain D^*_{tf}:

$$D^*_{tf} = D_v + D_w + D_{sp} + D_i - F_{NF} - T_B \tag{6.36}$$

Thus, by substituting D_{tf} by D^*_{tf} the exact near-field/far-field balance is guaranteed.

6.3.5 Installation drag decomposition in power-on conditions

The installation drag is typically computed as follows:

$$F^{install} = F^{WBPN} - F^{WB} - D^{scrub} \tag{6.37}$$

where F represents the net propulsive force i.e. the drag in power-off. In a situation where thrust is produced, this force will be negative because the integration surface includes the nacelle's inlet and oulet where a gain in momentum is generated. To overcome this phenomenon, we use the configuration drag D_c as detailed by Van der Vooren and Destarac [46]. The installation drag thus becomes:

$$D_c^{install} = D_c^{WBPN} - D_c^{WB} \tag{6.38}$$

It would also be interesting to decompose the installation drag, not only in physical phenomena sources of drag, but also in term of aircraft components. This force represents the cost of including the engines to the configuration [3]. It consists mainly of the nacelle drag, but also includes the interference drag. When two bodies are brought close to each other they mutually affect the flow around them causing the total drag of the bodies to be different than the sum of their isolated drag [63]. This difference is called the interference drag and it is also present in the case of engine/airframe integration.

We propose, using the far-field method, to decompose the configuration installation drag $D_c^{install}$ in terms of the nacelle D_c^{NAC} plus the interference D_c^{inter} drags as follows:

$$D_c^{install} = D_c^{NAC} + D_c^{inter} \tag{6.39}$$

where the configuration interference drag D_c^{inter} is defined as follows:

$$D_c^{inter} = D_c^{WBPN} - D_c^{WB} - D_c^{NAC} \tag{6.40}$$

Each of the configuration installation and interference drags can be decomposed in terms of entropy drag production. So the "k" installation drag ΔD_k is defined as follows:

$$\Delta D_k = D_k^{NAC} + \delta D_k \tag{6.41}$$

where δD_k corresponds to the interference drag of the "k" component which is defined as follows:

$$\delta D_k = D_k^{WBPN} - D_k^{WB} - D_k^{NAC} \tag{6.42}$$

Note that, in this case, the pylon drag would fall inside the interference drag component, and "k" represents any of the physical drag source of the configuration drag i.e. viscous, spurious, wave, etc.

To the authors' knowledge, it is the first time such an approach is proposed to decompose the installation drag in terms of nacelle and interference drag by decomposing those two

forces in terms of the viscous, wave, spurious, induced, additive through-flow and pre-entry forces. This technique, which constitutes the main contribution of this paper, is applied to the DPW2 test case in power-on conditions without and with thrust. Results are presented in Sections 6.4.2 and 6.4.2.

6.4 Test cases

6.4.1 Flow conditions, meshes, & algorithm

The flow conditions are listed in Table 6.2. The meshes, generated with ICEM-CFD, and providing values of $y+$ below 1, are shown in Figs. 6.2-6.3[1]. Mesh details are listed in Table 6.3. Note that the TFN mesh is the same as the TPS mesh, but with an extra block inside the nacelle. All the simulations were run with ANSYS Fluent 14.5 CFD software. The Spalart-Allmaras [55] turbulence model was used, with a 4% turbulence viscosity ratio at the far-field boundaries, which were set to pressure-far-field. The density-based solver combined with the implicit Roe scheme was selected, and second order upwind resolution associated with the Green-Gauss cell center algorithm was used. For all the simulations, the residuals were dropped below 10^{-6}, and the drag coefficients were stable within less than 0.01 drag count between two successive iterations.[2]

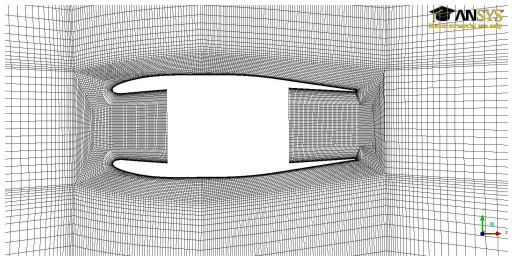

Figure 6.2 Mesh on CFM56 nacelle

6.4.2 Results & Discussion

Configuration drag

The objective of this test case is to validate the configuration drag. It is done by comparing a TFN with a TPS where the boundary conditions on the latter are set to match the flow

[1] DLR-F6 meshes are provided by the second drag prediction workshop (DPW2) committee
[2] 1 drag count is worth $1/10,000^{th}$ of the drag coefficient

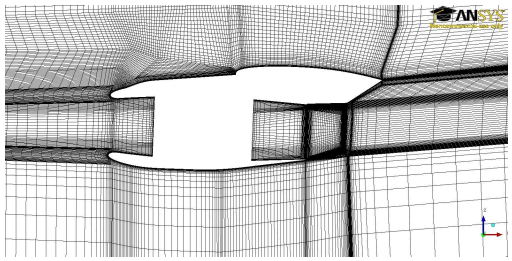

Figure 6.3 Mesh on Wing-Body-Pylon-Nacelle

Table 6.2 Flow properties

Property	**Value**	**Units**
T_∞	300	K
M_∞	0.75	-
ρ_∞	1.176674	kg/m^3
p_∞	101325	Pa
c	0.1412	m
S_{ref}	0.0727	m^2
Re_c	$3{\cdot}10^6$	-
μ	$1.4421 \cdot 10^{-5}$	$kg/m \cdot s$

Table 6.3 Meshes

Case	**Coarse**	**Medium**	**Fine**
Isolated TFN	303 072	2 424 576	19 396 608
Isolated TPS	298 560	2 388 480	19 107 840
WB	3 374 848	5 715 968	9 966 592
WBPN TFN	4 787 392	8 290 304	13 481 984
WBPN TPS	4 732 096	8 232 960	13 412 352

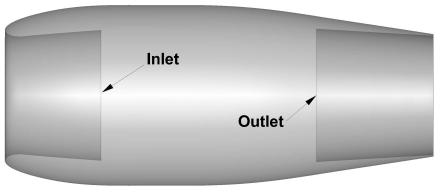

Figure 6.4 Nacelle boundary conditions

of the former. The mass flow rate measured from the TFN is imposed to the TPS via mass flow inlet boundary conditions. Results are summarized in Table 6.4. Columns 2 to 8 list the viscous, spurious, induced, real and adjusted through-flow and the scrubbing drags, respec-

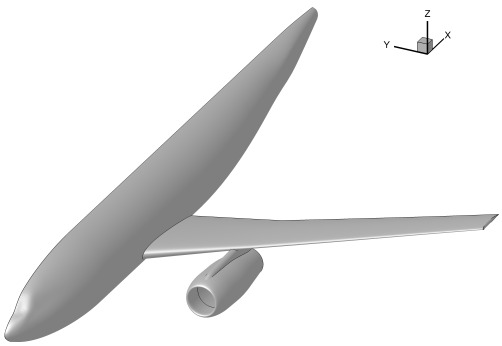

Figure 6.5 DLR-F6

tively. Columns 9, 10 and 11 correspond to the pre-entry, standard net and basic thrusts, respectively while columns 12 and 13 are associated with the near-field and far-field net propulsive forces. Finally, columns 14 and 15 contain the configuration drag computed with two distinct approaches. The symbol "-" means that the property cannot be computed for the TFN case because S_{in} and S_{out} do not exist. Furthermore, the TFN and TPS pre-entry thrusts are equal because the mass flow rates are equals, and the same geometry at the same flow conditions is studied.

The decrease in the scrubbing drag, listed in column 8, is explained by the smaller internal wetted area for the TPS case. On the fine mesh, it decreases by 1.2 drag counts. This corresponds to a decrease of 23% while, using empirical correlations, a decrease of 31% is obtained.

There is also a variation in the viscous and spurious drags listed in columns 2 and 4 respectively. Between the TFN and the TPS, on the fine mesh, the viscous drag decreases by 3.4 drag counts while the spurious drag increases by 2.6 counts yielding a net decrease of 0.8 drag count in the entropy drag. The viscous drag is expected to decrease due to the smaller wetted area. Between the TFN and the TPS cases, there is an exchange of entropy drag from viscous toward spurious. This is explained by the boundary conditions of the TPS case. Indeed, for the TFN case, the inner boundary layer evolves naturally while, for the TPS case, a new boundary layer is created from the nacelle's oulet plane (see Fig. 6.4) which affects the downwind flow. A deeper analysis of the viscous and spurious drag is presented, for the fine mesh, in Table 6.5 where the upstream and wake regions are defined as follows:

$$V_{\text{Upstream}} = \left\{(x, y, z) \in \mathbb{R}^3 : x < x_{\text{Leading edge}}\right\} \tag{6.43}$$

$$V_{\text{Wake}} = \left\{(x, y, z) \in \mathbb{R}^3 : x > x_{\text{Trailing edge}}\right\} \tag{6.44}$$

As for the internal and external volumes, the remaining cells are splitted whether they are inside or outside the nacelle. Results presented in Table 6.5 show that the flow downwind the nacelle exhaust is reponsible for the spurious drag increase. In the wake region, spurious drag increases by 2.4 drag counts while viscous drag decreases by 2.1 counts. This is merely a shift from viscous to spurious due to the mass flow inlet boundary condition. The latter is the only explanation for such a shift. Furthermore, the external drag is constant between the TFN and the TPS cases which proves that the TFN was well imitated by the TPS. Contours of pressure difference on Fig. 6.6 also supports the last statement. Indeed, the differences are mainly located downstream of the exit plane.

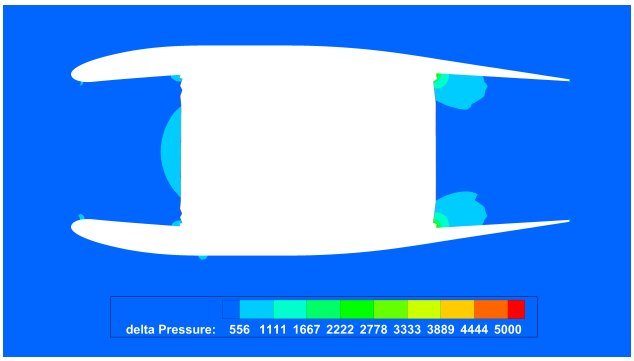

Figure 6.6 Pressure contours on CFM56

For each case, both methods for the configuration drag are in agreement within 0.1 drag count, but a difference of 9.7, 9.6 and 9.0 counts for the coarse, medium and fine meshes, respectively, is present between the TFN and the TPS cases. This difference corresponds to the additive through-flow drag listed in column 6. For the TFN case, the additive through-flow drag is not computed because S_{in} and S_{out} do not exist. However, by looking at Eq. (6.35), it is possible to reckon that the basic thrust $\mathrm{T_B}$ must equal the negative of the additive through-flow drag $-\mathrm{D_{tf}}$ since, for a TFN, the near-field drag corresponds to the sum of the viscous, spurious, wave and induced drag. By looking at columns 6 and 11 of Table 6.4 it is possible to conclude that this is the case. This observation supports that the TFN flow is well reproduced by the TPS.

It is also possible to compute $\mathrm{D_{tf}}$ for the TFN case by integrating Eq. (6.22) at the same locations. Results are reported in Table 6.6. The differences listed in the last column are less than 2 counts and are explained by the boundary conditions for the same aforementioned

reasons. To demonstrate this statement, it is possible to compute the integral of Eq. (6.22) on S_{in} and S_{out} separately. Results are listed in Table 6.6. The value of the integral remains almost constant on S_{in} while it decreases on S_{out}. For the fine mesh, the value on S_{in} increases by 0.1 counts while it decreases by 1.8 counts on S_{out} for a net difference of 1.7 drag counts, again weak. This highlights that S_{out} has the main influence on the additive through-flow drag variation between the TFN and the TPS, and shows that the difference in this quantity is due to the boundary condition which is unable to perfectly reproduce the TFN flow. The only reason for such a behaviour is thus the difference in boundary layers between both cases.

Table 6.4 Results for isolated CFM56 TFN and TPS with TFN boundary conditions (values in drag counts)

Property		**Drag**						**Thrust**			**Net force**		**Conf. drag**	
		C_d^v	C_d^{sp}	C_d^i	C_d^{tf}	C_d^{tf*}	C_d^{scrub}	C_T^{Pre}	C_T^N	C_T^B	C_F^{NF}	C_F^{FF}	$C_d^{c\,(1)}$	$C_d^{c\,(2)}$
Equation		(6.17)	(6.21)	(6.23)	(6.22)	(6.36)	(6.26)	(6.27)	(6.29)	(6.4)	(6.6)	(6.7)	(6.32)	(6.33)
Column #		2	4	5	6	7	8	9	10	11	12	13	14	15
	TFN	25.3	14.2	0.0	-	-	7.3	28.9	21.6	-	39.6	39.5	61.2	61.1
Coarse	**TPS**	22.6	14.6	0.4	-8.7	-9.8	5.4	28.9	32.4	8.9	38.5	37.3	70.9	70.9
	Δ	-2.7	0.4	0.4	-	-	-1.8	0.0	10.8	-	-1.1	-2.2	9.7	9.7
	TFN	27.1	4.1	0.0	-	-	5.5	28.9	23.4	-	31.2	31.2	54.6	54.6
Medium	**TPS**	23.7	6.6	0.4	-8.2	-8.6	4.1	28.9	32.8	7.9	31.4	31.1	64.1	64.1
	Δ	-3.4	2.5	0.4	-	-	-1.5	0.0	9.4	-	0.1	-0.1	9.5	9.6
	TFN	27.0	2.0	0.0	-	-	5.3	28.6	23.3	-	29.1	29.1	52.4	52.3
Fine	**TPS**	23.6	4.6	0.4	-8.3	-8.3	4.1	28.6	32.6	8.1	28.8	28.8	61.4	61.4
	Δ	-3.4	2.6	0.4	-	-	-1.2	0.0	9.3	-	-0.3	-0.3	9.0	9.0

From TPS case

Table 6.5 Viscous and spurious drag distribution on the TFN/TPS case on the fine mesh (values in drag counts)

Location	**Total**			**External**			**Upwind**			**Wake**			**Internal**		
Case	**TFN**	**TPS**	**Δ**	**TFN**	**TPS**	**Δ**	**TFN**	**TPS**	**Δ**	**TFN**	**TPS**	**Δ**	**TFN**	**TPS**	**Δ**
Viscous	27.0	23.6	-3.4	20.4	20.5	0.1	0.0	0.0	0.0	1.9	-0.2	-2.1	4.7	3.3	-1.4
Spurious	2.0	4.6	2.6	1.0	1.1	0.1	0.1	0.1	0.0	0.3	2.7	2.4	0.6	0.8	0.2

Table 6.6 Additive through-flow drag TFN vs. TPS (values in drag counts)

Case	$\mathbf{D_{tf}^{TFN}}$			$\mathbf{D_{tf}^{TPS}}$			$\mathbf{\Delta D_{tf}}$
Surface	$\mathbf{S_{in}}$	$\mathbf{S_{out}}$	$\mathbf{S_{in} \cup S_{out}}$	$\mathbf{S_{in}}$	$\mathbf{S_{out}}$	$\mathbf{S_{in} \cup S_{out}}$	$\mathbf{S_{in} \cup S_{out}}$
Coarse	28.0	-34.8	-6.8	28.6	-37.3	-8.7	1.9
Medium	28.7	-35.4	-6.7	29.1	-37.3	-8.2	1.5
Fine	28.8	-35.5	-6.6	29.0	-37.2	-8.3	1.7

Installation drag in power-off

The objective of this test case is to compute and validate the installation drag. Experimental results on the DLR-F6 are available through Ref. [58]. Flow conditions are listed in Table 6.2 and the lift coefficient C_L is 0.5. For each case, the angle of attack is tuned to achieve the required lift.

Results on the three meshes are presented in Table 6.7. Are also presented results from other participants of the second drag prediction workshop (DPW2) and the experimental values [58]. On the fine mesh, the computed installation drag is 44.9 counts while the average of other DPW2 participants is 42.4 counts and the experimental data is 37.2 counts. This difference may seem high, however, the relative errors in drag coefficients for the Wing-Body and Wing-Body-Pylon-Nacelle cases compared to experimental results on the fine mesh are less than 0.1% and 2.5%, respectively. It is thus possible to conclude that the present results are validated and satisfactory.

Table 6.7 Installation drag comparison with other DPW2 participants and experimental results (in drag counts)

C_D	Present			Average of DPW2 participants			Experimental		
	WB	**WBPN**	**Install**	**WB**	**WBPN**	**Install**	**WB**	**WBPN**	**Install**
Coarse	299.3	355.6	49.9	297.1	350.0	45.2			
Medium	298.2	353.1	48.5	288.7	340.1	44.0	295.0	338.0	37.2
Fine	294.9	346.2	44.9	286.5	336.8	42.4			

Drag decomposition is performed and results are listed in Table 6.8. The viscous drag, listed in column 2, is expected to be higher, 244.9 counts compared to 203.0 counts on the fine mesh, due to the larger wetted area on the WBPN. The addition of the nacelle requires more artificial dissipation from the solver which increases the spurious drag, listed in column 4. Indeed, on the fine mesh the spurious drag is 5.2 counts compared to 1.2 counts on the WB. As for the induced drag, the value is about 90 counts. For the DLR-F6, the aspect ratio is 9.44 yielding an Oswald factor of 0.95 which is below unity, as expected. The wave drag is also higher, 5.4 compared to 1.5 counts, on the WBPN. Pressure contours on the WB and WBPN are presented in Fig. 6.7. It shows that the shock is stronger on the WBPN case yielding a higher wave drag. The experimental value for the scrubbing drag is 5.8 drag counts [58]. The computed value on the fine mesh is 6.3 counts yielding a relative error of less than 9% or less than 0.2% when compared to the aircraft total drag. Note that the experimental errors are not available to us.

The installation drag is listed in columns 16a-b-c and is computed with the near-field (16a) and far-field (16b) methods. As for the last column (16c), the installation drag is the sum of all variations in drag components. The three methods should yield the same value, however, small discrepancies are expected because the near-field/far-field drag balance is not exact as it is usually the case with this method. Nevertheless, the maximum discrepancy is 0.6 drag counts which is satisfactory.

Table 6.8 Drag decomposition on the Wing-Body and Wing-Body-Pylon-Nacelle (values in drag counts)

Property		**Drag**					**Net force**		**Install drag ($C_d^{install}$)**		
		C_d^v	C_d^w	C_d^{sp}	C_d^i	C_d^{scrub}	C_F^{NF}	C_F^{FF}	**NF**	**FF**	$\sum$
Equation		(6.17)	(6.18)	(6.23)	(6.21)	(6.26)	(6.6)	(6.7)	(6.37)	(6.37)	(6.16)-(6.23)
Column #		2	3	4	5	8	12	13	16a	16b	16c
	WB	203.5	2.4	4.8	87.9	-	299.3	298.9			
Coarse	**WBPN**	250.0	5.1	11.2	88.7	6.4	355.6	355.3	**49.9**	**50.0**	**50.1**
	Δ	46.6	2.7	6.4	0.8	6.4	56.3	56.4			
	WB	202.5	1.7	5.4	88.4	-	298.2	298.1			
Medium	**WBPN**	250.9	6.4	7.1	87.8	6.4	353.1	352.4	**48.5**	**47.9**	**47.9**
	Δ	48.4	4.7	1.7	-0.6	6.4	54.8	54.3			
	WB	203.0	1.5	1.2	88.8	-	294.9	294.6			
Fine	**WBPN**	244.9	5.4	5.2	90.6	6.3	346.2	346.1	**44.9**	**45.2**	**45.3**
	Δ	41.9	3.8	4.1	1.8	6.3	51.3	51.5			

Installation drag decomposition in power-on without thrust

The objective of this test case is to decompose the installation drag when no thrust in generated by the engines. To do so, the nacelle's boundary conditions are set to match the flow generated by a TFN, as explained in Section 6.4.2. The presence of the S_{in} and S_{out} planes allow computation of the pre-entry and the standard net thrusts through the fully far-field approach developed in Ref. [48].

In this section, three configurations are studied: the isolated CFM56 TPS nacelle, the Wing-Body and the Wing-Body-Pylon-Nacelle TPS. Installation drag can be computed by subtracting results of the WB from results on the WBPN TPS. Results are listed in Table 6.9. For each mesh, the last two rows represent the interference drag δ and the installation drag Δ, respectively as detailed in Section 6.3.5.

First, we notice that the viscous component has the main effect on the installation and inter-

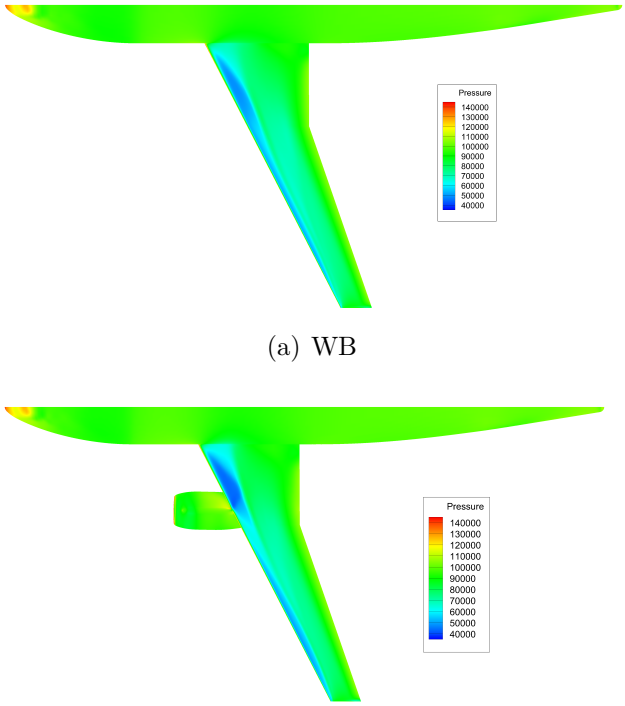

(a) WB

(b) WBPN

Figure 6.7 Pressure contours

Table 6.9 Installation and interference drag decomposition (without thrust)

Property		**Drag**						**Thrust**	**Net force**		**Conf. drag**	
		$\mathbf{C_d^v}$	$\mathbf{C_d^w}$	$\mathbf{C_d^{sp}}$	$\mathbf{C_d^i}$	$\mathbf{C_d^{tf*}}$	$\mathbf{C_d^{scrub}}$	$\mathbf{C_T^{Pre}}$	$\mathbf{C_F^{NF}}$	$\mathbf{C_F^{FF}}$	$\mathbf{C_d^{c\ (1)}}$	$\mathbf{C_d^{c\ (2)}}$
Equation		(6.17)	(6.18)	(6.21)	(6.23)	(6.36)	(6.26)	(6.27)	(6.6)	(6.7)	(6.32)	(6.33)
Column #		2	3	4	5	7	8	9	12	13	14	15
Coarse	**TPS**	22.6	0.0	14.6	0.4	-9.8	5.4	28.9	38.5	37.3	70.9	70.9
	WB	203.5	2.4	4.8	87.9	0.0	0.0	0.0	299.3	298.9	299.3	298.5
	WBPN	248.1	5.1	12.1	89.8	-10.0	5.7	21.7	356.3	354.7	381.0	381.0
	δ	22.0	2.7	-7.3	1.4	-0.2	0.3	-7.2	18.5	18.5	**10.8**	**11.6**
	Δ	44.6	2.7	7.3	1.9	-10.0	5.7	21.7	57.0	55.9	**81.7**	**82.5**
Medium	**TPS**	23.7	0.0	6.6	0.4	-8.6	4.1	28.9	31.4	31.1	64.1	64.1
	WB	202.5	1.7	5.4	88.4	0.0	0.0	0.0	298.2	298.1	298.2	297.9
	WBPN	245.6	6.4	8.6	91.3	-9.5	5.5	22.3	352.2	351.3	378.2	378.2
	δ	19.5	4.7	-3.4	2.4	-0.9	1.4	-6.6	22.6	22.1	**15.8**	**16.1**
	Δ	43.1	4.7	3.2	2.9	-9.5	5.5	22.3	54.0	53.2	**80.0**	**80.2**
Fine	**TPS**	23.6	0.0	4.6	0.4	-8.3	4.1	28.6	28.8	28.8	61.4	61.4
	WB	203.0	1.5	1.2	88.8	0.0	0.0	0.0	294.9	294.6	294.9	294.4
	WBPN	243.5	5.1	6.7	91.0	-6.9	5.8	21.8	343.5	345.3	369.2	369.2
	δ	16.9	3.5	0.9	1.9	1.3	1.7	-6.8	19.8	21.9	**12.9**	**13.4**
	Δ	40.5	3.5	5.5	2.3	-6.9	5.8	21.8	48.6	50.7	**74.3**	**74.8**

ference drags. On the finer mesh, they are 40.5 and 16.9 drag counts respectively, representing almost 11% and 5% of the WBPN configuration drag. This is expected since the viscous drag

on the nacelle is 23.6 drag counts, representing almost 40% of the nacelle configuration drag.

The installation drag is higher than the previous test case, 74.3 versus 44.9 drag counts on the fine mesh. This is explained by the fact that the configuration drag, which includes the pre-entry thrust and the additive through-flow drag, is used instead of the net propulsive force. The configuration drag is chosen to avoid the inclusion of the thrust in the computation of the installation drag.
There is a variation in the additive through-flow and scrubbing drags, as well as in the pre-entry thrust between the isolated and attached nacelle. Those three forces are related in the sense that they vary with the mass flow ratio which increases when the nacelle is attached. This means that the mass flow rate through the nacelle is higher when the nacelle is under the wing. Indeed, on the finer mesh, the isolated and attached mass flow ratios are 0.751 and 0.773 respectively. This explains the lower pre-entry thrust and the higher scrubbing drag. This difference is explained by the change in back pressure due to the presence of the wing. The latter affects the flow downwind of the nacelle causing an increase in the mass flow rate.

Total interference and installation drag are listed in columns 14 and 15 of Table 6.9. For each row, values in columns 14 and 15 are expected to be equal. The discrepancies are explained by the fact that values under column 14 are undecomposed while column 15 represents the sum of the interference/installation drag for each component i.e. viscous. The fact that the highest discrepancy is lower than one drag count is an implicit validation of those results. Basically, we notice that the installation and interference drags represent 20% and less than 4% of the total configuration drag which is not negligible. It is thus of utmost importance to carefully optimize the nacelle's position.

Installation drag decomposition with thrust

For this test case, the boundary conditions are changed to generate thrust. The total temperature and total pressure ratios, $T^0_{\text{outlet}}/T^0_\infty$ and $P^0_{\text{outlet}}/P^0_\infty$ at the nacelle's outlet are 2.053 and 1.17, respectively. Note that the thrust contribution to the lift has been neglected due to the small angle between the nacelle and the fuselage centerlines. Indeed, the angle of attack is kept constant when adding thrust and the variation in the lift coefficient is less than 0.001, resulting in a variation of less than 0.3 counts for a typical aspect ratio (i.e. 10) and span efficiency factor (i.e. 0.9) at a lift coefficient of 0.5. Results are presented in Table 6.10 for the medium mesh.

Table 6.10 Installation and interference drag decomposition (with thrust)

Property		**Drag**						**Thrust**	**Net force**		**Conf. drag**	
		$\mathbf{C_d^v}$	$\mathbf{C_d^w}$	$\mathbf{C_d^{sp}}$	$\mathbf{C_d^i}$	$\mathbf{C_d^{tf*}}$	$\mathbf{C_d^{scrub}}$	$\mathbf{C_T^{Pre}}$	$\mathbf{C_F^{NF}}$	$\mathbf{C_F^{FF}}$	$\mathbf{C_d^{c\ (1)}}$	$\mathbf{C_d^{c\ (2)}}$
Equation		(6.17)	(6.18)	(6.21)	(6.23)	(6.36)	(6.26)	(6.27)	(6.6)	(6.7)	(6.32)	(6.33)
Column #		2	3	4	5	7	8	9	12	13	14	15
Medium	**TPS**	14.9	0.0	16.2	0.3	-8.3	4.9	47.5	-278.0	-277.0	82.2	82.2
	WB	202.5	1.7	5.4	88.4	0.0	0.0	0.0	298.2	298.1	298.2	297.9
	WBPN	242.4	6.6	8.9	91.1	-11.7	4.4	43.1	39.0	35.4	399.3	399.3
	δ	25.0	4.9	-12.7	2.4	-3.4	-0.5	-4.4	18.8	14.3	**18.9**	**19.1**
	$\mathbf{\Delta}$	39.9	4.9	3.5	2.7	-11.7	4.4	43.1	-259.2	-262.7	**101.1**	**101.4**

First of all, the nacelle viscous drag dropped from 23.7 to 14.9 drag counts with the addition of thrust. However, when splitted in external, upwind and wake regions as presented in Table 6.11, we notice that the external drag is constant at 20.6 drag counts. It is the wake region that shifts from -0.3 to -8.9 drag counts. The spurious drag also increases from 6.6 to 16.2. Once again, it is in the wake region that most of the change happens. The spurious drag in the wake region increases from 3.6 to 12.5 drag counts. In the wake region of the isolated TPS, the viscous plus spurious drag variation from power-off to power-on is 0.3 drag count. This means that the entropy drag is almost invariable with the thrust increase. For the WBPN case, the viscous drag decreases from 245.6 to 242.4 drag counts yielding a variation of 3.2 counts while it decreases by 8.8 counts for the isolated TPS. Since the same boundary conditions are applied to both the isolated TPS and the WBPN, the same variation in the viscous drag would be expected. However, this is not the case. The reason that explains this phenomenon is the effect of the mesh. Comparing both meshes represented in Figs. 6.2 and 6.3, we notice that the mesh near the interaction region between inner and outer flows at the nacelle exit is more refined on the WBPN than on the isolated TPS. Since the mesh is unable to accurately solve the interaction between the inner and outer flows it causes the viscous sensor to falsely attribute a cell to the viscous zone [48]. This explains why there is a higher variation in viscous drag on the isolated nacelle compared to the WBPN.

The viscous installation drag decreases by 3.2 drag counts (43.1-39.9) which is due to the viscous drag variation on the WBPN when adding thrust. However, the viscous interference drag increases from 19.5 to 25.0 drag counts. This represents a variation of 5.5 counts, which is the consequence of the viscous drag decrease of 8.7 drag counts on the TPS case minus the variation in viscous drag on the WBPN case of 3.2 counts which yields the increase of 5.5 counts.

The same variation is present for the spurious interference drag. It is -3.4 counts without

thrust and -12.7 counts with thrust. This is a decrease of 9.3 counts which balances the increase in viscous interference drag of 8.7 counts. It is due to the spurious drag increase on the isolated TPS of 9.6 counts minus the spurious drag increase on the WBPN of 0.3 count. The spurious drag increases with thrust because the flow downwind the nacelle exhaust is faster (161 vs 263 m/s) thus more difficult to solve.

When adding thrust, the pre-entry thrust increases by 18.6 and 20.8 drag counts on the isolated TPS and WBPN cases respectively. This is expected since the MFR decreases from 0.750 to 0.678 on the CFM56 isolated nacelle. Recall that the smaller the MFR, the higher the pre-entry thrust. Using ESDU correlations [62], these MFR correspond to pre-entry thrusts of 26.8 and 43.4 drag counts, respectively while they are 28.9 and 47.5 using Eq. (6.27). The results presented in Tables 6.9 and 6.10 are thus in good agreement with empirical correlations.

The installation drag increases by 21.2 counts leading to the conclusion that the pre-entry thrust has the main effect on the installation drag variation when adding thrust. The sum of other phenomena contributes only by 0.4 count. The interference drag increases by 3.1 drag counts from 15.8 to 18.9 counts. The highest contribution is due to the pre-entry thrust. Other phenomena accounting only for 0.9 count.

The installation and interference drags represent 25% and 5% of the WBPN configuration drag, respectively. This increase, compared to the TFN case, is mainly due to the pre-entry thrust increase. Nevertheless, it is a non-negligible contribution to the configuration drag.

Table 6.11 Viscous and spurious drag distribution on the TPS (on/off) case on the medium mesh (values in drag counts)

Location	**Total**			**External**			**Upwind**			**Wake**			**Internal**		
Case	**TFN**	**TPS**	**Δ**	**TFN**	**TPS**	**Δ**	**TFN**	**TPS**	**Δ**	**TFN**	**TPS**	**Δ**	**TFN**	**TPS**	**Δ**
Viscous	23.7	14.9	-8.7	20.7	20.6	-0.1	0.0	0.0	0.0	-0.3	-8.9	-8.6	3.2	3.2	0.0
Spurious	6.6	16.2	9.6	2.5	1.6	-0.9	-0.3	0.4	0.7	3.6	12.5	8.9	0.8	1.7	0.8

6.5 Conclusion

The far-field theory applied to a motorized configuration as well as a review of the bookkeeping techniques for CFD were presented. A method was proposed to compute the installation and interference drags in power-on conditions based on the configuration drag instead of the traditional net propulsive force. The ability of the far-field method to ‘decompose the

configuration drag allowed to establish that the pre-entry thrust has the main effect on the installation and interference drags increase when adding thrust. We also notice that the viscous component is the main contributor to the installation drag, which was expected. It corresponds to 54% of the total installation drag in power off conditions.

Results validation was implicit by computing the configuration, installation and interference drags with two methods which were in good agreement. It was not possible to validate the present data otherwise because of the lack of CFD and experimental results in power-on conditions in the literature. However, we used the DLR-F6 geometry which is available to all so any other researcher can use them to validate our and their results.

CHAPITRE 7 DISCUSSION

Dans cette thèse, trois problématiques, dépendantes les unes des autres, sont traitées. En premier lieu, l'incapacité des méthodes traditionnelles à évaluer de manière précise la traînée interne est corrigée par l'utilisation de la méthode champ lointain limitée au volume interne de la nacelle. Par la suite, la force de captation, inhérente lors du calcul de la traînée de configuration en régime de poussée, ne requiert plus la connaissance précise du tube de courant capturé par le moteur. Une formulation entièrement basée sur la méthode champ lointain est proposée. Un des termes de cette formulation réutilise la méthode d'évaluation de la traînée interne. Finalement, il est maintenant possible de décomposer, en phénomènes physiques, les forces responsables des traînées d'installation et d'interférence. Le traitement de chacune des trois problématiques constitue les trois contributions de cette thèse. Le présent chapitre vise à éclairer le lecteur sur les différentes limitations des méthodes utilisées et développées dans ce travail. La stratégie de validation des traînées d'installation et d'interférence est également détaillée.

7.1 Limitations

Il est à noter que les méthodes développées dans cette thèse comportent certaines limitations. Premièrement, elles ne s'appliquent qu'à des simulations Navier-Stokes moyennées par le nombre de Reynolds (RANS). En second lieu, les algorithmes développés par l'auteur demeurent très couplés avec le logiciel commercial ANSYS Fluent. En théorie, la méthode peut être appliquée au post-traitement d'une simulation RANS peu importe le solveur utilisé. Cependant, la méthode champ lointain requiert que les propriétés telles que la pression et les vitesses soient accessibles au centre de chaque face de chaque cellule. Fluent utilise un schéma centré sur cellule. Il est donc nécessaire d'utiliser les gradients, également accessibles au centre des cellules, afin d'extrapoler les propriétés au centre des faces. Une telle opération doit obligatoirement être effectuée à l'intérieur du solveur, par le biais d'une fonction définie par l'usager *UDF-User Defined Function* ou par une sous-routine si le code source est disponible. Il est fort probable que toute tentative de reconstruction des flux au centre des faces à l'extérieur du solveur soit confrontée à un échec à moins d'être en contrôle du code source, ce qui n'est pas le cas avec Fluent. Finalement, toutes les simulations sont réalisées sur des maillages hexaédriques. Ces méthodes n'ont pas été testées sur des maillages de type tétraédriques dans le cadre de ce travail.

7.2 Traînées d'installation et d'interférence

L'évaluation et la décomposition des traînées d'installation et d'interférence constituent un important progrès dans ce domaine. Certes, la nécessité de trois simulations sur trois configurations distinctes, aile-fuselage, aile-fuselage-pylon-nacelle ainsi que nacelle isolée, pour chaque condition de vol peut paraître comme un désavantage. Cependant, de telles simulations sont beaucoup plus simples et moins onéreuses à implémenter que leur contrepartie expérimentale.

Il est à noter que peu de validation a été présentée dans le Chapitre 6. Puisque ce domaine reste peu étudié de la communauté scientifique, il est difficile de trouver des résultats expérimentaux et numériques sur une même configuration aux mêmes conditions de vol. De plus, lorsque des résultats sont disponibles, c'est la géométrie de la configuration qui ne l'est pas. Il a donc été décidé, depuis le tout début de ce doctorat, qu'une configuration publique serait étudiée. Le DLR-F6 équipé de nacelles CFM56 a donc été sélectionné. Des données expérimentales et numériques sont disponibles et publiées par le comité du second atelier de prédiction de traînée. Cependant, il a été impossible de valider nos résultats de décomposition des traînées d'installation et d'interférence en régime de poussée. À la connaissance de l'auteur, aucune autre étude n'a été publiée sur ce sujet. La validation a donc été effectuée par étapes, en augmentant progressivement le niveau de complexité. Tout d'abord, les résultats sur les configurations aile-fuselage ainsi que aile-fuselage-pylon-nacelle TFN ont été comparés aux résultats expérimentaux et aux résultats des autres participants du second atelier de prédiction de traînée [58]. Les valeurs étant en accord, la seconde étape a donc été de modifier légèrement les maillages des configurations nacelle isolée et aile-fuselage-pylon-nacelle afin d'implémenter les conditions limites servant à créer la poussée, mais en reproduisant un écoulement TFN. L'écoulement étant le même, les valeurs des traînées d'installation devaient être les mêmes. Une différence à été observée et expliquée par le développement d'une seconde couche limite à la sortie de la deuxième condition limite associée au plan de sortie de la turbine d'un moteur. La dernière étape a été de modifier les conditions limites de manière à générer une poussée. À ce point, les résultats obtenus n'ont pas pu être validés. Cependant, toutes les procédures employées ont été détaillées dans les trois articles et les configurations sont disponibles à tous de sorte que le lecteur intéressé puisse reproduire et valider les résultats.

CHAPITRE 8 CONCLUSION

Cette thèse porte sur l'utilisation de la méthode de champ lointain pour l'étude des configurations d'avions équipés de moteurs en régime de poussée. Traditionnellement, des essais en soufflerie sont préconisés afin de prédire la traînée d'installation motrice. Cependant, de tels essais comportent de nombreuses limitations et les erreurs expérimentales sont souvent importantes ce qui en diminue leur crédibilité. C'est pourquoi les avionneurs se tournent de plus en plus vers l'utilisation des méthodes numériques. La puissance de calcul qui augmente sans cesse et le continuel développement des méthodes numériques et des logiciels de CFD permettent ce virage. À ce jour, ce domaine reste peu exploré par la communauté scientifique. Une des raisons est sans doute que la simple intégration des forces de pression et de frottement sur la surface de l'avion ne permet pas d'analyse détaillée. La méthode de champ lointain est toute indiquée pour ce genre d'étude.

Le calcul de la traînée d'installation en régime de poussée requiert la connaissance de la traînée interne et de la force de captation. Une formulation entièrement basée sur la méthode de champ lointain a été proposée afin d'évaluer ces deux forces. Les résultats sont en accord avec les méthodes empiriques et les valeurs expérimentales, lorsque ces dernières sont disponibles. Finalement, l'objectif principal a été atteint et une méthode permettant l'analyse des configurations motorisées est maintenant disponible. Tel qu'expliqué précédemment, la validation reste en suspend, mais la procédure adoptée permet d'avoir confiance en les résultats obtenus.

Dans ce document, l'analyse d'une seule configuration, étudiée aux mêmes conditions de vols, a été présentée. Une avenue de recherche possible serait d'employer ces méthodes afin d'optimiser l'emplacement des nacelles sous les ailes. Il pourrait également être possible d'optimiser la manière dont les nacelles sont connectées aux ailes afin de minimiser la traînée d'interférence. Dans tous les cas, les outils développés et proposés dans cette thèse permettront aux aérodynamiciens d'étudier plus en profondeur les configurations de manière à pousser plus loin leur optimisation. Les moteurs simulés dans cette thèse sont à simple flux. Il serait intéressant d'appliquer les méthodes développées à des moteurs à double flux qui représentent mieux la réalité d'aujourd'hui. Finalement, l'utilisation de mailleurs automatiques et efficaces utilisants des cellules tétraédriques peuvent être très utiles lors de longs processus d'optimisation. La capacité de retirer la traînée numérique pourrait être mise à contribution afin de générer des résultats précis plus rapidement.

RÉFÉRENCES

[1] Ministry-Industry Drag Analysis Panel Study Group et al., "Guide to in-flight thrust measurement of turbojets and fan engines", Technical report, AGARD-AG-237, January, 1979.

[2] J. S. Holdhusen and J. L. Grunnet, "Model testing techniques for measuring inlet drag", *AGARD Aerodyn. of Power Plant Installation 8 p(SEE N 82-13065 04-01)*, 1981.

[3] Eugene E Covert, *Thrust and drag: Its prediction and verification*, volume 98, AIAA, 1985.

[4] J.M. Bousquet, "Survey of Engine Integration Testing in ONERA Wind Tunnels", in *41 st AIAA/ASME/SAE/ASEE Joint Propulsion Conference & Exhibit*, pp. 1–12, 2005.

[5] JW Slooff, "Computational drag analysis and minimization. Mission impossible?", 1986.

[6] A. Betz, "A method for the direct determination of profile drag (German)", vol. 1, pp. 258–260, 1938.

[7] EC Maskell, *Progress Towards a Method for the Measurement of the Components of the Drag of a Wing of Finite Span*, Procurement Executive, Min. of Defence, 1973.

[8] K. Kusunose, J.P. Crowder and RL Watzlavick, "Wave drag extraction from profile drag based on a wakeintegral method", in *37th AIAA Aerospace Sciences Meeting & Exhibit, Reno, Nevada, AIAA-99-0275*, 1999.

[9] RC Lock, "The prediction of the drag of aerofoils and wings at high subsonic speeds", *Aeronautical Journal*, vol. 90, pp. 207–226, 1986.

[10] J. Roskam, *Airplane Design*, Design Analysis & Research, 1985.

[11] D.P. Raymer et al., *Aircraft design: a conceptual approach*, volume 3, American Institute of Aeronautics and Astronautics, 1999.

[12] J. van der Vooren and J.W. Slooff, "CFD-based drag prediction: State-of-the-art, theory, prospects", Technical report, National Aerospace Lab., Amsterdam(Netherlands). Fluid Dynamics Div., 1992.

[13] D. Destarac, "Far-field drag in transonic potential flow- Analysis and optimisation", *Recent developments and applications in aeronautical CFD*, page 25, 1993.

[14] CP Van Dam, K. Nikfetrat, K. Wong and P. Vijgen, "Drag prediction at subsonic and transonic speeds using Euler methods", *Journal of aircraft*, vol. 32, n. 4, pp. 839–845, 1995.

[15] D. Lovely and R. Haimesy, "Shock detection from computational fluid dynamics results", *Shock*, vol. 1, pp. M2, 1999.

[16] R. Tognaccini, "Methods for Drag Decomposition, Thrust-Drag Bookkeeping from CFD Calculations", *VKI Lecture Series 2003, CFD-based Aircraft Drag Prediction and Reduction*, 2003.

[17] R.M. Cummings, MB Giles and GN Shrinivas, "Analysis of the elements of drag in three-dimensional viscous and inviscid flows", in *AIAA 14th Applied Aerodynamics Conference*, page 815, 1996.

[18] V. Schmitt and D. Destarac, "Recent progress in drag prediction and reduction for civil transport aircraft at ONERA", *AIAA paper 98*, vol. 137, 1998.

[19] Klaus Oswatitsch, *Gas Dynamics*, Academic Press Inc., 195.

[20] E. Laurendeau and J. Boudreau, "Drag prediction using the Euler/Navier-Stokes code FANSC", *SAE transactions*, vol. 112, n. 1, pp. 488–499, 2003.

[21] C. Veilleux, C. Masson and I. Paraschivoiu, "A new induced-drag prediction method using Oswatitsch's expression", *Aeronautical Journal*, vol. 103, n. 1024, pp. 299–307, 1999.

[22] C. Masson, C. Veilleux and I. Paraschivoiu, "Drag Predictions Using Euler Solutions of 2D and 3D Transonic Flows", in *37th AIAA Aerospace Sciences Meeting and Exhibit*, number AIAA-99-0527, 1999.

[23] D.L. Hunt, R.M. Cummings and M.B. Giles, "Wake integration for three-dimensional flowfield computations: Applications", *Journal of aircraft*, vol. 36, n. 2, pp. 366–373, 1999.

[24] DD Chao and CP Van Dam, "Airfoil drag prediction and decomposition", *Journal of aircraft*, vol. 36, n. 4, pp. 675–681, 1999.

[25] D. Destarac, "Far-field/near field drag balance and applications of drag extraction in CFD", *VKI Lecture Series*, pp. 3–7, 2003.

[26] L. Paparone and R. Tognaccini, "Computational fluid dynamics-based drag prediction and decomposition", *AIAA journal*, vol. 41, n. 9, pp. 1647–1657, 2003.

[27] S. Esquieu, "Numerical simulation and drag extraction using patched grid calculations", *Office National d'Étude et de Recherches Aérospatiales ONERA*, , n. 11, 2003.

[28] W. Yamazaki, K. Matsushima and K. Nakahashi, "Unstructured Mesh Drag Prediction Based on Drag Decomposition", in *European Conference on Computational Fluid Dynamics*, 2006.

[29] W. Yamazaki, K. Matsushima and K. Nakahashi, "Drag prediction and decomposition based on CFD computations", *JSME International Journal Series B*, vol. 48, n. 2, pp. 235–240, 2005.

[30] S. Esquieu, "Reliable Drag Extraction from Numerical Solutions: Elimination of Spurious Drag", in *Symposium, RTO-MP-AVT-147*, 2007.

[31] D. Hue and S. Esquieu, "Computational Drag Prediction of the DPW4 Configuration Using the Far-Field Approach", *Journal of aircraft*, vol. 48, n. 5, pp. 1658–1670, 2011.

[32] W. Yamazaki, K. Matsushima and K. Nakahashi, "Aerodynamic Design Optimization Using the Drag-decomposition Method", *AIAA journal*, vol. 46, n. 5, pp. 1096–1106, 2008.

[33] W. Yamazaki, K. Matsushima and K. Nakahashi, "Drag decomposition-based adaptive mesh refinement", *Journal of aircraft*, vol. 44, n. 6, pp. 1896–1905, 2007.

[34] M. Gariépy and J.-Y. Trépanier, "A new axial velocity defect formulation for a far-field drag decomposition method", *CASI Journal*, vol. 58, 2012.

[35] R. Abernethy, G. Adams, J. Ascough, J. Baer-Riedhart, G. Balkcom and T. Biesiadny, "In-flight thrust determination", *(SAE Aerospace Information Report, SAE AIR 1703, Nov. 1985) IN: In-flight thrust determination and uncertainty(A 88-15226 04-05). Warrendale, PA, Society of Automotive Engineers, Inc., 1986, 234*, 1986.

[36] JL Godard, H. Hoheisel, CC Rossow and V. Schmitt, "Investigation of interference effects for different engine position on a transport aircraft configuration", *Office National d'Études et de Recherches Aérospatiales Onera-Publications-TP*, 1996.

[37] O. Brodersen, "Drag prediction of engine-airframe interference effects using unstructured Navier-Stokes calculations", *Journal of aircraft*, vol. 39, n. 6, pp. 927–935, 2002.

[38] JL Godard, O. Brodersen and M. Hepperle, "Aerodynamic interference effects with engines of different by-pass ratio on the generic F 6 transport aircraft configuration", in *European Propulsion Forum, 7 th, Pau, France, Mar. 10-12, 1999, ONERA, TP*, number 1999-40, 1999.

[39] A. Hurez, "Recent Progress on Powerplant/Airframe Integration at Aerospatiale Matra Airbus", in *Contribution to the Workshop on EU-Research on Aerodynamic Engine/Aircraft Integration for Transport Aircraft, DLR Braunschweig*, pp. 26–27, 2000.

[40] W. Burgsmüller, C. Rollin and C. Rossow, "Engine integration on future transport aircraft", *The European Research Programs DUPRIN/ENIFAIR, ICAS Paper*, vol. 98, n. 5.6, pp. 1, 1998.

[41] E. Chaput, C. Gacherieu and L. Tourrette, "Application of Navier-Stokes Methods for Engine/Airframe Integration", in *Workshop on Airframe Engine Integration, DLR, Braunschweig, Germany*, pp. 6–7, 1996.

[42] J.P. Becle, J. Coste and J. Leynaert, "Nouveau banc d'etalonnage de nacelles equipees de turbines pour soufflantes (TPS), et essais d'ejecteurs", Technical report, AGARD-CP-348, 1983.

[43] S. Esquieu, *Evaluation de la traînée d'un avion de transport à partir de calculs numériques de mécanique des fluides*, PhD thesis, Université de Bordeaux, 2003.

[44] H. Ogoshi, Y. Yamaguchi and S. Suzuki, "Kawasaki Wake Survey System", *24th International Congress of the Aeronautical Sciences*, 2004.

[45] M. Meheut and D. Bailly, "Drag-breakdown methods from wake measurements", *AIAA journal*, vol. 46, n. 4, pp. 847–862, 2008.

[46] J. Van der Vooren and D. Destarac, "Drag/thrust analysis of jet-propelled transonic transport aircraft; Definition of physical drag components", *Aerospace science and technology*, vol. 8, n. 6, pp. 545–556, 2004.

[47] Benoit Malouin, Martin Gariépy, Jean-Yves Trépanier and Éric Laurendeau, "Internal drag evaluation for a Through Flow Nacelle using a far-field approach", *Journal of Aircraft*, 2014.

[48] Benoit Malouin, Martin Gariépy, Jean-Yves Trépanier and Éric Laurendeau, "Engine Pre-entry Thrust and Standard Net Thrust Evaluation Based on the Far-field Method", *Aerospace Science and Technology*, 2015.

[49] K Rüd and HJ Lichtfuss, "Trends in aero-engines development", in *Aspects of Engine-Airframe Integration, Proceedings of the DLR Workshop. 6-7 May*, pp. 1–23. Cranfield Institute of Technology, 1996.

[50] R. Tognaccini, "Drag computation and breakdown in power-on conditions", *Journal of aircraft*, vol. 42, n. 1, pp. 245–252, 2005.

[51] Martin Gariépy, Benoit Malouin, Jean-Yves Trépanier and Éric Laurendeau, "Far-Field Drag Decomposition Method Applied to the DPW-5 Test Cases Results", *Journal of Aircraft*, vol. 50, pp. 1822–1831, 2013.

[52] Martin Gariépy, Jean-Yves Trépanier and Christian Masson, "Convergence criterion for a far-field drag prediction and decomposition method", *AIAA journal*, vol. 49, n. 12, pp. 2814–2818, 2011.

[53] J. Seddon and E.L. Goldsmith, *Intake aerodynamics*, Blackwell science, 1999.

[54] "Drag of axisymmetric cowls at zero incidence for subsonic Mach numbers", *Engineering Sciences Data Unit (ESDU)*, vol. 81024, pp. 1–58, 2006.

[55] P.R. Spalart and S.R. Allmaras, "A one-equation turbulence model for aerodynamic flows", in *AIAA, Aerospace Sciences Meeting and Exhibit, 30 th, Reno, NV*, number AIAA-92-0439, 1992.

[56] Thomas H Pulliam, "Solution methods in computational fluid dynamics", *Notes for the von Kármán Institute For Fluid Dynamics Lecture Series*, 1986.

[57] E Laurendeau and J Boudreau, "Drag prediction methods using Bombardier Full-Aircraft Navier-Stokes code FANSC", in *2005 Aerospace Technology and Innovation Conference Toronto, Canada: CASI*, 2005.

[58] Kelly R Laflin, Steven M Klausmeyer, Tom Zickuhr, John C Vassberg, Richard A Wahls, Joseph H Morrison, Olaf P Brodersen, Mark E Rakowitz, Edward N Tinoco and Jean-Luc Godard, "Data summary from second AIAA computational fluid dynamics drag prediction workshop", *Journal of Aircraft*, vol. 42, n. 5, pp. 1165–1178, 2005.

[59] H. Schlichting and K. Gersten, *Boundary-layer theory*, Springer, 2004.

[60] Ishmail B Celik, Urmila Ghia, Patrick J Roache et al., "Procedure for estimation and reporting of uncertainty due to discretization in {CFD} applications", *Journal of fluids {Engineering-Transactions} of the {ASME}*, vol. 130, n. 7, 2008.

[61] CP Van Dam, *Critical Factors in CFD-Based Drag Prediction*, VKI Lecture Series, von Karman Institute for Fluid Dynamics, 2003.

[62] "Mass flow and momentum functions for one-dimensional flow of gas in ducts", *Engineering Sciences Data Unit (ESDU)*, vol. 81004, 1981.

[63] S.F. Hoerner, *Fluid-dynamic drag: practical information on aerodynamic drag and hydrodynamic resistance*, Hoerner Fluid Dynamics, 1965.